ROBOTIC INDUCTION OF NEUROMODULATION VIA PAIRED BRAIN STIMULATION WITH MECHANICAL STIMULATION

A Dissertation
Presented to
The Academic Faculty

By

Euisun Kim

In Partial Fulfillment
of the Requirements for the Degree
Doctor of Philosophy in the
George W.Woodruff School of Mechanical Engineering

Georgia Institute of Technology

May 2020

ROBOTIC INDUCTION OF NEUROMODULATION VIA PAIRED BRAIN STIMULATION WITH MECHANICAL STIMULATION

Approved by:

Dr. Jun Ueda, Advisor
George W. Woodruff School of Mechanical Engineering
Georgia Institute of Technology

Dr. Frank Hammond
George W. Woodruff School of Mechanical Engineering
Georgia Institute of Technology

Dr. YongTae (Tony) Kim
George W. Woodruff School of Mechanical Engineering
Georgia Institute of Technology

Dr. Minoru Shinohara
School of Biological Sciences
Georgia Institute of Technology

Dr. Dobromir Rahnev
School of Psychology
Georgia Institute of Technology

Date Approved: December 5, 2019

Soli Deo Gloria

ACKNOWLEDGEMENTS

I would like to first thank my advisor, Dr. Jun Ueda, for his dedicated guidance throughout my graduate career. His patience and generosity helped me go through my PhD study for the last five and a half years. His excellence in research and passion for learning new topics have inspired me to become a professional researcher. Also, his sincere care for his students encouraged me to dream to become a warm-hearted teacher. It is my great honor to have had him as my academic advisor and mentor.

I would like to express my sincere thanks to my reading committee, Dr. Minoru Shinohara, Dr. YongTae (Tony) Kim, Dr. Frank Hammond, and Dr. Dobromir Rahnev. I truly appreciate all helpful suggestions that they have given to me, with regard to both on my research, and on my career.

I would additionally like to thank my colleagues and friends at Georgia Tech for their encouragement and support. With you I have had great memory at Georgia Tech and thankful that I have made lifelong colleagues and friends like you. In particular, I would like to thank my friends in the Bio-robotics and Human Modeling Laboratory.

In addition, I would like to acknowledge my pastors and friends in New Church of Atlanta. I am grateful for their encouragement and prayers.

Last but not least, I would like to thank to my family for their sincere encouragement, support and prayers. Without their support, I would not have been able to accomplish my PhD study. Thank you for your unconditional love.

TABLE OF CONTENTS

LIST OF TABLES

LIST OF FIGURES

SUMMARY

Recent studies indicate that neural plasticity may contribute to functional recovery after a stroke where long-term potentiation (LTP) has been regarded as a contributor to motor learning as it strengthens excitatory synapses. There is an intervention that is known to induce LTP by applying transcranial magnetic stimulation (TMS) and peripheral stimulation. It is only when TMS and peripheral stimulation is repeatedly applied with an appropriate inter-stimulus interval (ISI) between them, that the LTP can be induced in the human motor cortex. Despite the promise of this intervention, tight time synchronization constraints and large variability in effective ISI among individuals still remain problems. In this study, the combination of TMS and mechanical stimulation as peripheral stimulation is used to understand the instantaneous neuromodulation of this intervention. This paired brain stimulation with mechanical stimulation was named mPBS. This mPBS intervention is similar to the intervention in paired associative stimulation (PAS), whereas PAS usually uses electrical stimulation as peripheral stimulation. The mechanical stimulation in mPBS was inspired by tendon tapping in a specific clinical practice called the repetitive facilitation exercise or RFE. The use of mechanical stimulation for peripheral stimulation in mPBS instead of electrical stimulation is expected to not only address tight timing issues associated with electrical stimulation, but also bridge the gap between the specific clinical practice RFE and conventional PAS. The objective of this research is to understand and characterize transient neuromodulation via mPBS. In order to accomplish the objectives the following aims were completed: 1) to verify timing repeatability of the mechanical stimulator for use in mPBS, 2) to apply statistical regression methods to estimate individual instantaneous neuromodulation ISI profiles faster than the conventional incremental method, and 3) to develop a robotic system that automatically tunes ISI and estimate enhanced motor evoked potential (MEP) profiles without human involvement to characterize the association between ISI and MEP in mPBS.

CHAPTER 1
INTRODUCTION AND BACKGROUND

1.1 Motivation

Currently, more than 700,000 people suffer a stroke each year in the United States and approximately two-thirds of these individuals survive and require rehabilitation treatment [1]. Among those stroke survivors, 60% of them experience significant impairments in movement [2]. Current post-stroke motor rehabilitation includes therapeutic interventions for regaining neural activation in hemiparetic limbs. However, therapeutic intervention in general is an intensive process that requires the patient's active and persistent effort to move the affected limb to gain motor recovery [3]. Current development of rehabilitation technology to improve physical therapy outcomes can be categorized into two approaches: (1) enhancing the frequency of exercise through video games that improves patient interaction and engagement [4, 5] and (2) facilitating neural excitation and neural plasticity to improve the effectiveness of therapy, shortening the period of treatment [6, 7, 8]. While studies have shown the potential of the first approach, there is still a need to characterize and quantify the second approach.

Recent studies indicate that neural plasticity may contribute to functional recovery after a stroke [9, 10, 11] and long-term potentiation (LTP) has been regarded as a contributor to motor learning because it strengthens excitatory synapses [12, 13]. Paired associative stimulation (PAS) is an intervention that repeatedly applies both transcranial magnetic stimulation (TMS) and peripheral stimulation with a timing interval between two. In general, electrical stimulation is used as the peripheral stimulation. It is known that only with an appropriate inter-stimulus interval (ISI) between the TMS and peripheral stimulation, LTP is induced in the human motor cortex [14, 15, 16]. To effectively induce LTP, PAS must

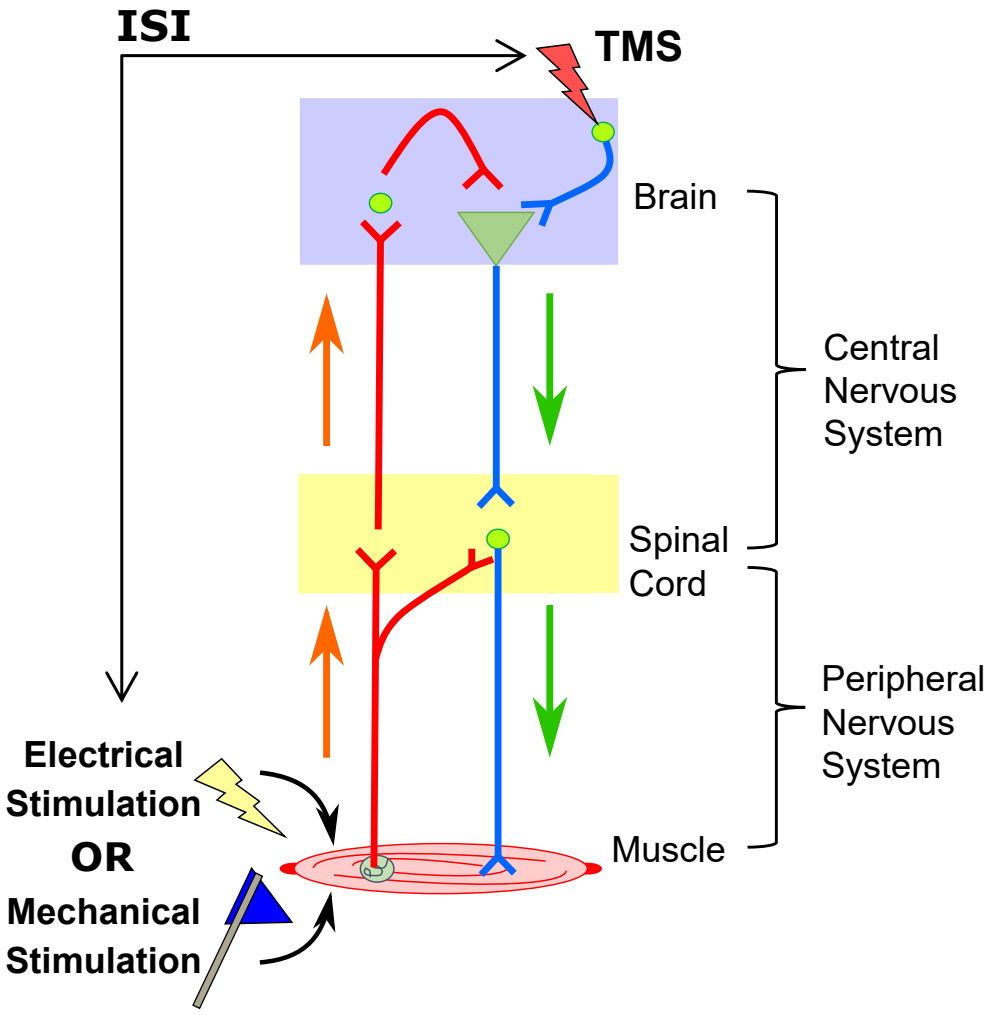

Figure 1.1: PAS and mPBS mechanism.

be repeatedly applied with an appropriate ISI as shown in Figure 1.1. There is a small range between the two stimuli to be effective, or the inter-stimulus interval window (ISI-W). Therefore, TMS and the peripheral stimulation must be tightly synchronized together so that the applied ISIs are within the effective ISI-W.

Despite promising features of PAS, the aforementioned tight time synchronization constraint in PAS and large variability in effective ISI among individuals still remain technical problems for implementation. In other words, individual differences in physiological parameters, such as body size and composition, gender and age [17, 18, 19, 20], impact the signal conduction time thus the effective ISIs that can induce LTP. This makes it very diffi-

cult to determine a single fixed ISI that can be applicable to any individual.

There are a number of studies that have been performed to identify the optimal ISI in the PAS intervention [21, 16, 22, 23, 24]. However, these studies tested a limited number of ISIs and determined the most effective ISI among them without considering the variability in individuals. In addition, other neural facilitation research attempted to find the effective ISIs but they required a very fine resolution of ISIs to observe responses which takes a lot of time [25, 26]. Therefore, a systematic approach that can meet time synchronization constraints and characterize individualized ISI profiles and helps understand the underlying mechanism of this paired stimulation with ISIs are required.

For this study, the combination of TMS and mechanical stimulation was used and the two stimuli were applied with different ISIs as shown in Figure 1.1. After the intervention, the instantaneous neuromodulation was investigated by measuring the MEPs right after each paired stimuli. This instantaneous neuromodulation paradigm using mechanical stimulation and TMS is defined as paired brain stimulation with mechanical stimulation, or mPBS in this study.This PBS with mechanical stimulation (i.e., mPBS) was inspired by a specific clinical practice called repetitive facilitation exercise or RFE [6, 27, 28]. In RFE, therapists manually apply mechanical tendon tapping to target muscles to induce the stretch reflex immediately before a patient is verbally instructed to produce a movement with the muscles as shown in Figure 1.2. Clinical studies report promising recovery results after RFE [29, 30]. PAS and RFE share a similar hypothesized mechanism, in which repetitive overlapping of responses of peripheral stimulation and cortical stimulation over the motor cortex will increase the neuron excitability level when the ISI is appropriate, allowing the patients to regain motor control. In addition, many studies on rats with mechanical stimulation in the form of whisker stimulation have shown neuroprotection [31, 32, 33]. This indicates the promising potential of mechanical stimulation for rehabilitation. In general, PAS pairs TMS and electrical stimulation and the goal of PAS study is to induce long term neuromodulation, not instantaneous neuromodulation. PAS has shown to induce

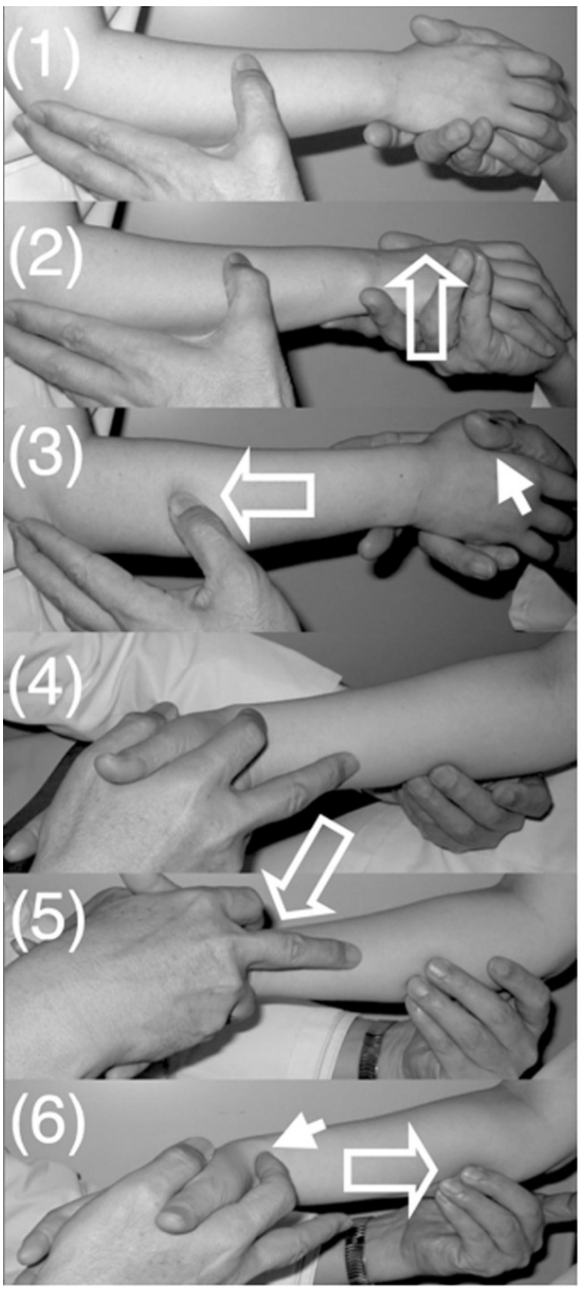

Figure 1.2: Repetitive facilitation exercise. The figure and caption are adopted from [6]. (1) To facilitate forearm supination/pronation with 90 elbow flexion in the sitting position, the therapist held the hand of the patient and placed the thumb of his other hand on the dorsal forearm, (2) quickly pronated the forearm, (3) rubbed the dorsal forearm with his thumb and provided slight resistance by his hand. (4) To facilitate forearm pronation, the therapist held the hand of the patient, (5) tapped with his second finger the radial wrist for quick supination of the forearm and (6) rubbed the ventral forearm using his third and fourth fingers. The open arrow and closed arrow indicate manipulation of the stretch reflex and light touch (resistance) to maintain the $\alpha - \gamma$ linkage, respectively.

Table 1.1: mPBS and PAS comparison.

	mPBS (paired pulse)	PAS (single pulse)
Stimuli	TMS & Mechanical Stimulation	TMS & Electrical Stimulation
Measurement	MEP	MEP
Measuring Time	After each paired stimuli (instantaneous neuromodulation)	Post intervention (long term neuromodulation)

long lasting plastic changes of neural excitability in the motor cortex [34]. Changes in the amplitudes of the motor evoked potentials (MEPs) are indication of PAS-induced neural excitability changes. The ISI between the peripheral stimulation and TMS may affect the magnitude of MEPs. In PAS, after applying two stimuli repeatedly with an appropriate ISI for a while, the amplitude of MEPs is measured for a long period after the PAS intervention (i.e., 10min, 20min,... after the PAS intervention) to observe the long-term neuromodulation effect. Both mPBS and PAS share similar intervention mechanism as shown in Figure 1.1, but mPBS investigates transient neuromodulation whereas PAS induces long-term potentiation. At this point, the correlation between transient neurodmoulation and the long-term potentiation is not clear. Table 1.1 shows the comparison between mPBS and PAS.

Using mechanical stimulation in mPBS instead of electrical stimulation is expected to bridge the gap between the specific clinical practice of RFE and conventional PAS. RFE is a clinically used exercise with little scientific research. On the other hand, PAS is a scientifically well-established method with little understanding of clinical effectiveness. Uniquely positioned between the conventional PAS and RFE, mPBS will help to understand the underlying mechanism of both interventions.

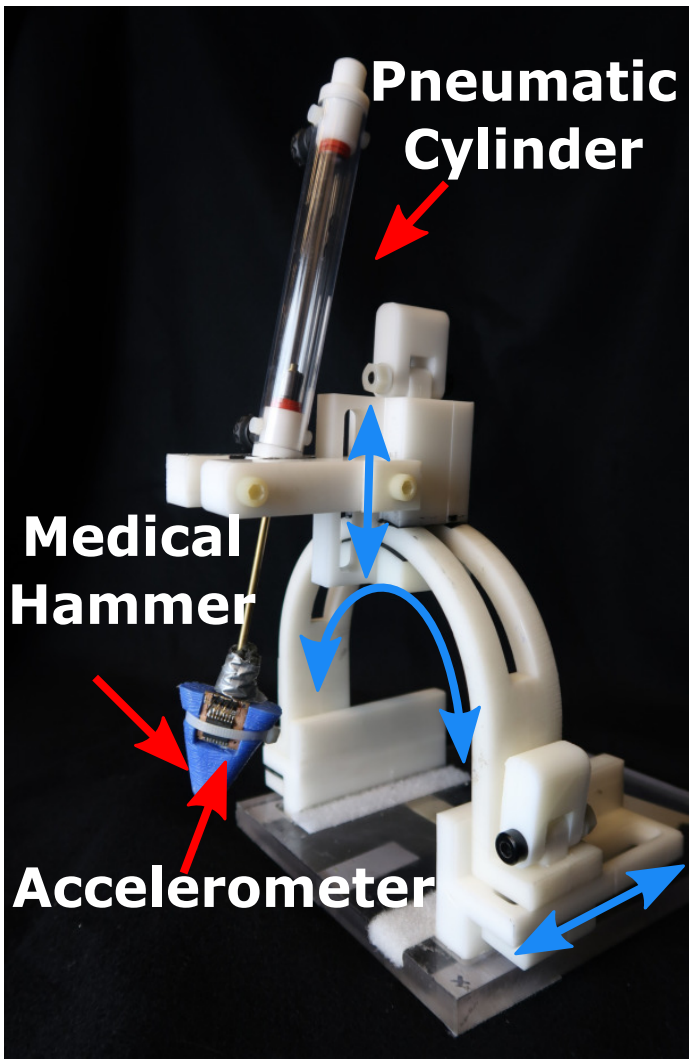

Figure 1.3: Mechanical stimulator overview.

1.2 Overview and Research Goals

1.2.1 Overview

Conventional PAS with electrical stimulation requires tight synchronization between TMS and electrical nerve stimulation. A small effective ISI range as shown in Figure 1.1, needs skilled operators and a long calibration time to characterize the ISI. In this thesis, the combination of TMS and mechanical stimulation was studied to address the aforementioned timing issues associated with the conventional PAS with electrical stimulation as explained in Chapter 1.1 to investigate the mechanical stimulation for a use for mPBS. Since the re-

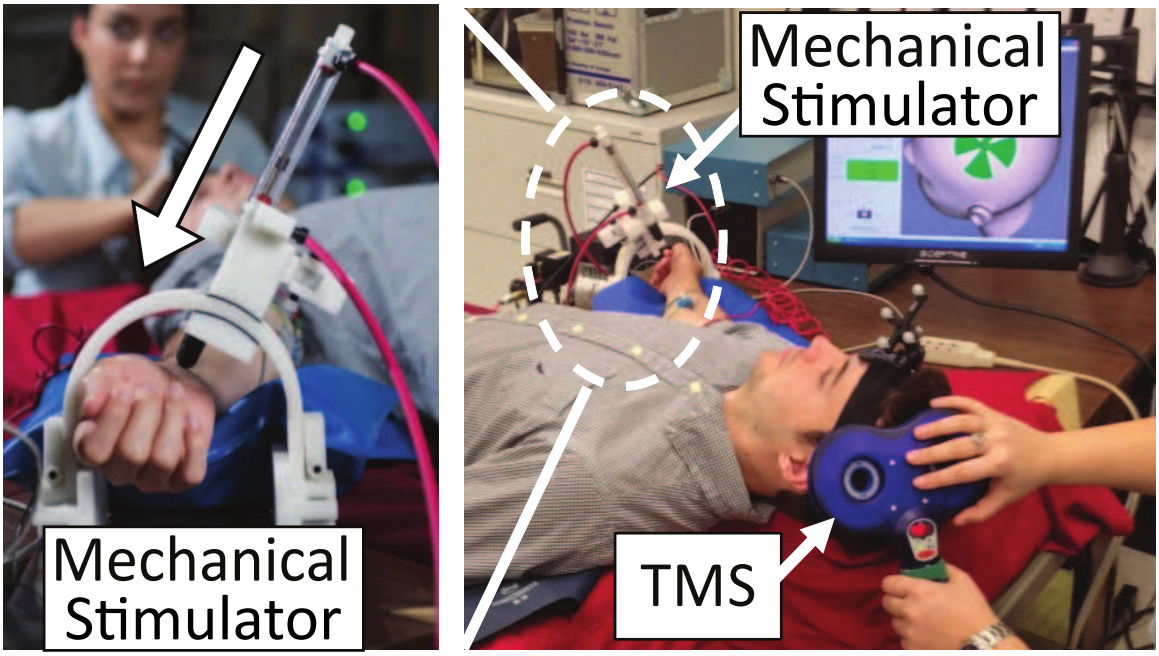

Figure 1.4: Experimental setup for mechanical stimulator and TMS.

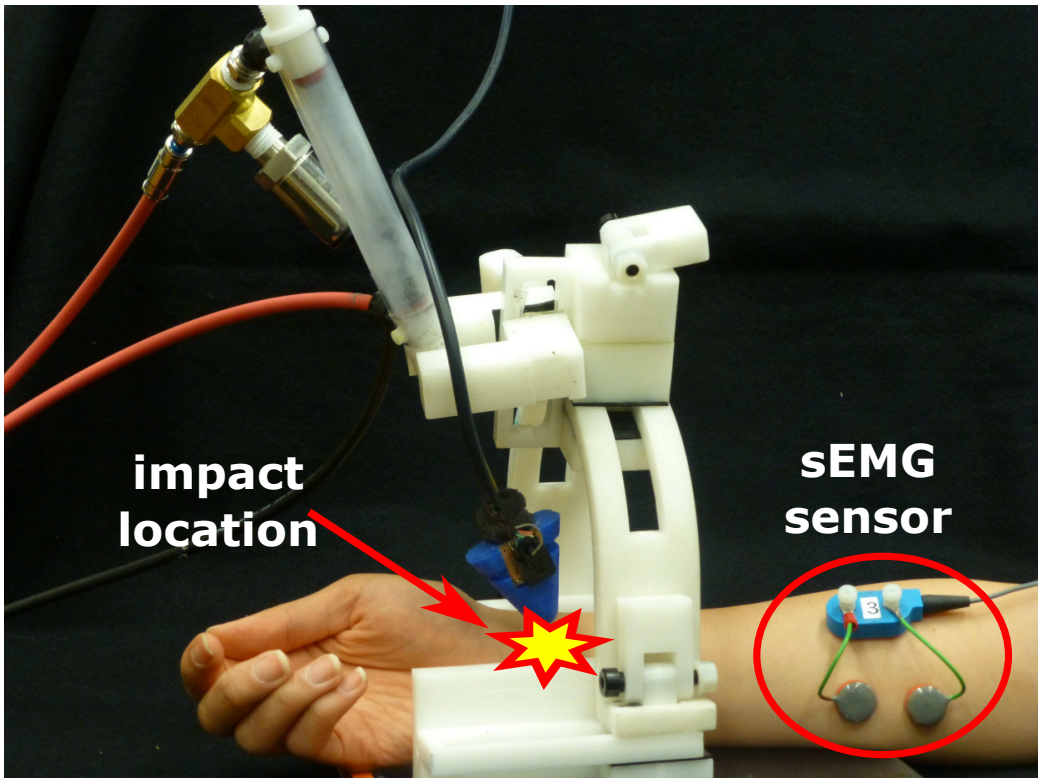

Figure 1.5: Experimental setup for mechanical stimulation.

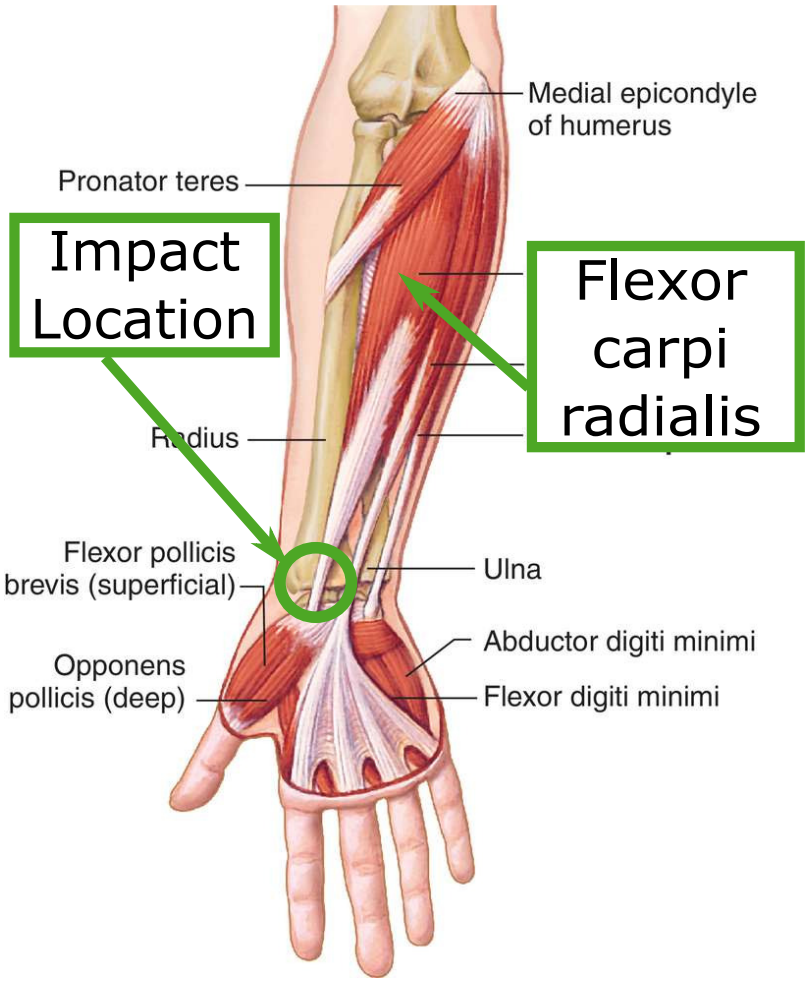

Figure 1.6: Anatomical structure of Flexor Carpi Radialis, or FCR muscle, adopted from [36]. The robotic tendon tapping device applies mechanical impact to the wrist tendon of the FCR muscle indicated by a circle.

peatability of human's manually-synchronized stimulation is not high [35], realizing manual mPBS, similar to RFE, to precisely apply two stimuli with a certain ISI was very challenging. This was because the ISI between those two were very small which is less than 100ms. Therefore a mechanical stimulator [37] that enables mPBS in the form of wrist tendon tapping has been developed as shown in Figure 1.3. As shown in Figure 1.4, this mechanical stimulator and TMS device applied mechanical stimulation and TMS to human subjects at various ISIs between the two stimuli. As shown in Figure 1.5 and Figure 1.6, this mechanical stimulator taps a subject's wrist tendon connected to the flexor carpi radialias (FCR) muscle. While performing the procedure, surface electromyography (sEMG)

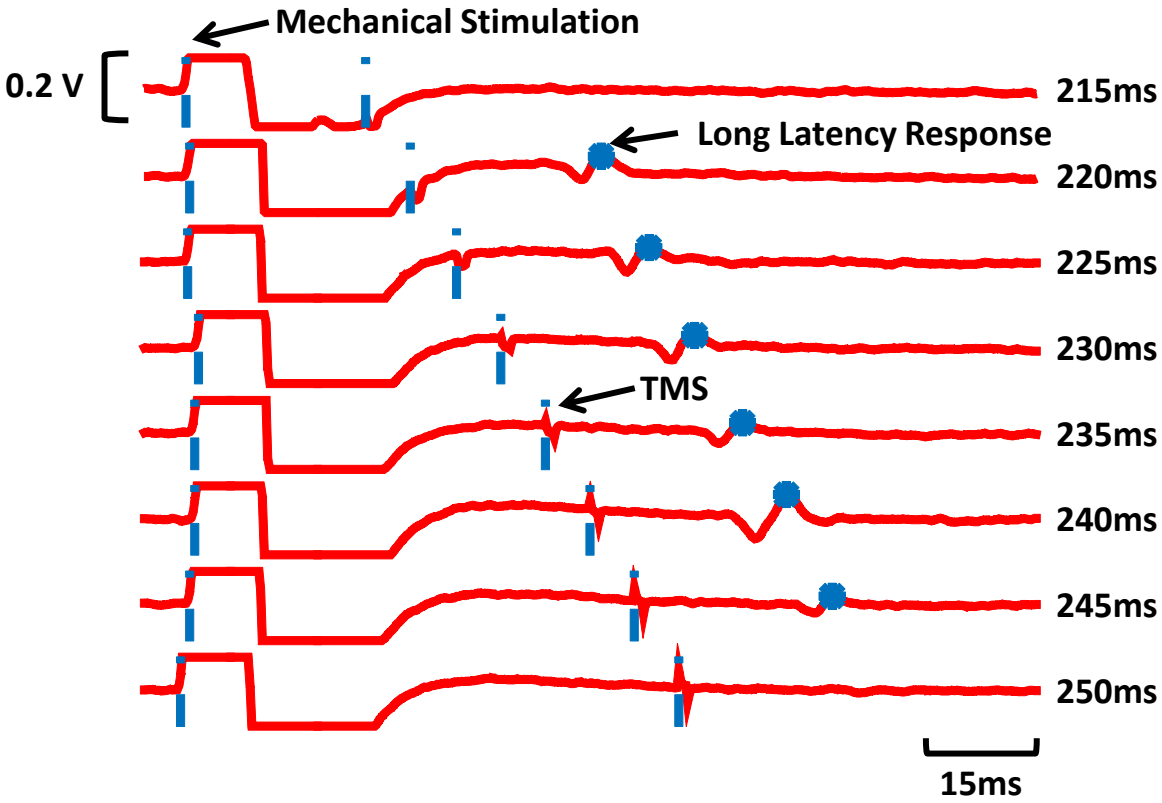

Figure 1.7: EMG Data of Long Latency Response with Different ISI of TMS and Mechanical Stimulation. The first dashed lines in blue indicate the timing of the EMG artifact due to mechanical stimulation and the second dashed lines in blue present the timing of TMS. The last blue points demonstrate the long latency response. The timing values on the right indicate the timing of TMS measured from the start of the experiment (t=0s) when the mechanical stimulation command is sent out.

is used to analyze the subjects' FCR muscle activity. The MEP amplitude from sEMG with different ISIs was analyzed to investigate the effectiveness of mPBS. Since the tight timing synchronization is required in mPBS, the repeatability of the mechanical stimulator system needs to be verified if it can meet the system requirements.

Once the mechanical stimulation from the mechanical stimulator and TMS are combined with an appropriate ISI, the long-latency response is expected to be observed in EMG as shown in Figure 1.7. From the region observing a long latency response, a peak-to-peak amplitude of MEP is used to characterize the instantaneous profile and range of ISIs that induce MEP. In the conventional method, MEP at various ISIs wre measured incrementally

to find an effective ISI-W profile. However, this is usually a time-consuming procedure which takes about 2 hours due to many stimuli which also gives physical burden on the subject. In order to solve this issue, the collected MEP vs ISI data were used to estimate an effective ISI-W using nonlinear regression, support vector regression, Gaussian process regression, and particle filtering. In addition, this mPBS procedure will be automated so that effective ISI is tuned automatically, removing a human operators' involvement in the tuning process.

1.2.2 Research Goals

This research aims to characterize and understand the instantaneous neuromodulation of mPBS by addressing the following research questions:

- **Question 1:** Is the mechanical stimulator timing precise enough to use it in mPBS that requires tight timing synchronization between the mechanical stimulator and TMS?
- **Question 2:** Is there a faster way to estimate the profile of ISI-W without using the conventional incremental method that is a time consuming procedure?
- **Question 3:** How can we build a fully automated system that can complete the ISI profile estimation without a human operator's involvement?

In order to answer these research questions, this research focuses on (1) the development of a mechanical stimulation platform that enables the mPBS intervention to induce neural facilitation in a more repeatable fashion; (2) characterization of effective ISI-W in mPBS for each individual more quickly and accurately; and (3) development of a closed-loop ISI-W determination system for mPBS. Therefore, this research aims to accomplish the following goals:

- **Aim 1:** To verify timing repeatability of the mechanical stimulator for use in mPBS.
- **Aim 2:** To apply statistical regression methods to estimate individual instantaneous neuromodulation ISI profiles faster than the conventional incremental method.

- **Aim 3:** To develop a system that tunes and characterizes ISI profiles automatically without human involvement to identify a dynamic human response model that explains the relationship between ISI and MEP in mPBS.

CHAPTER 2
LITERATURE SURVEY

2.1 Inter-stimulus Interval in Neurorehabilitation

Neural excitability of the motor cortex is essential for activating muscles, but is often compromised in hemiparetic stroke survivors. The modulation of this excitability can facilitate motor learning and recovery [38, 39, 40, 41, 42]. Excitability of the motor cortex is modulated by a repetition of electrical stimulation (Estim) to a peripheral nerve (e.g. median nerve) alone or its paired stimulation with central brain stimulation known as PAS [43, 44, 45, 46, 47]. Excitability of the primary motor cortex (M1) can be potentiated for a long term (approximately 1 hour) after a repetition of a conventional form of PAS, i.e., application of Estim to the peripheral nerve (e.g. median nerve) with an appropriate time interval immediately (approximately 25 ms) before TMS to M1 (termed Estim-PAS in this paper) in experimental studies [43, 44, 45, 46, 47].

In a therapeutic analogy such as RFE- an emerging effective rehabilitation for hemiparetic stroke survivors, a repetition of manual application of mechanical stimulation (Mstim) to the target muscles (e.g., tendon tapping or rapid muscle stretch) by a therapist immediately before a contraction effort of a patient (termed Mstim-paired manual therapy in this paper) can facilitate neuromotor recovery and often lead to significantly better rehabilitation outcomes compared with conventional rehabilitation without Mstim [48, 49, 6, 50, 28, 27].

One of the difficulties of stroke rehabilitation is that neurorehabilitation efficacy is variable [51, 52, 53]. Since a repeated application of PAS can result in facilitation or inhibition of neural excitability depending on the timing interval of stimulations, determination of the appropriate inter-stimulus interval (ISI) is crucial for inducing facilitation [54, 55]. ISI is

the period of time that separates two consecutive stimuli [56]. In the conventional form of PAS (i.e. Estim-PAS), ISI is the timing difference between Estim and TMS. Neural plasticity via Hebbian learning is assumed to be induced through the repetition of paired associative excitatory inputs to M1. One is originating from the stimulation of the somatosensory system (afferents) and the other is from either TMS or motor effort of an individual in response to therapist provided instruction [57] which arrives at M1 shortly after the afferent stimulation. The time interval between the two paired inputs is critical to the consequence of PAS and likely other therapeutic techniques [58, 57]. Since the scientific mechanisms for this promising emerging Mstim-paired manual therapy are not well understood, the time interval between the peripheral Mstim by a therapist and the central motor effort by a patient is undefined and thus can be variable. Individual differences in signal transduction times due to various anatomical and physiological characteristics such as body size and composition, sex, and age [59, 18, 20] may influence the timing-dependent profiles of neural excitability and thus the effectiveness of Mstim-paired manual therapy. Anecdotally, physical therapists skilled in this clinical practice are able to adjust the stimulation intervals by observing responses in patients based on their experience. However, this heuristic approach is unfortunately not fully generalizable. As a result, Mstim-paired rehabilitation has been difficult to standardize. Hence, it is imperative to develop an efficient method that helps determine the appropriate range of ISI for inducing neuromodulation in Mstim-paired manual therapy or Mstim-PAS for each individual. In addition, it is reported that this neuromodulation effectiveness is dependent on a particular phase of the sleep-wake/circadian cycle [60, 61].

2.2 Characterization of Mstim-induced neuromodulation

Potentiated synaptic excitability of M1 is assessed with the amplitude of motor evoked potentials (MEP) via unpaired single-pulse TMS. Induced potentiation at this motor system level is analogous to the long-term potentiation (LTP) at the synaptic level, i.e., strength-

ened excitatory synapses due to repetitive timing-dependent excitation of presynaptic and postsynaptic neurons (Hebbian model) [62, 63, 64]. At the synaptic level, LTP can be induced only when the postsynaptic neurons are excited immediately after the excitation of presynaptic neurons. Similarly, the largest and most consistent facilitation of M1 via neuromodulation is induced when cortical stimulation is applied 2-5 ms after the arrival of the Estim-induced sensory signal in the somatosensory cortex [45, 65, 66, 67]. With Estim, the arrival time can be determined for each individual with the first negative peak around 20-ms latency (N20) in somatosensory evoked potentials recorded through electroencephalography (EEG) [46, 67]. The critical issue is that Estim-PAS can induce inhibition if the brain is stimulated 5-10 ms before the arrival of the sensory signal [46, 66, 67]. For example, Wolters et al. previously utilized the N20-P25 somatosensory evoked potential (SSEP) complex to evaluate the effect of PAS timing on neural plasticity [58]. The latency of the complex is important to clinical applications of PAS, as changes of even 15ms in timing can reverse the direction of the neuromodulation. [58]. Hence, the consequent neuromodulation with this type of paired stimulation can be inverted due to a subtle timing error.

Depending on stimulation intensity, Estim often causes a painful sensation. In addition, PAS with electrical stimulation requires tight synchronization between TMS and electrical nerve stimulation, requiring skilled operators and a long calibration time. In contrast, Mstim is more applicable and relevant to actual clinical practice and the desired muscle activity. Moreover, Mstim allows access to various muscles that cannot be individually accessed via electrical nerve stimulation.

As a simpler paradigm before this combined long-term effect is investigated, however, there are few studies that have examined instantaneous and transient modulation of excitability of M1 due to Mstim. In the Estim, excitability of M1 is inhibited at a latency of 19-50 ms, known as short-latency afferent inhibition [22], and is likely due to the direct thalamocortical projections to M1 via cholinergic paramedian thalamic nuclei [68] and the projections from the primary sensory cortex to M1 [69, 70], which recruits M1 interneurons

that inhibit layer V pyramidal neurons [68, 71].

In contrast, Mstim of the periphery in the form of muscle stretch often produces a transcortical long-latency stretch reflex with 50-150ms latencies [72, 73], indicating the induction of long-latency facilitation of the M1. The impact-based Mstim to the muscle-tendon complex can stimulate various mechanoreceptors in the skin, tendon, muscle, and joint. These afferent inputs induced by Mstim can project to various supraspinal pathways other than those with Estim, potentially leading to not only net facilitation but also net inhibition of M1 in a latency-dependent manner.

While long-term neuromodulation can be induced after a repetition of Estim-PAS or Mstim-paired manual therapy with an appropriate timing interval, a single application of peripheral stimulation can also induce transient neuromodulation in a time-dependent manner. The time-dependent profiles of neuromodulation in response to an impact-based Mstim of muscles have been understudied because of the absence of a versatile and reliable mechanical stimulator that allows for timing adjustment. This configuration that pairs Mstim and TMS enables the investigation of neuromodulation via different afferent nerve stimulation from one studied by using the conventional conditioned stimulation with Estim and TMS [74, 22, 75, 76, 24, 77]. The form of mechanical tendon tapping will not induce joint motion unlike other studies that have utilized rapid joint extension as Mstim [78].

2.3 Interstimulus Interval (ISI) between Mstim and TMS timings

There are significant research interest on the interstimulus interval (ISI) between the peripheral stimulation and transcranial magnetic stimulation in paired associative stimulation. ISI is crucial in paired stimulation, since the effect of an intervention depends on the ISI; neural excitability can be inhibited or excited. Some studies reported how the ISI values affect the result of their intervention [23, 16, 22]. Other studies have reported the optimal ISI of paired associative stimulation for soleus muscle [21]. Since each individual has different body dimensions and neural conduction times, one ISI cannot be effective for everyone.

Due to the generally large variability in effective ISI in individuals [79], an adjustment procedure must be performed before actual neuroscientific research in every single subject. The method of evaluating ISI requires many data samples and times [80]. However, to the best of the author's knowledge, there is no study on determining effective ISIs efficiently for individuals.

2.4 Automated closed-loop neuromodulation system

Neuromodulation using PAS, mPBS, RFE, and so on, is known to potentially effective treatment for neurological diseases leading to the resumption of motor functionality. However, these treatments still have room for improvement by automating the current manual and long time-consuming process. A closed-loop approach may possibly lead to the adjustment of the parameters such as ISI for each individual by monitoring the subjects' MEP. In neuromodulation, there are a number of studies on closed-loop neurostimulation that provided therapeutic stimulation in response to changes in patients in different fields of studies such as deep brain stimulation [81], spinal cord injury [82], and so on. Based on the author's knowledge, there is limited study on automating the entire ISI adjustment procedure. In order to reduce the human operator's burden during therapeutic exercise and be able to adapt to each individual condition in a short period of time, an automated system should be effective.

CHAPTER 3
TIMING ANALYSIS OF MECHANICAL STIMULATOR

3.1 Problem Description

In the conventional paired brain stimulation (PBS), electrical stimulation, Estim in short, has been used as the most popular stimulation modality [16]. Estim is advantageous in that it can directly stimulate the median nerve so that the nerve stimulating time can be precisely given. However PBS with Estim requires a tight synchronization between TMS and Estim, requiring skilled operators and a long calibration time to find the very short ISI-W of PBS with Estim. In addition, PBS with Estim requires significant resources such as an Estim device and related tools which may only be available at major medical facilities or academic institutions. Depending on stimulation intensities, Estim often causes a painful sensation in users [83].

In order to address the issues of PBS with Estim, mPBS (i.e., PBS with mechanical stimulation) was designed and tested. This mechanical stimulation, Mstim in short, was inspired from the mechanical tendon tapping in the RFE intervention which has shown some advantages over Estim in its longer duration for exciting the nerve [84]. Mechanically induced muscle activation may be dispersed in a time range because of desynchronized activation of muscle spindles after mechanical tendon tapping.

3.2 Mechanical Stimulator

3.2.1 Mechanical Design of Mechanical Stimulator

As shown in Figure 1.3, the mechanical stimulator was designed to perform tendon tapping on the human wrist [7, 37]. This mechanical stimulator was designed to be adjustable for all subjects by rotating and translating the device so that the hammer can tap the human

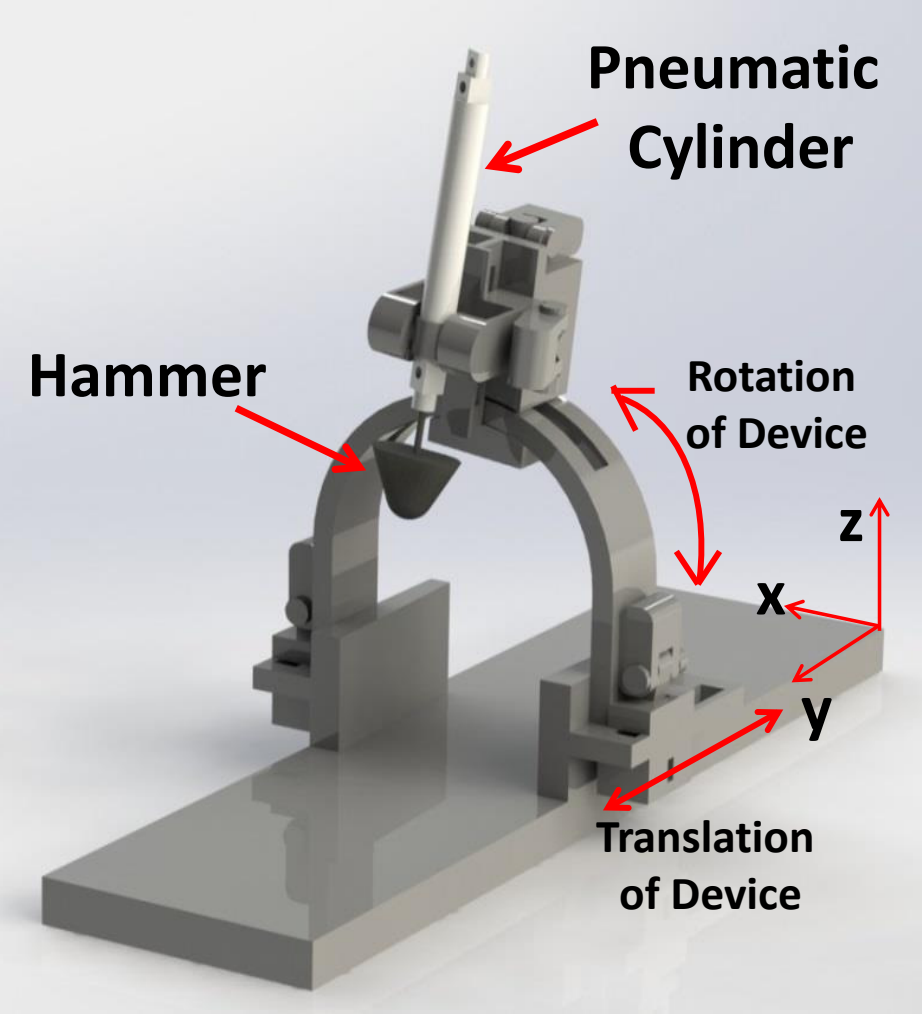

Figure 3.1: Robotic Neuromodulation Rehabilitation System (RNRS).

wrist tendon from an appropriate angle as shown in Figure 3.1. In order to use this device in a functional magnetic resonance imaging (fMRI) environment and observe how the brain activity changes with robotic intervention in future studies, only MRI safe materials were used [37]. This system was operated by a pneumatic linear cylinder (Airpel E9D20U, Airpot Corporation, Norwalk, CT, US) equipped with a medical hammer at the end to apply Mstim to the target muscle tendon in the form of tendon tapping. A pressure sensor (SSI-P51-101, SSI Technologies, Inc., Janesville, WI, US) was used to measure the pressure of the upper chamber of the cylinder, to which constant pressure was applied during the motion. An accelerometer (MMA2202K, Freescale Semiconductor, Inc., Austin, TX, US)

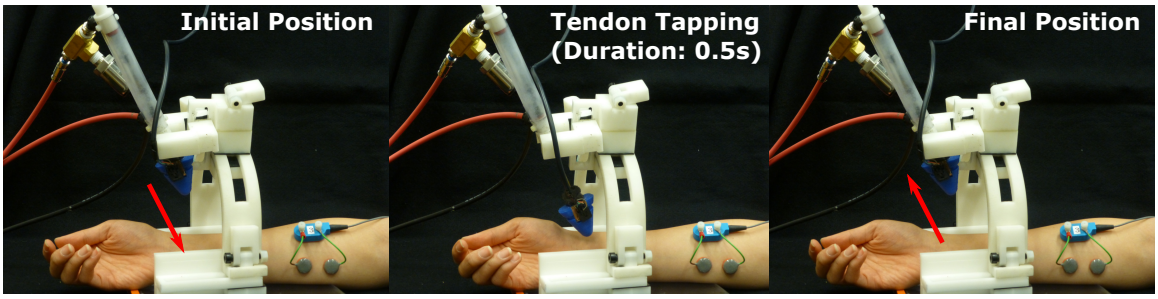

Figure 3.2: Tendon tapping motion.

attached to the hammer was used to detect the time when the medical hammer hit the tendon. This pneumatic system created the tapping motion as shown in Figure 3.2. It moved toward the wrist tendon, tapped the tendon approximately for 0.5 seconds and moved back to the original position.

3.2.2 Pneumatic System Setup

All of the non-fMRI compatible components were attached to an air compressor (GMC Syclone 6310, GMC) via 7.5-meter long pneumatic lines with a 0.25 inch outer diameter. This air compressor outputted air at 416.7kPa (60psi) and a four-way spool valve (MPYE-5-1/4-010-B, Festo, US) was used to operate the pneumatic cylinder by controlling this pressurized air flow. A 7.5-meter long line is used to secure the distance between the MRI chamber and the MRI control room, where non-fMRI compatible materials are allowed.

3.2.3 System Operation

Commands and sensor readings such as 1) mechanical stimulator output commands, 2) TMS output commands, 3) accelerometer readings, 4) pressure sensor readings, and 5) EMG signals were converged into a Power 1041 deck (Power1401-3A, Cambridge Electronic Design Limited, Cambridge, England) processed by commercial software Signal (Signal Version 5, Cambridge Electronic Design Limited, Cambridge, England).

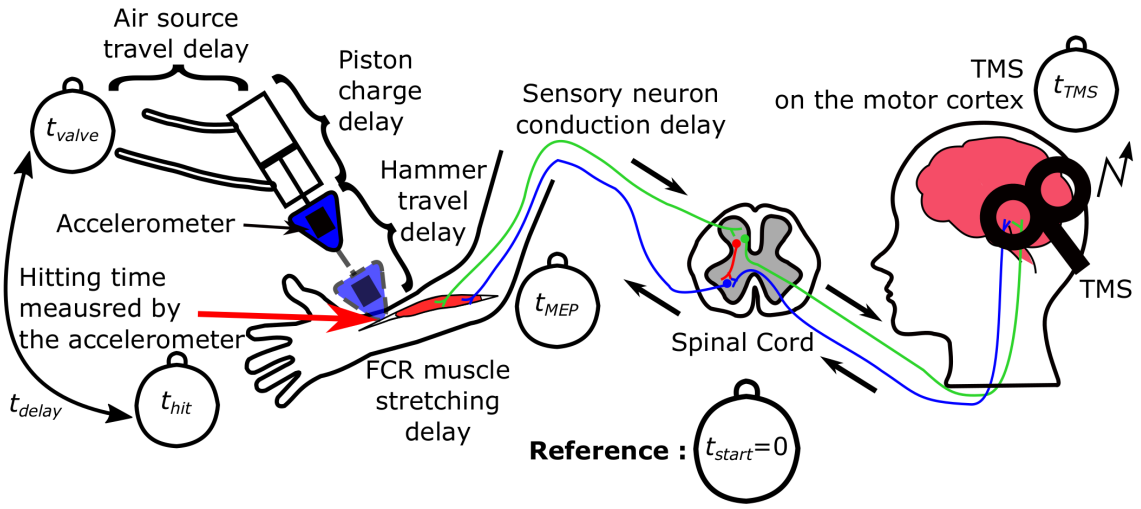

Figure 3.3: Sources of time delay in paired brain stimulation with mechanical stimulation.

3.3 Timing analysis of the Mechanical Stimulator

As mentioned in the previous section, mPBS is a time sensitive neural facilitation procedure that requires tight synchronization of the time interval between cortical stimulation and peripheral stimulation. Compared with Estim, there are additional sources of time delay and variability in the developed pneumatic mechanical stimulator, including: 1) air pressure propagation time in the pneumatic line, 2) pressure development time in the pneumatic chamber, 3) travel time of the hammer moving from its initial position to the target tendon position, and 4) nonlinear mechanical interaction between the hammer material and skin/subcutaneous tissues. The sum of these factors produces a system delay between a pneumatic valve open command and the resultant tendon tapping as illustrated in Figure 3.3. Therefore, in this chapter, the timing repeatability of the mechanical stimulator was tested.

3.3.1 Mechanical Stimulation Timing Detection

This experiment was conducted to collect data to analyze the Mstim timing of the tendon. In the first experiment, a force sensor (LCM703-50, Omega Engineering Inc., Stamford, CT) was placed underneath the mechanical stimulator to detect the actual Mstim timing as

shown in Figure 3.4. Also, the same experiment was performed with human subjects by placing their wrist underneath the stimulator as shown in Figure 3.5. One representative graph of the experiment with the force sensor is shown in Figure 3.6. Another representative graph for a human subject is shown in Figure 3.7. Descriptions of the important timings, in order of occurrence, are given in Table 3.1. The timings explained in Table 3.1 were determined using the following procedures:

1. t_{ini} : Initial valve signal was programmed to be sent after 0.5 second of the start of the system by *Signal* control software.

2. t_{fill} : Start time of supplying pressurized air to the top pneumatic chamber was defined as the first time when the pressure sensor data showed pressure increase. This delay was due to the long length of the pneumatic line of 7.5m.

3. t_{descent} : Time when the hammer started its downward descent was defined as the first time when the accelerometer went above a threshold value and never went back below it.

4. t_{hit} : The hammer hitting the object or the tendon was obtained by detecting when the accelerometer values changed from positive to negative, signifying a sharp decrease in velocity. This is the onset of mechanical stimulation.

5. t_{away} : The hammer bouncing away from the object or tendon was obtained by detecting when the accelerometer values changed from negative to positive, signifying that the tendon had finished pushing back the hammer.

6. t_{memg} : EMG onset is obtained by detecting the time when the EMG signal changes from the zero value.

Two timings, t_{hit} and t_{away} were confirmed using force sensor data. In Figure 3.6, the acceleration of the hammer hitting the object agreed with an initial spike in the force sensor data. The accelerometer reading when the hammer was till at the initial position was used

as a baseline level. t_{hit} was detected when the first falling edge of the reading crossed the baseline level as shown in Figure 3.6. The acceleration of the hammer bouncing away from the object agreed the end of the impulse shown in the force sensor data. The time delay between the two may be an Estimate for the duration of time that the hammer pressed on the object.

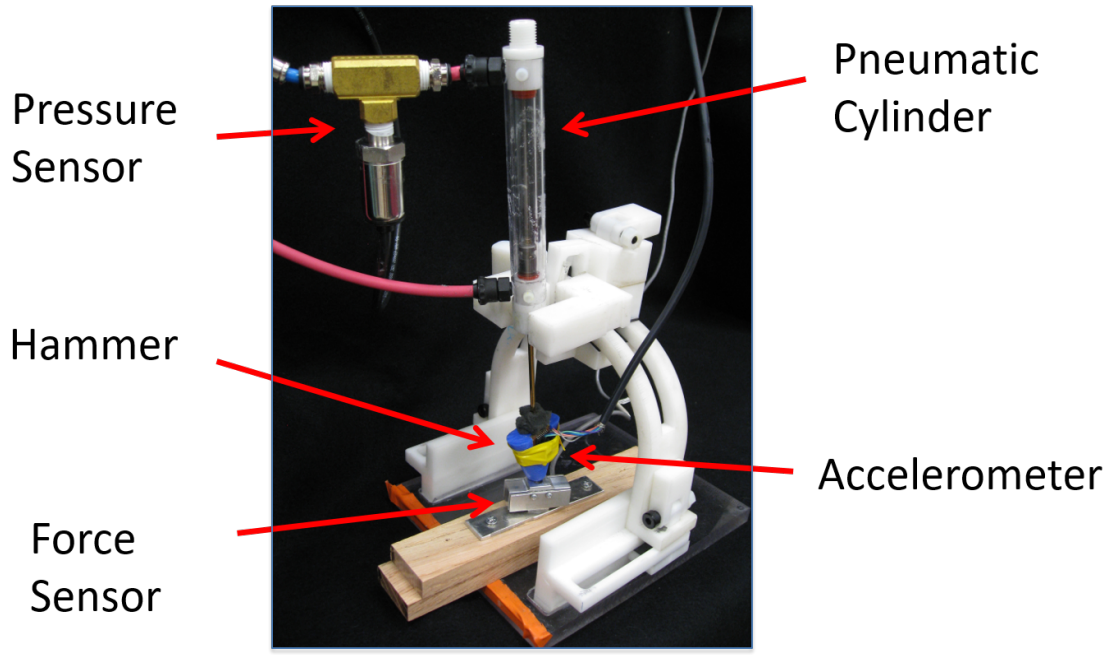

Figure 3.4: Experimental setups for testing of timing delays of mechanical stimulator with force sensor.

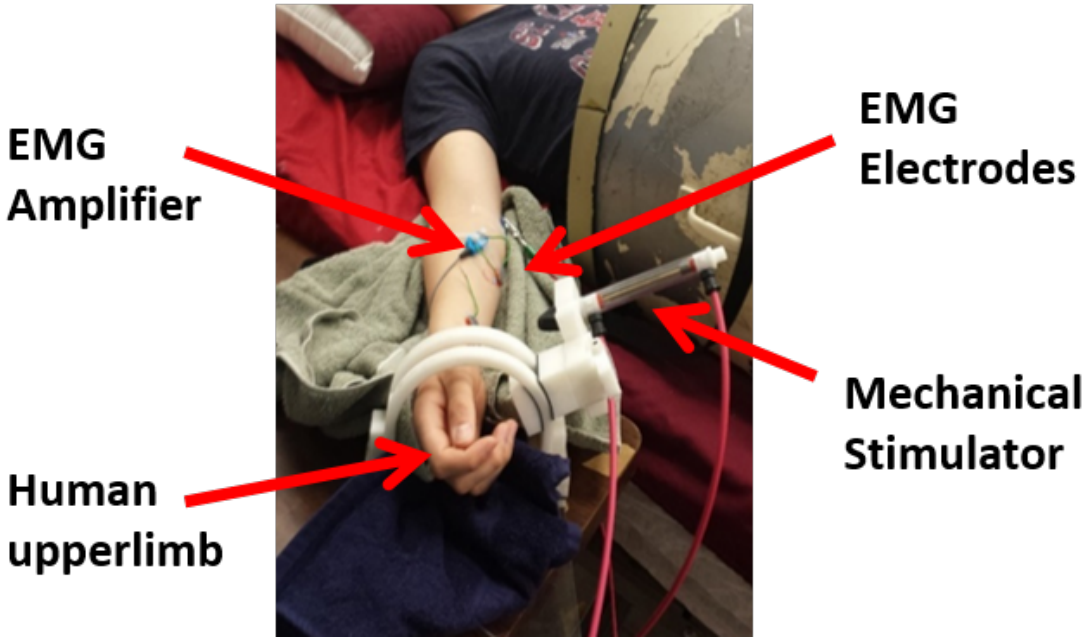

Figure 3.5: Experimental setups for testing of timing delays of mechanical stimulator with human subject.

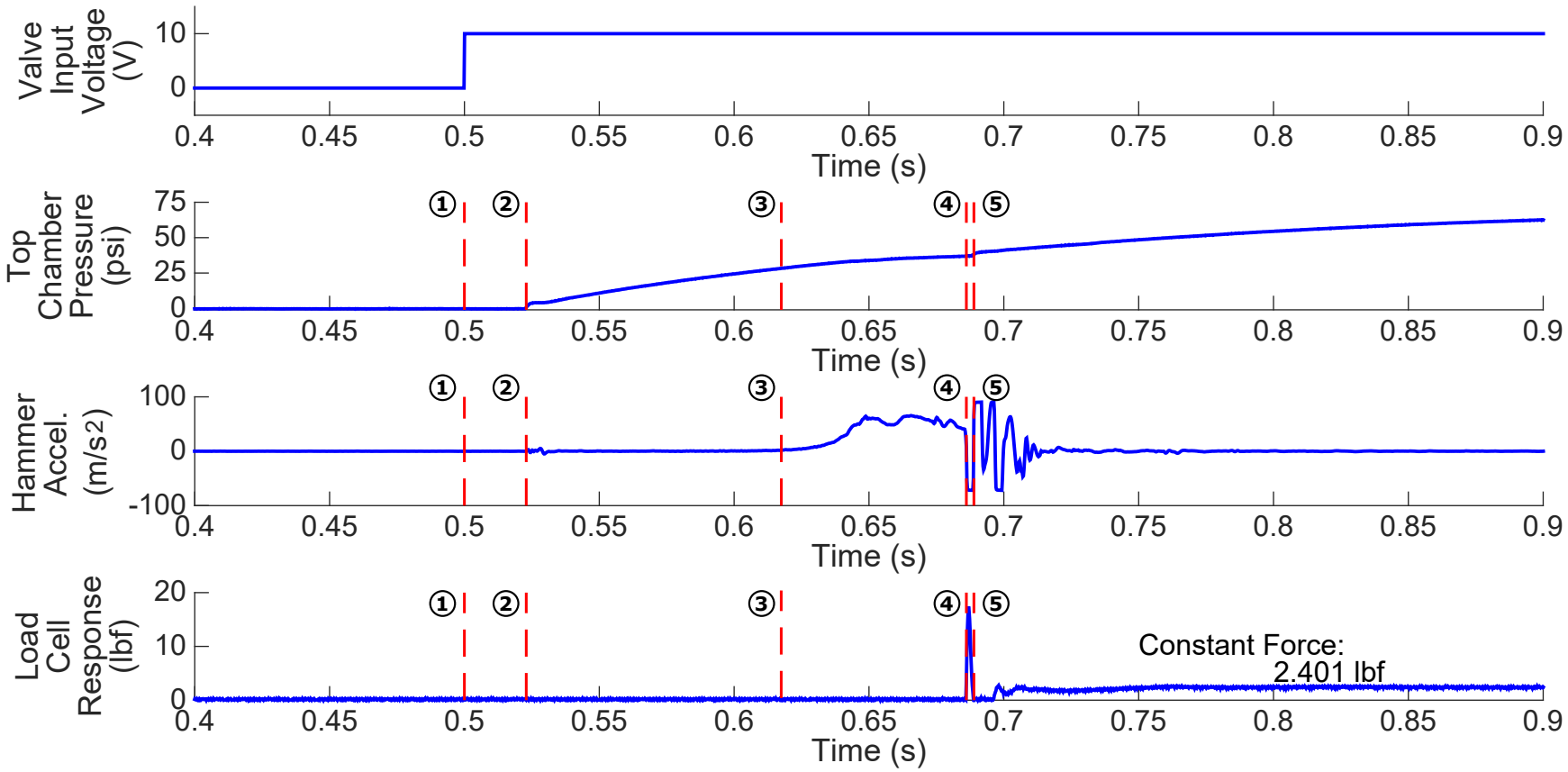

Figure 3.6: One trial with the force sensor. Timing delays sensor data. This force sensor graph was plotted from one out of 50 trials. The red dashed lines represent the following time points in order: 1) Valve starts to open (t_{i}), 2) Pneumatic cylinder starts to fill up (t_{fill}), 3) Hammer starts to move down (t_{descent}), 4) Hammer hits the object or tendon (t_{hit}), 5) Hammer rebounds away from the object or tendon (t_{away}).

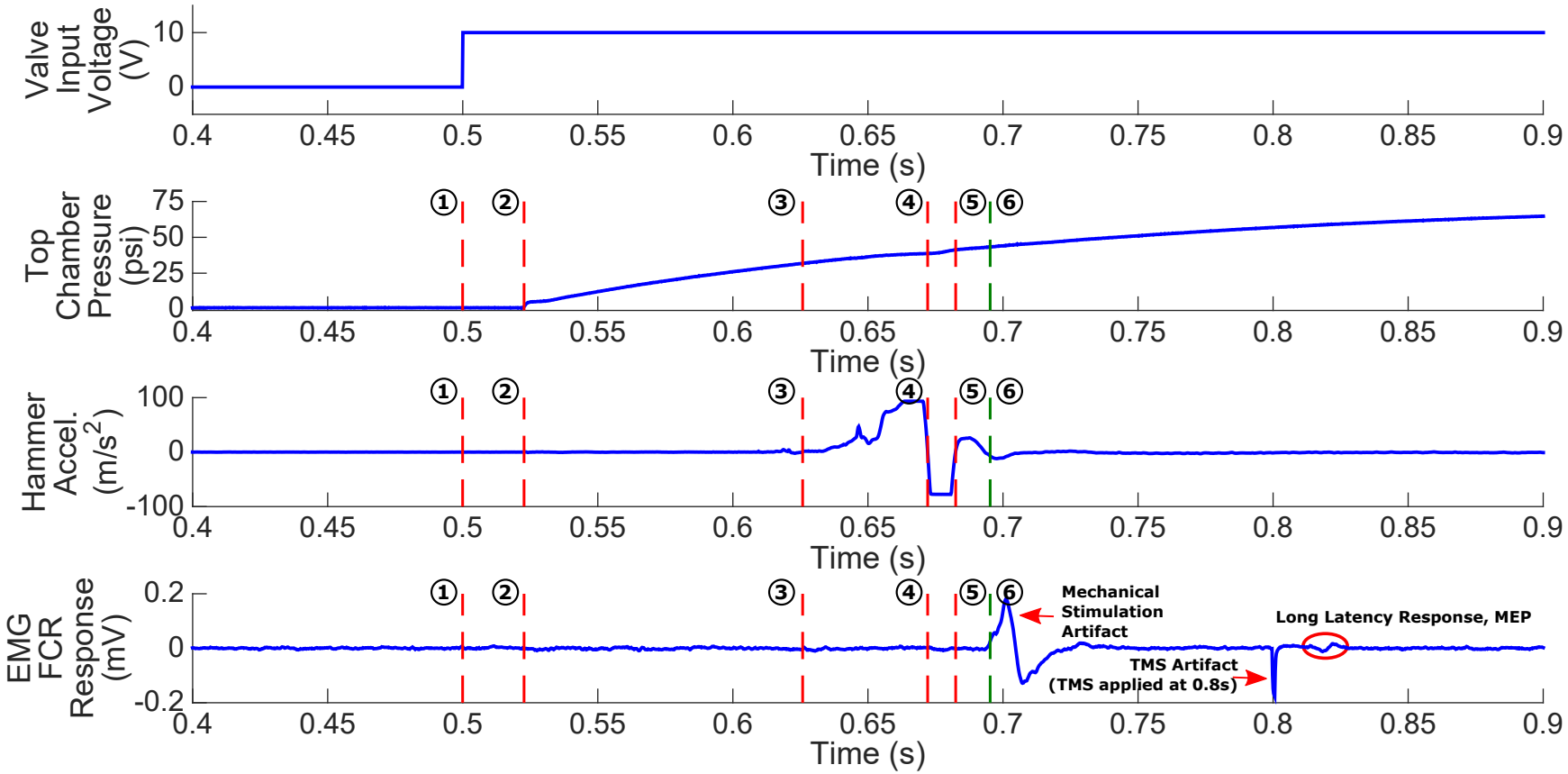

Figure 3.7: One trial with a subject. Timing delays sensor data. The data from Subject 2 was randomly chosen as a representative to show the shape of graph profile. Note that the data from the other subjects showed a similar profile. The red dashed lines represent following time points in order: 1) Valve starts to open (t_{i}), 2) Pneumatic cylinder starts to fill up (t_{fill}), 3) Hammer starts to move down ($t_{descent}$), 4) Hammer hits the object or tendon (t_{hit}), 5) Hammer rebounds away from the object or tendon (t_{away}). The green last dashed line represents the time when the EMG artifact is measured (t_{memg})

Table 3.1: Timing descriptions.

Notation	Description	Sensor Used
t_{i}	A full-scale (10v) signal is sent to the valve to start to push compressed air through the line connected to the top chamber of the pneumatic cylinder	Valve Input Voltage
t_{fill}	The top chamber of the pneumatic cylinder starts to fill up with compressed air	Pressure Sensor
t_{descent}	The hammer starts its downward descent	Accelerometer
t_{hit}	The hammer hits the object or tendon	Accelerometer
t_{away}	The hammer rebounds away from the object or tendon	Accelerometer
t_{memg}	EMG electrodes pick up the EMG artifact from the hammer strike	EMG electrodes

3.3.2 Timing Repeatability of Mechanical Stimulator

The timings of the events defined in Table 3.1 were collected for both the force sensor and experiments with four subjects. Results on timing repeatability are summarized in Table 3.2. In the force sensor experiments, the mechanical stimulator performed a total of 50 hits and the repeatability of impact timing were analyzed. Force sensor readings were used to detect t_{hit}. For human subject experiments, due to the variance of the range of ISIs that show long latency response among subjects, 538, 324, 252 and 346 different trials were recorded and analyzed for four subjects respectively. The timing delays presented in Table 3.2 were measured from the time that the pneumatic valve opened at t_{i}=0.5s. All timing data were processed and averaged for each subject as well as for the force sensor experiments. STD for all of the trials shown in the table was below 5ms, supporting the repeatability and timing accuracy of the mechanical stimulator. The timing delays of the top chamber filling up, $t_{\text{fill}} - t_{\text{i}}$, showed an average timing delay of 23ms with 0ms STD for all of the conducted experiments. The hammer extending time delays, $t_{\text{descent}} - t_{\text{i}}$, were

Table 3.2: Timing precision results. All values are in [ms].

		t_{fill}	t_{descent}	t_{hit}	t_{away}	t_{memg}
Force Sensor (n=50)	Average	523	621	688	690	N/A
	STD	0	2	1	1	N/A
	Range	[523, 523]	[617, 626]	[686, 690]	[689, 692]	N/A
Subject 1 (n=538)	Average	523	631	683	698	701
	STD	0	5	4	4	4
	Range	[523, 523]	[613, 640]	[669, 688]	[688, 704]	[689, 712]
Subject 2 (n=324)	Average	523	626	672	681	695
	STD	0	4	2	2	2
	Range	[523, 523]	[614, 650]	[666, 678]	[673, 688]	[689, 703]
Subject 3 (n=252)	Average	523	615	676	693	695
	STD	0	2	1	1	1
	Range	[523, 523]	[609, 625]	[674, 679]	[691, 696]	[692, 699]
Subject 4 (n=346)	Average	523	629	682	697	704
	STD	0	2	1	1	2
	Range	[523, 523]	[619,653]	[677,687]	[690,699]	[698,714]

121ms, 131ms, 126ms, 115ms and 129ms, respectively. These time delays had the biggest STD among all of the delays. Inner friction between the cylinder surface and piston may be a cause of the larger STD for this motion. The average hammer hitting time delays, $t_{\text{hit}} - t_{\text{i}}$, were 188ms, 183ms, 172ms, 176ms and 182ms, respectively. The STDs of the hitting time were 1ms, 4ms, 2ms, 1ms, and 1ms. Note that these t_{hit} were detected by the accelerometer measurement. The slight difference in values may be due to the subject's arm physical characteristics that contributed to a varying travel distance of the hammer. Overall, the mechanical stimulator can provide Mstim at a precise timing with little variability such as STD under 5ms. The timing repeatability results in Table 3.2 are shown in Figure 3.8.

3.3.3 Estimating Actual Impact Time for Each Subject

The timing delay between the EMG artifact and the hammer impact time, $t_{\text{memg}} - t_{\text{hit}}$, is shown in Figure 3.9. The timing difference was around 20ms. Physical attributes such as the length of the forearm and thickness of subcutaneous fat contribute to the slight difference between subjects. This time difference can be used to Estimate actual tendon stimu-

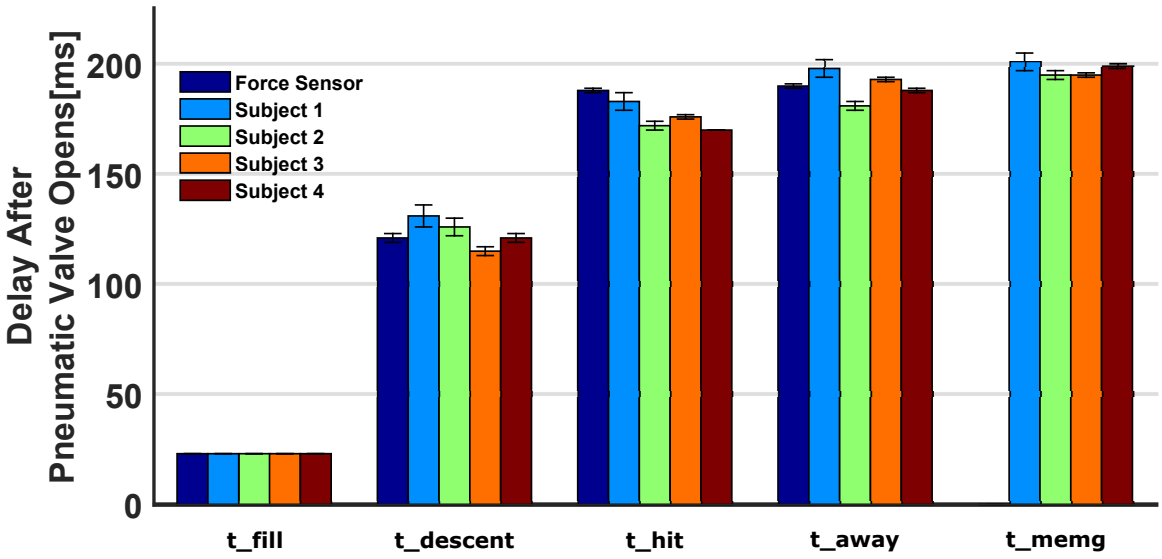

Figure 3.8: Time delays for all robotic actions during testing. Each bar length represents the time delay after pneumatic valve open at 0.5s. Robotic Actions 1 to 5 represents the following: 1) Top Chamber Fills up (t_{fill}), 2) Hammer Starts to Extend (t_{descent}), 3) Hammer Hits Hand (t_{hit}), 4) Hammer Bounces Back to Hand (t_{away}), 5) EMG Picks up (t_{memg}) Mech. Stimulus.

lation time by observing only the mechanical artifact of the EMG sensor since the STD of this timing difference is very small, less than 2ms.

The time duration, $t_{\text{away}} - t_{\text{hit}}$, is shown in Figure 3.10. This time delay shows the duration of time that the hammer presses down the tendon. It accounts for the spike shown in Figure 3.6. An example of this time delay in a human subject is shown in Figure 3.7. This hammer pressing delay was longer than the Estim which stimulates for a very short time period. This may contribute to the dispersed neural facilitation of Mstim which will be explained in section 3.3.4. In addition, each subject had different pressing delays as shown in Figure 3.10. This may contribute to the length of the effective ISI-W of Mstim which will be examined further in order to better understand the characteristics of Mstim.

3.3.4 Comparison of Long Latency Reflex with Electrical and Mechanical Stimulation

The number of long latency responses after PBS is compared for both Estim and Mstim. The timings considered in this comparison were the timing of Estim, t_{e}, the timing of

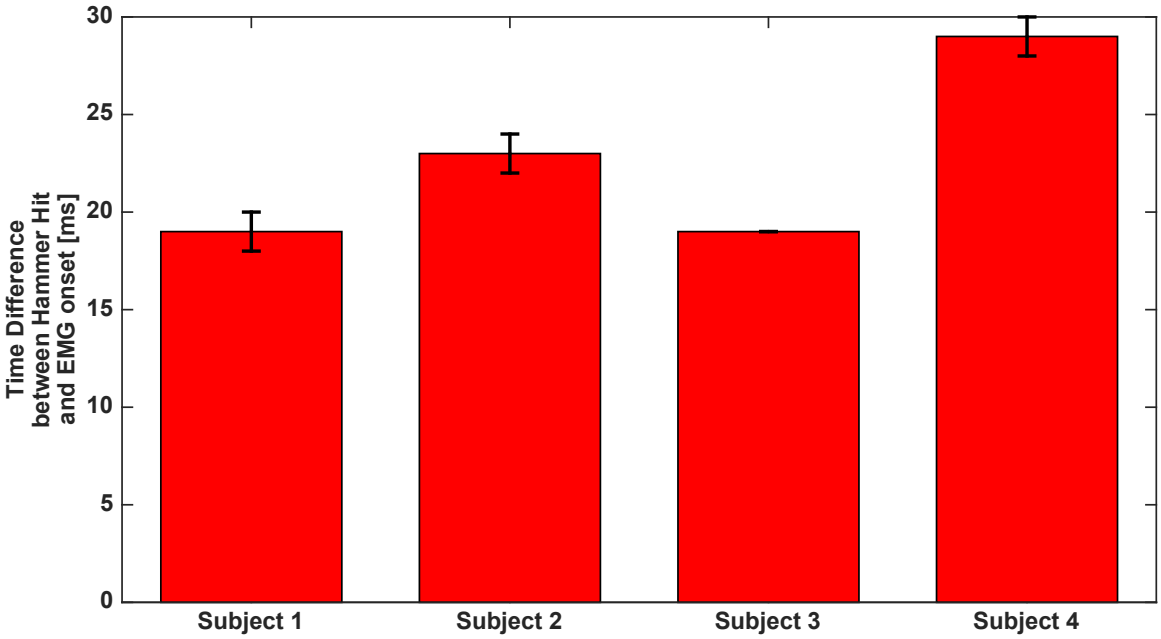

Figure 3.9: Time difference between hammer hit (t_{hit}) and EMG picks up mechanical stimulus (t_{memg}).

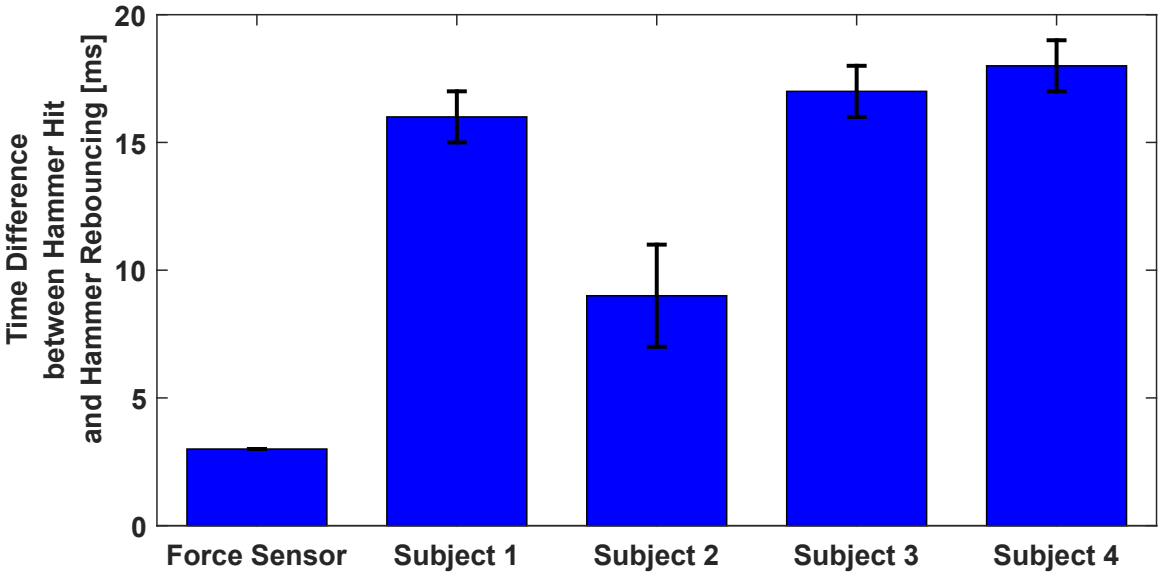

Figure 3.10: Time difference between hammer hit (t_{hit}) and hammer rebouncing (t_{away}), or hammer pressing duration.

Mstim, t_{hit}, and the timing of TMS application, t_{TMS}. EMG data are shown in Figure 1.7 when Mstim and TMS were applied with varying ISI to Subject 3. A response following TMS was considered to be a long latency response and counted when its MEP was greater than a certain threshold as shown in Figure 3.11. Each subject had a different threshold.

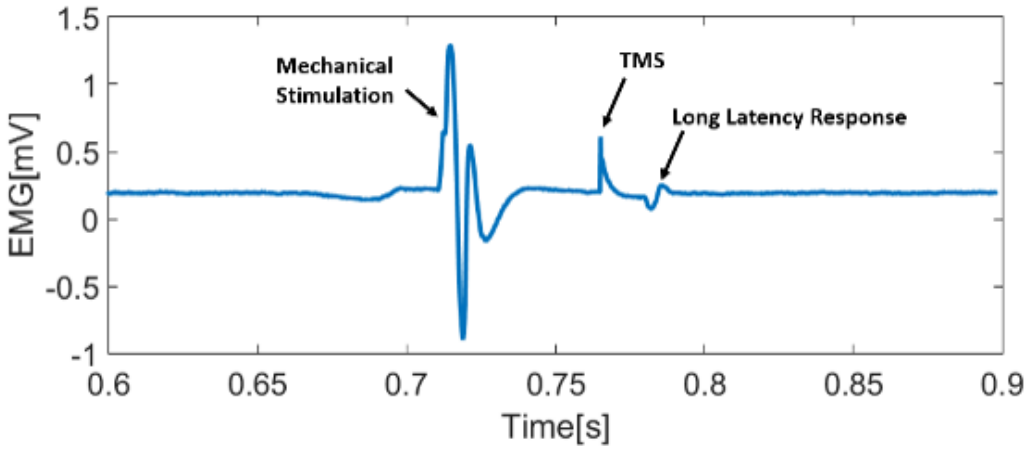

Figure 3.11: EMG with long latency response example.

This threshold will be explained further in chapter 4. The numbers of responses with varying ISI are displayed in Figure 3.12. This figure shows the ISI, $t_{\text{TMS}} - t_{\text{e}}$ or $t_{\text{TMS}} - t_{\text{hit}}$ on the x-axis, and the number of responses recorded for each ISI on the y-axis. The length of the bars represents the total number of trials for each ISI and green represents the number of observed responses out of the total trials during a certain time window. Yellow box represents the number of no responses. The varying timings of Mstim, which is shown to have a STD of 5ms, contribute to varying total trials for each ISI in the graph.

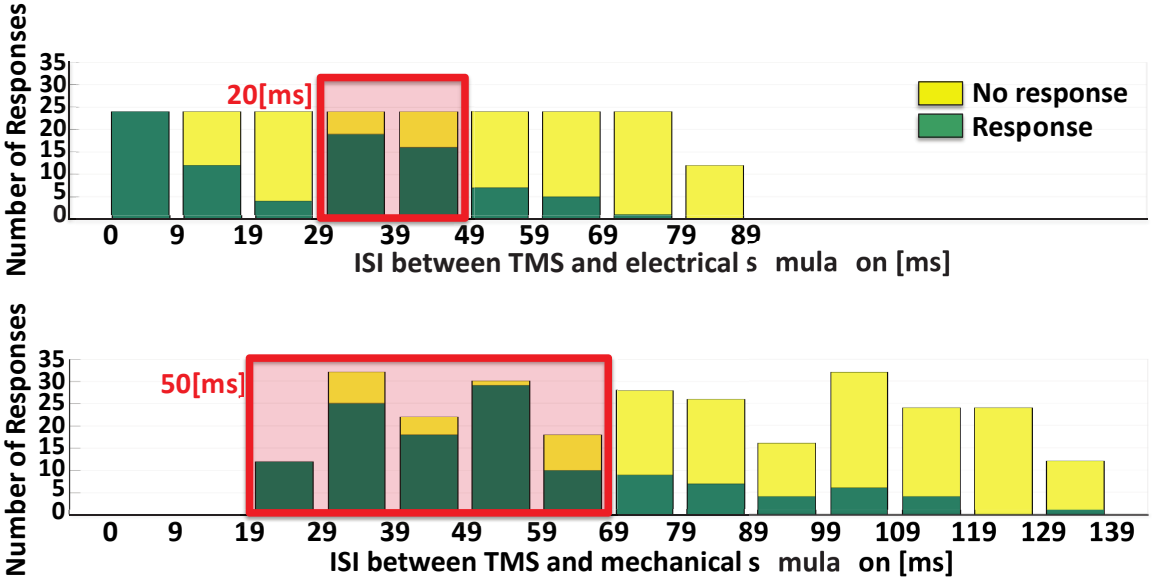

Figure 3.12: Effective ISI-W of electrical and mechanical stimulation.

When the number of long latency responses was counted to be more than 40% of all trials, it was defined as an effective ISI-W, the effective ISI-W is the range of ISI-W that induces facilitation. The effective ISI-W for Mstim was around 50ms, which is wider than Estim which was around 20ms. The first two time delay bars in Estim were not counted, because they were possibly due to short latency responses and not long latency responses. Mechanically induced long latency responses were shown may be in a dispersed time range because of the desynchronized activation of muscle spindles after Mstim. On the other hand, the muscle spindles activate synchronously during Estim, leading to a less dispersed time range of response. This larger effective ISI-W of Mstim is expected to help relax the timing precision requirement for synchronizing TMS and Mstim by the mechanical stimulator.

3.4 Contribution of the Work

This chapter presented results on Aim 1 of the research. With the accelerometer attached to the medical hammer, this device successfully detected tendon impact time, which is crucial information to record ISI. The mechanical stimulator showed a consistent time delay for Mstim with a high repeatability. The tendon impact time of Mstim was repeatable below 5ms STD for all trials. This repeatability of 5ms was accurate for tendon tapping regarding a 40-60ms neural facilitation window, or effective ISI-W, for Mstim which will be described in Chapter 4.

CHAPTER 4
EFFECTIVE TIME WINDOW ESTIMATION

The goal of this work is to develop statistical sampling and regression methods to efficiently model transient neuromodulations in the motor cortex via impact -based Mstim to muscles, using a robotic mechanical stimulator and paired cortical stimulation. An experimental identification of the exact timing and magnitude of neuromodulation in M1 of a person usually requires many test trials at different ISIs to individualize stimulation timings.

To mitigate this issue, the proposed procedure estimates individual ISI-W with sub-threshold TMS and Mstim. Statistical sampling and regression with relatively large time intervals (e.g., 5 ms) approximates the profile of Mstim-enhanced MEP with a reduced number of stimulation trials.

4.1 Problem Description

4.1.1 Need for Individually Adjusting Mstim and TMS Timings

Due to the large variability in the ISI window (ISI-W) for observations in Mstim-enhanced MEP in individuals, shown in Figure 4.2, an adjustment procedure must be performed on every subject before conducting actual neuroscientific research. Even within a single subject, the effective ISI-Ws measured at different days show huge variability as shown in Appendix B. Figure 4.2 shows the number of responses out of ten trials from eleven subjects. The number of responses were recorded by counting trials which MEP amplitude was greater than a predefined threshold value. These threshold values were tuned individually for each subject due to the individual difference in excitability level. The predefined threshold values were following; subject1: 0.026mV, subject2: 0.02mV, subject3: 0.03mv, subject4: 0.033mV, subject5: 0.015mV, subject6: 0.02mV, subject7: 0.03mV, subject8:

0.02mV, subject9: 0.03mV, subject10: 0.025mV, and subject11: 0.03mV. These values are determined by observing individual responses pattern. In the rest of the study, MEP amplitude were used to create ISI-W instead of the number of observations for several reasons; 1) With MEP amplitudes, the neural excitability changes according to ISI were observed directly, 2) ISI-W ranges based on the number of observations were highly sensitive to the threshold value, and 3) MEP amplitudes were easy to process for ISI-W estimation which will be explained in more detail in next Sections. ISI-W can also vary depending on the experimental arrangement, including mechanical variability associated with the tested muscle and employed Mstim. Mstim is an indirect method to stimulate the peripheral sensory organs by applying physical perturbation in the form of transient changes in pressure, velocity, and acceleration in the target peripheral tissues. These processes introduce additional dynamic factors, which lead to delayed and variable responses, such as skin and tendon stretch dynamics, muscle spindle discharge timings associated with the human sensorimotor system dynamics. In addition, air pressure propagation and development in the pneumatic system associated with the mechanical tendon tapping system also introduce delays.

The method of evaluating all responses across the set range and interval for identifying the ISI-W requires many data samples, which is laborious to the recipient of stimulation and makes the collection of a large data set time-consuming. For example, in the authors previous study [80], the initial range of ISIs for Mstim-subthreshold TMS neuromodulation was uniformly given to be 250 ms for all subjects where 12 Mstim trials were applied for 5-ms increments, totaling 600 Mstim trials. Including variable rest breaks between trials, the average duration to complete data collection for each individual in order to determine the ISI-MEP profile was approximately 2 hours (See 4.4.1).

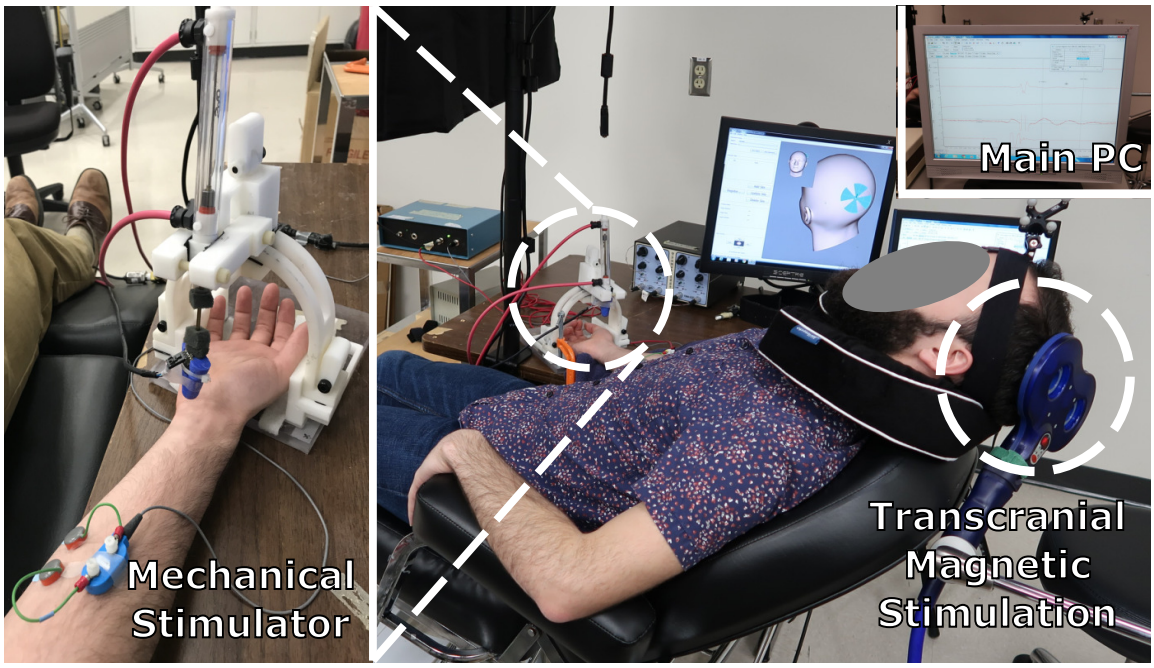

Figure 4.1: Experimental setup of peripheral Mstim and measurement of neuromodulation by means of TMS; a subject is lying down on a bed experiencing Mstim and TMS. Both devices are operated by the main computer.

4.2 Materials and Methods

4.2.1 Experimental Procedure

Healthy adult subjects (n=11) participated in this study from the pool at the Georgia Institute of Technology, Atlanta Campus. All subjects were between 18-30 years and were right-handed without a history of neurological disorders. The experimental procedure was approved by the Institutional Review Board (IRB) at the Georgia Institute of Technology (Protocol number: H14191). Subjects were asked to read and sign a consent form before the experiment.

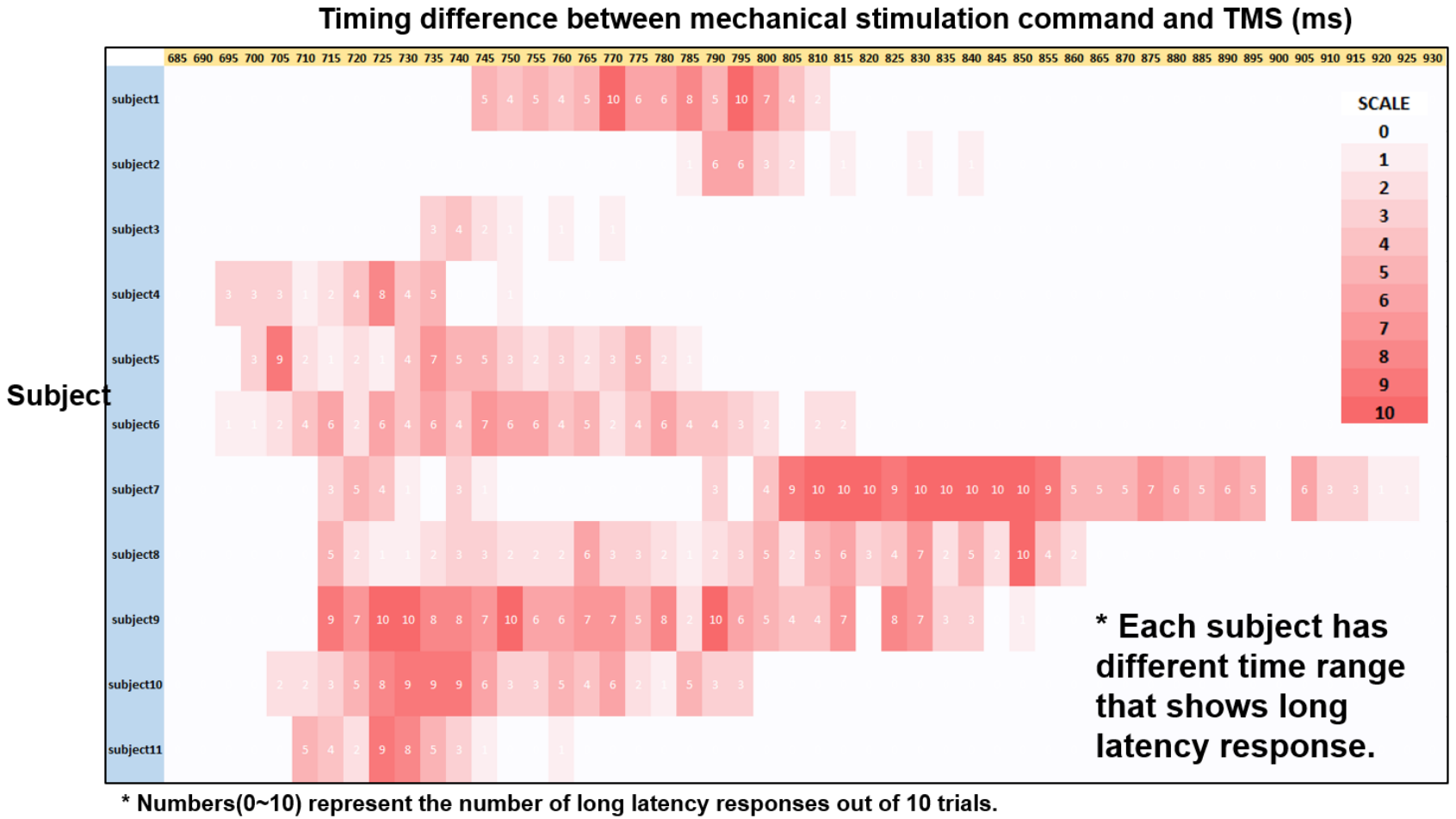

Figure 4.2: Number of responses from 11 individuals at different ISIs.

As shown in Figure 4.1, a subject was supine on a bed experiencing Mstim from the robot as well as TMS. TMS was applied over the motor cortex that is mapping to the flexor carpi radialis (FCR) muscle as shown in Figure 4.3, so called the FCR hot spot. This hot spot is the TMS coil location over the motor cortex with the lowest FCR rest motor threshold. In other words, the location was found by searching around locations which result in more than five MEPs above 0.05mV out of ten stimulation with the lowest TMS intensity. The location was stored with a TMS navigation system (NDI TMS Manager, Northerhn Digital Inc., Waterloo, Ontario, Canada) for repeatable placement of the coil. The timing of TMS and Mstim (i.e. t_{TMS} and t_{valve}, respectively) were controlled by Signal (Cambridge Electronic Design Limited, UK). The mechanical stimulator applied Mstim to the wrist tendon connected to the FCR muscle as shown in Figure 1.6. The impact timing (i.e. t_{hit}) was detected by an accelerometer attached on the hammer.

The robotic system was configured as illustrated in Figure 1.3. Two timing commands, t_{valve} and t_{TMS}, were sent from the host PC as shown in Figure 4.4. The resultant MEP amplitudes were recorded from the subject. To measure peak-to-peak MEP values of the FCR muscle for different ISIs, the surface EMG was used. Two Ag-AgCl electrodes (E224N, In Vivo Metric, Healdsburg, CA, US) were placed on the FCR muscle belly as shown in Figure 1.6 and Figure 4.5.

The accelerometer mounted to the medical hammer was utilized to measure the acceleration of the hammer and detect the onset of hammer tendon impact (t_{hit}). As shown in Figure 4.6, t_{hit} was determined by detecting the time where the acceleration crossed zero for the first time after the initiation of the hammer motion. Assuming negligible variability in t_{TMS} , ISI was calculated by $ISI = t_{\text{TMS}} - t_{\text{hit}}$. Note that t_{TMS} and t_{valve} were reference commands to the system. t_{hit} is a resultant timing point which is $t_{\text{hit}} = t_{\text{valve}} + t_{\text{delay}}$ as shown in Figure 3.3. In this thesis, five out of eleven subjects have measured acceleration data.

Enhanced MEP amplitudes were measured following the conventional procedure devel-

Figure 4.3: TMS stimulation location

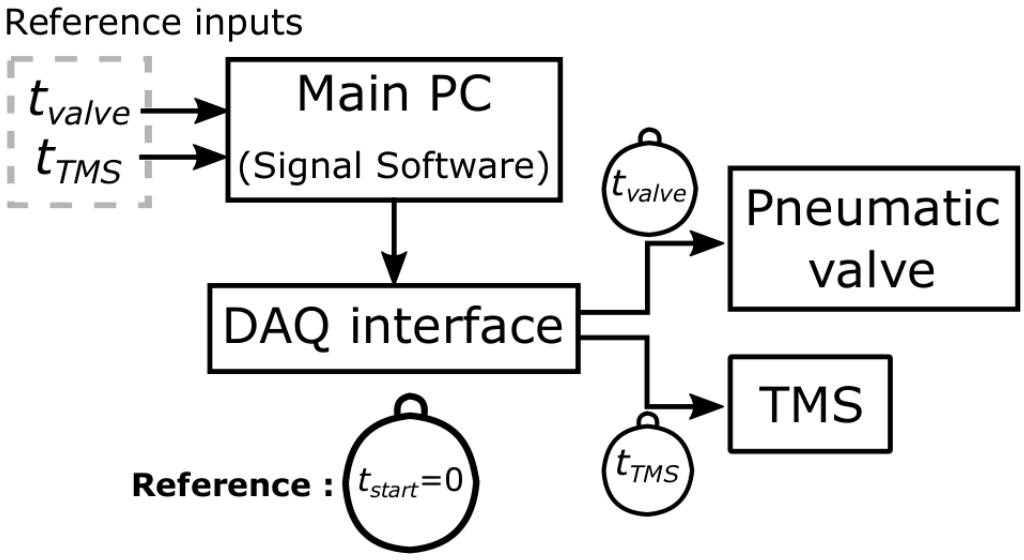

Figure 4.4: System configuration diagram. Main PC operates Mstim and TMS devices based on t_{valve} and t_{TMS} via a DAQ (Data Acquisition) interface.

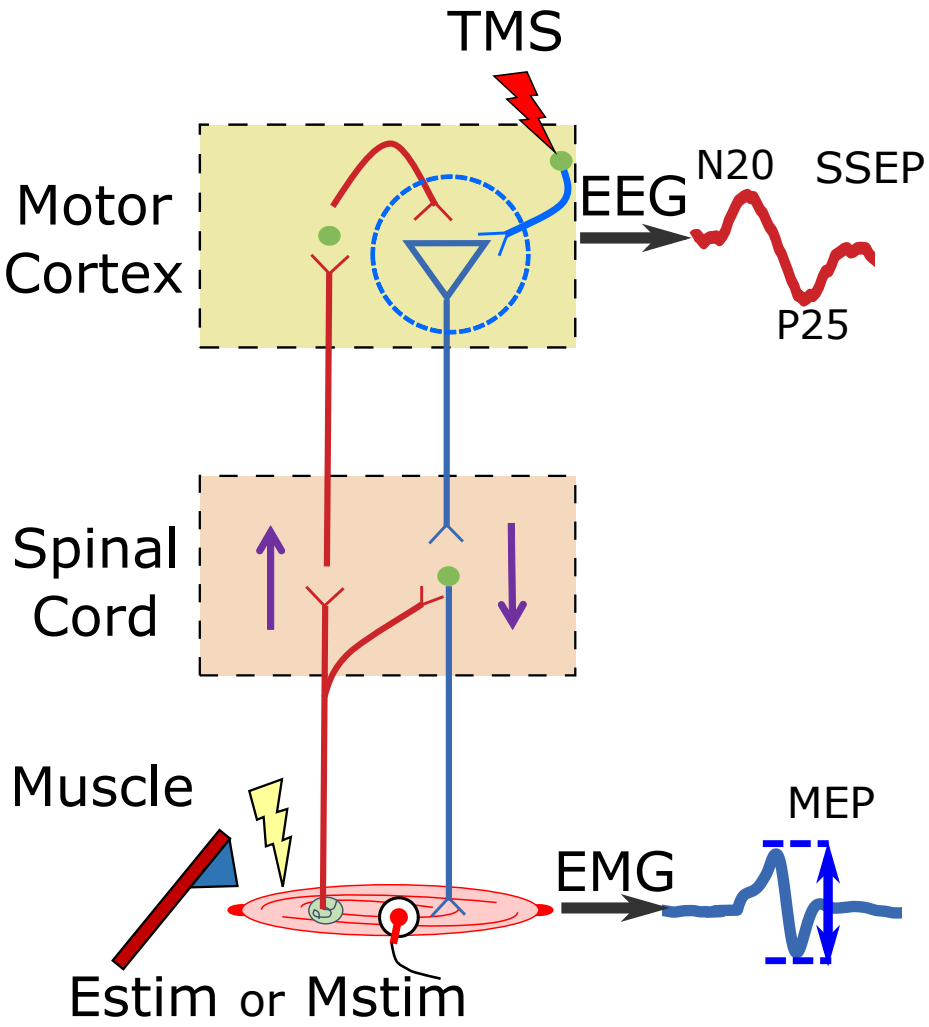

Figure 4.5: Schematic diagram of neuromodulation in the motor cortex induced by peripheral stimulation and observation of induced motor evoked potential.

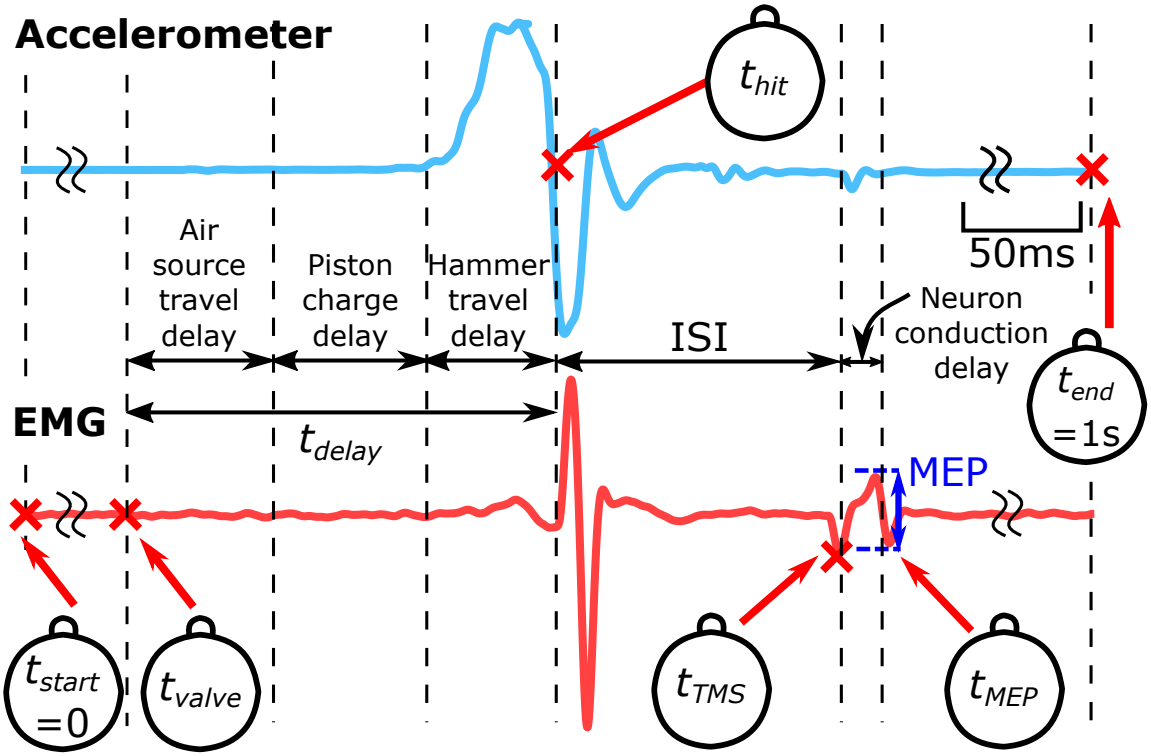

Figure 4.6: Representative acceleration and EMG measurement.

oped for Estim study. In the conventional method, the timing between t_{TMS} and t_{valve} was changed from 0 ms to 500 ms incrementally by 5ms as shown in Figure 4.7. Once all MEP amplitudes were recorded, the data was used as the ground truth for MEP modeling and ISI-W estimation. A series of ISIs where MEP measurements were above the baseline (i.e., MEP with 100% resting motor threshold TMS) indicated the neural enhancement. These ISIs were used to determine the effective ISI-W with sub-threshold TMS.

Note that in the conventional incremental procedure of MEP data collection, the experimenter expected a single distribution of MEP across ISI, and was allowed to manually terminate data collection when little or no MEP was observed after observing a distribution before reaching the longest searching time range of 500 ms. Without manual termination, a maximum of 600 trials was needed to incrementally sweep the entire search time range: Each mechanical stimulation took 1 second (1 second $\times$ 12 trials) followed by a 2-minute rest. Among 12 MEP measurements at a single ISI, the first two measurements

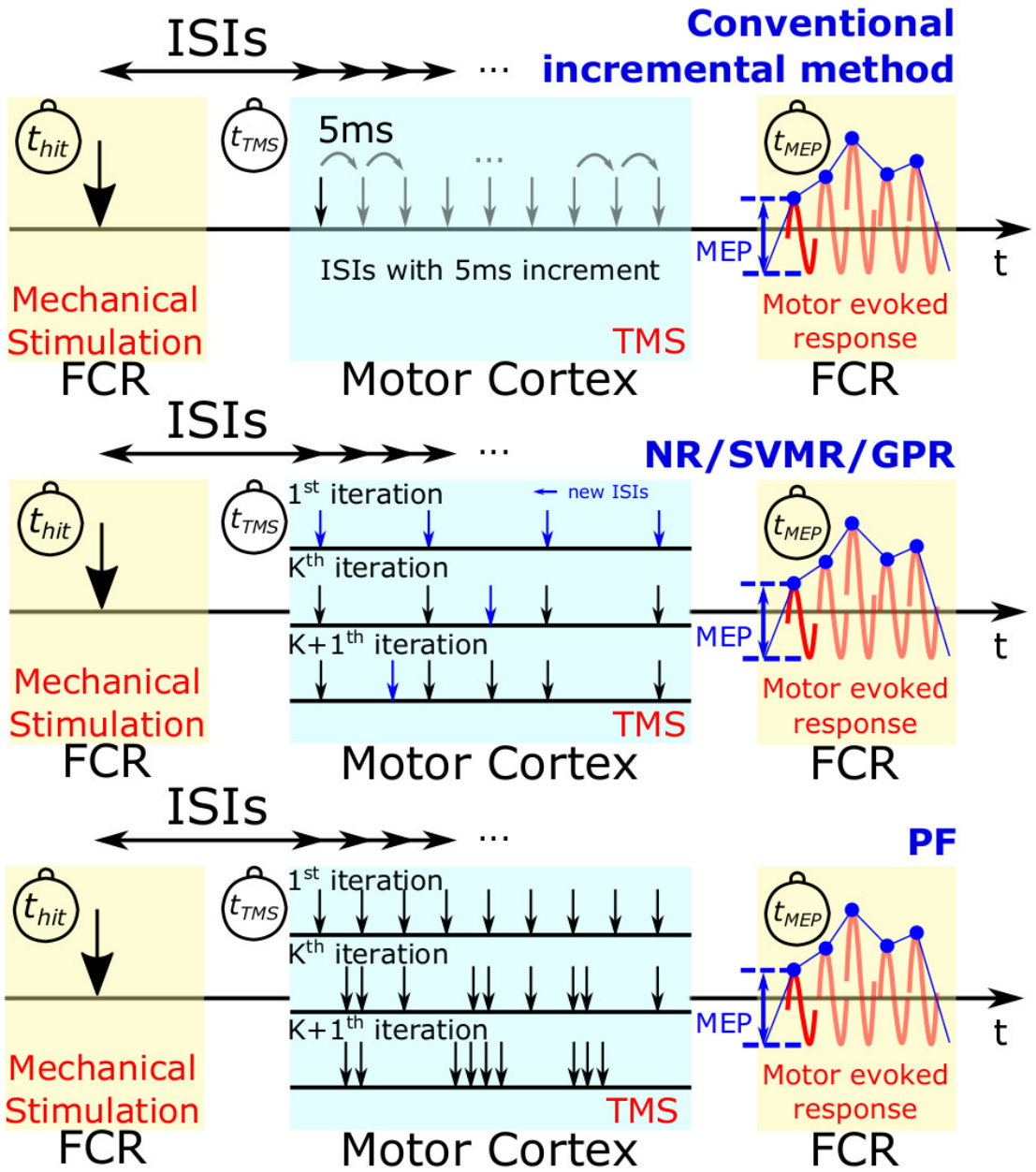

Figure 4.7: MEP sampling procedures for different regression methods to estimate effective ISI-W. Top: conventional incremental measurement of MEP. Middle: NR/SVMR/GPR. Bottom: PF.

were discarded and the last 10 measurements were recorded. The first two measurements were excluded due to the potential startle response. Two 5-minute-long breaks were given between sessions. As a result, the standard time to collect data from one subject was: (1s $\times$ 12 repetitions + 120s rest) $\times$ 50 intervals + 600-second-long rest $\times$ 2 = 130 minutes. By allowing the experimenter to manually terminate the experiment after there are no more observed responses at large ISIs, the average number of trials was reduced to 260, which was still almost an hour.

4.2.2 Evaluation of Timing Precision of Tendon Tapping

The mechanical impact timing delay and the precision of the tendon tapping robot were evaluated [7]. Two types of timing evaluation were conducted by applying mechanical impact to 1) a force sensor (LCM703-50, Omega Engineering Inc., Stamford, CT) fixed to a rigid floor and 2) the forearm of human subjects (a total of four). In the first evaluation, the one not involving a human volunteer, the force sensor was used to detect the measurement of t_{hit} for its faster response to impact than that of the accelerometers. A total of 50 trials were performed. In the second measurement, the impact applied on human subjects and accelerometer readings were used to detect the impact time (t_{hit}) as illustrated in Figure 4.6 and described in Figure 4.8. Data was collected from tendon tapping trials at an average of 365 trials per subject.

As expected, the tapping delay t_{delay} ranged from 172 ms to 188 ms among subjects primarily due to slight differences in the distance between the hammer's initial position and the target tendon position. However, within a single subject, a high repeatability was observed. By offsetting the mean time delay between the subject, the timing precision of the mechanical impact application was determined to be 2 ms in STD across all trials, and was judged that the tapping precision was sufficiently high with little variability to meet the timing precision of Mstim as shown in Figure 4.9.

Timing descriptions

Notation	Description
t_{start}	Start of a trial(t=0s)
t_{valve}	Main PC commands to open pneumatic valve (t=0.5s)
t_{delay}	Difference between thitand tvalve
t_{hit}	Hammer hits the target tendon
t_{TMS}	TMS stimulates the motor cortex
t_{MEP}	EMG electrodes pick up motor evoked response
t_{end}	End of a trial(t=1s)

Figure 4.8: Timing descriptions.

4.3 Statistical Regression of Enhanced MEP and ISI-W Estimation

A total of four methods have been implemented and compared to each other: 1) Nonlinear Regression with the Gaussian Model (NR), 2) Support Vector Machine Regression (SVMR), 3) Gaussian Process Regression (GPR), and 4) Particle Filter (PF). NR is one of the widely used regression methods that assumes a parametric nonlinear model of experimental data including biological data [85]. Based on the normality test described in the 4.4.8 section, a single-Gaussian Model was adopted as a parametric model to fit the measured MEP profiles for NR. SVMR is a nonparametric regression method based on a support vector machine (SVM). GPR is another nonparametric regression method that utilizes certain base functions that represent uncertainties in prediction as a Gaussian distribution, and may resemble the variability of multiple MEP measurements at a single ISI [86]. Nonparametric algorithms may be useful to model ISI-MEP data that does not nec-

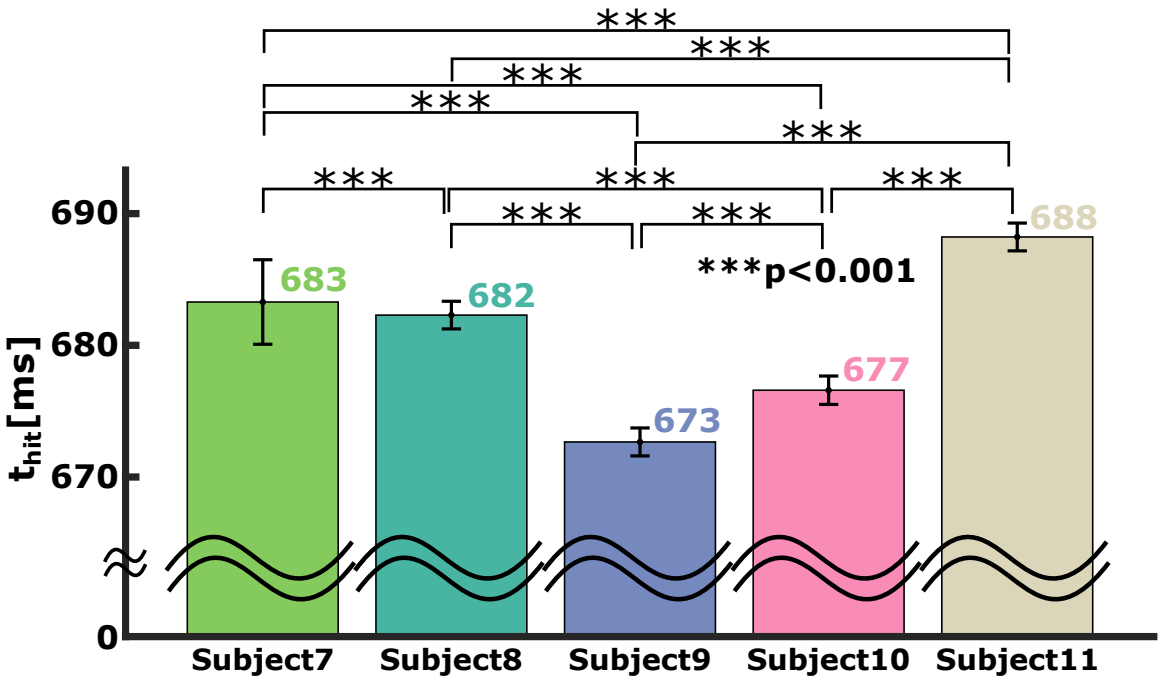

Figure 4.9: t_{hit} timing precision analysis (n=5). This shows the result of timing precision analysis of t_{hit} for five subjects. Mean t_{hit} values between the subjects were different with statistical significance, supporting the need for individual timing adjustment. Although the individual physical characteristics of the subject's arm may have contributed to the variability in the t_{delay}, the standard deviation of impact timing in each subject was found to be less than 2ms, which demonstrates the high-timing precision of the mechanical stimulator.

essarily fit a Gaussian model and perform regression with no assumption of the underlying function. On the other hand, nonparametric methods require many data points and take a long time to process. PF was previously implemented by the author [87] where 30 particles were adopted.

The top row of Figure 4.7 shows the procedure of the incremental method that incrementally changes the interval between t_{TMS} and t_{valve} by 5ms to sweep through the predefined searching range. PF distributes multiple particles (i.e., 30 measurements to observe enhanced MEP) within the searching range as shown in the second row of Figure 4.7. The locations of particles in the next iteration are updated based on the current observations. NR, GPR, and SVMR determine the next ISI to observe MEP in the next iteration based on the current observation and update of the model of MEP as shown in the third row of Figure 4.7. Figure 4.10 shows a representative estimation process with NR for one subject. The Gaussian model fits more closely with the measured MEP as regression progresses. In this particular trial, the initial number of observations is chosen to be 7 shown by red circles. Figure 4.11 shows a representative estimation process with SVMR and Figure 4.12 shows an estimation process with GPR.

MEP amplitudes corresponding to initially chosen ISI values were recorded and stored in a form of an array. Arrays of ISI and MEP amplitudes were fed into the NR, SVMR, GPR, and PF algorithms. The next ISI to evaluate MEP was determined based on updated prediction, completing one iteration. New ISI and corresponding MEP were added to the arrays for the next iteration. This procedure continued until predefined stopping criteria were met that are given as follows: Variances at the lower and upper ends of the modeled distribution were evaluated. Iteration was terminated when variances in the last five iterations of both the lower and upper ends were lower than 50, or iteration reached a maximum number of 99. The variance of 50 corresponds to 7ms standard deviation of the last five lower and upper ends. This is slightly greater than the 5ms increment of ISI, which tolerates one interval long (5ms) change of two end locations.

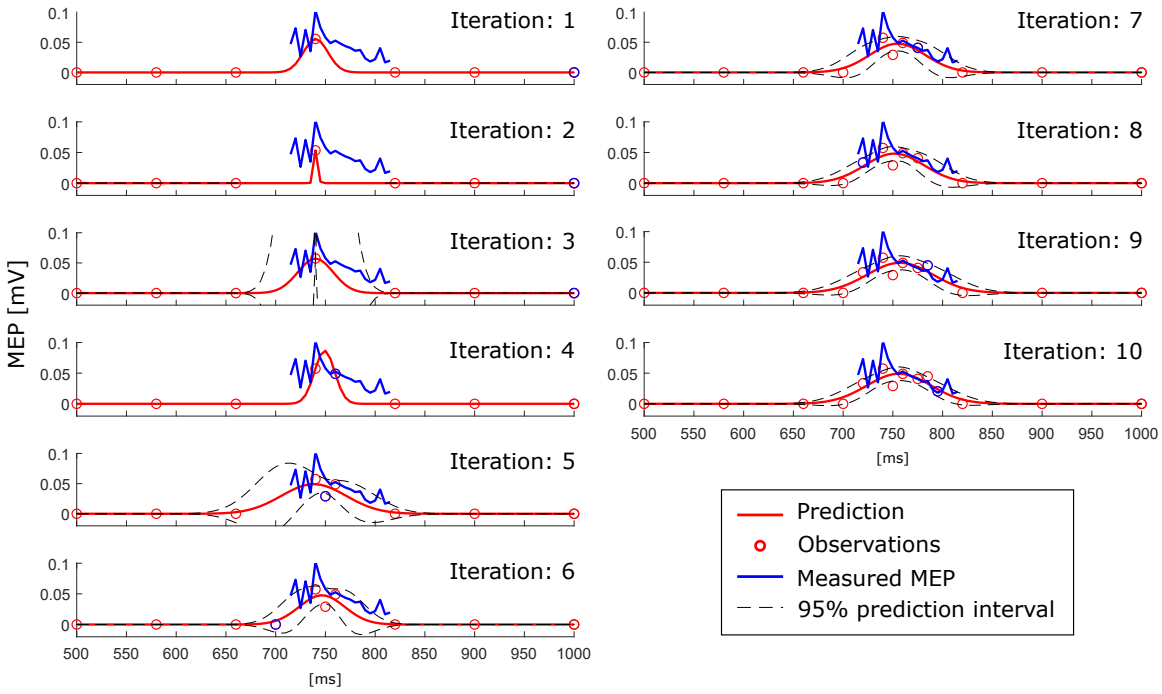

Figure 4.10: Example of estimation of enhanced MEP by NR with 7 initial observations. The blue circle indicates the most recent observation.

After the regression of MEP amplitude converged, a threshold method was applied to find the two ends of the Gaussian model to determine its ISI-W. For a Gaussian distribution, the range within two standard deviation (i.e., two sigma, or 95%) was used as an estimation of effective ISI-W as shown in Figure 4.13. 0.135 is the value of a normal distribution at two standard deviations from the mean. For the nonparametric SVMR and GPR, the same amplitude of 0.135 was applied to determine the ISI-W for consistency. The final estimated profiles from these methods had hill-shaped curves similar to Gaussian curves (See Figure 4.10, 4.11, and 4.12). Regression results of NR, SVMR, GRP and PF modeling MEP profiles are shown in Figure 4.14, 4.15, 4.16, and 4.17. For these estimated MEP profiles, the approximations were performed without using accelerometer measurements and started with n_{ini}=7. Among the methods, GPR tends to closely reproduce the MEP profile of the ground truth, as observed in the highest F1-score of the GPR. This is probably because of the characteristic of GPR where the covariance is almost unity when input observations, or ISIs, are close in distance, or zero, when they are highly distinct.

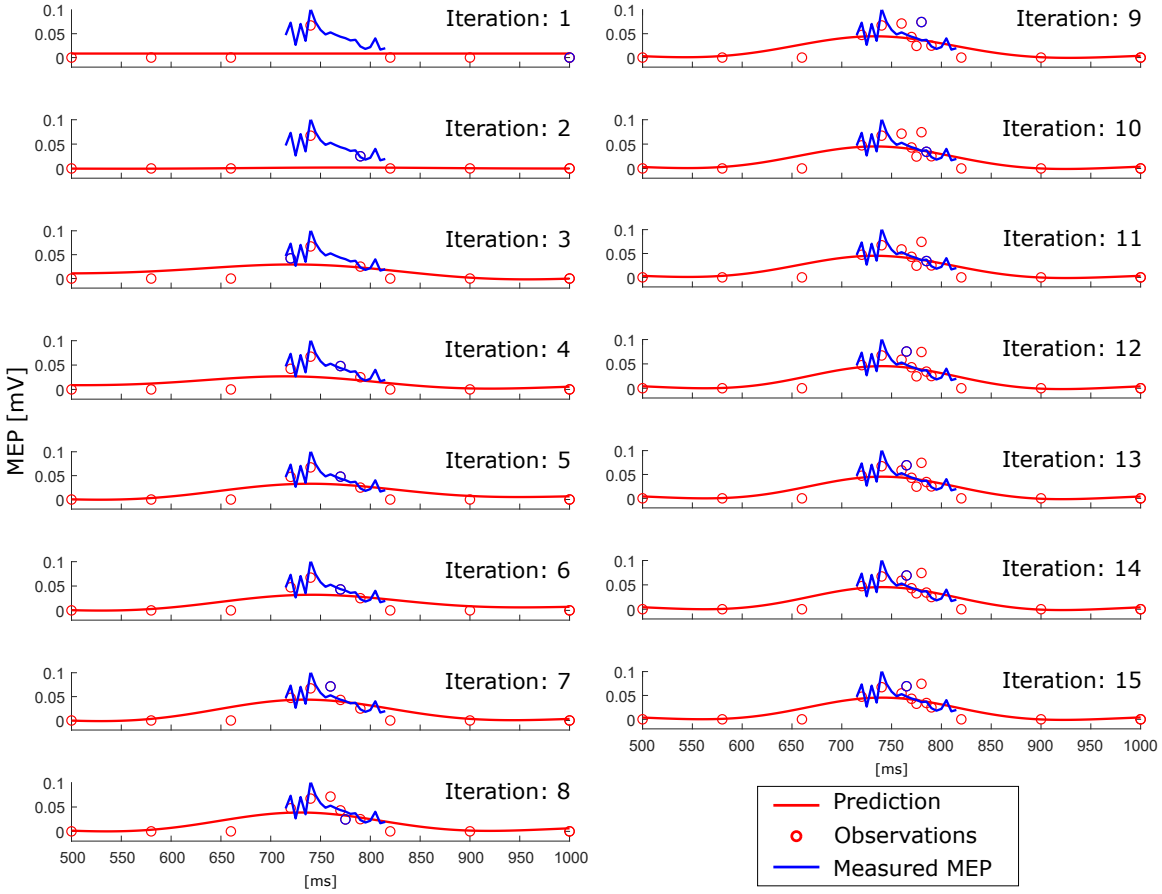

Figure 4.11: Example of estimation of enhanced MEP by SVMR with 7 initial observations. The blue circle indicates the most recent observation.

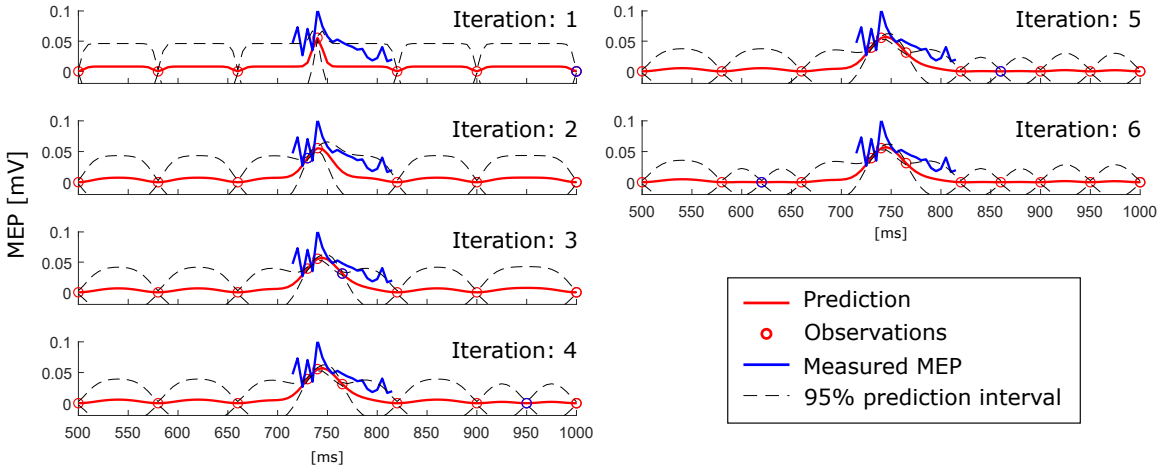

Figure 4.12: Example of estimation of enhanced MEP by GPR with 7 initial observations. The blue circle indicates the most recent observation.

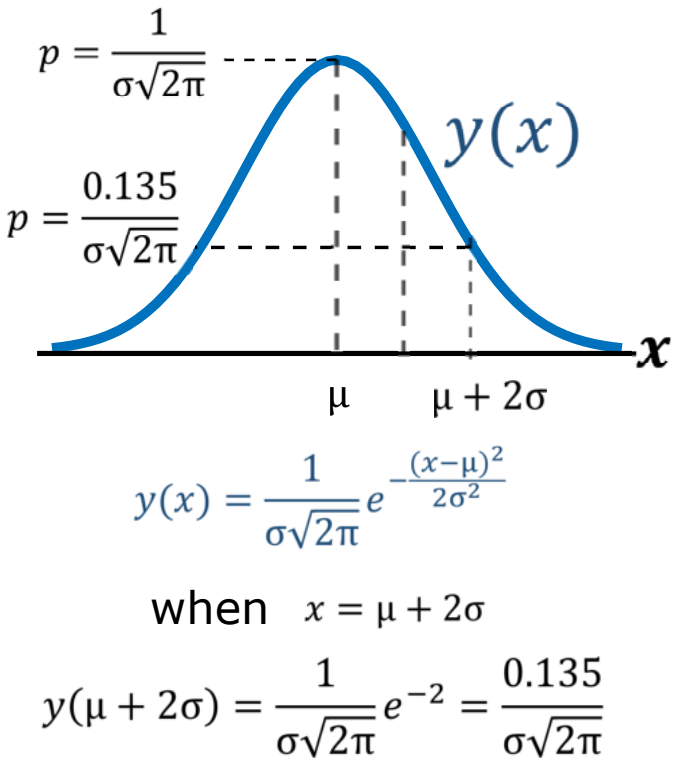

Figure 4.13: Determination of ISI-W from single-Gaussian fitting in NR and PF. Region within two standard deviations from the mean (i.e., two sigma) was used to determine ISI-W.

This tendency achieves MEP amplitude estimation near observed points of MEP. SVMR has a slightly greater average number of observations compared with GPR and NR. Due to nonparametric regression, SVMR tends to reproduce the overall shape of MEP amplitude including artifacts. This characteristic increases the number of iterations in the SVMR algorithm to meet the stopping criteria. NR and PF used a single-Gaussian model that demonstrated robustness to artifacts in Figure 4.18. Figure 4.19 shows how estimation of ISI-W progresses with GPR.

A number of observations refers to the number of MEP measurements before the algorithm stops. Cross correlation between an estimated MEP curve and a measured MEP profile as the ground-truth was evaluated. A correlation coefficient was determined using Pearson's linear correlation coefficient. An F1 score was calculated by evaluating a true positive, false positive, and false negative. The percentage of convergence is the percent-

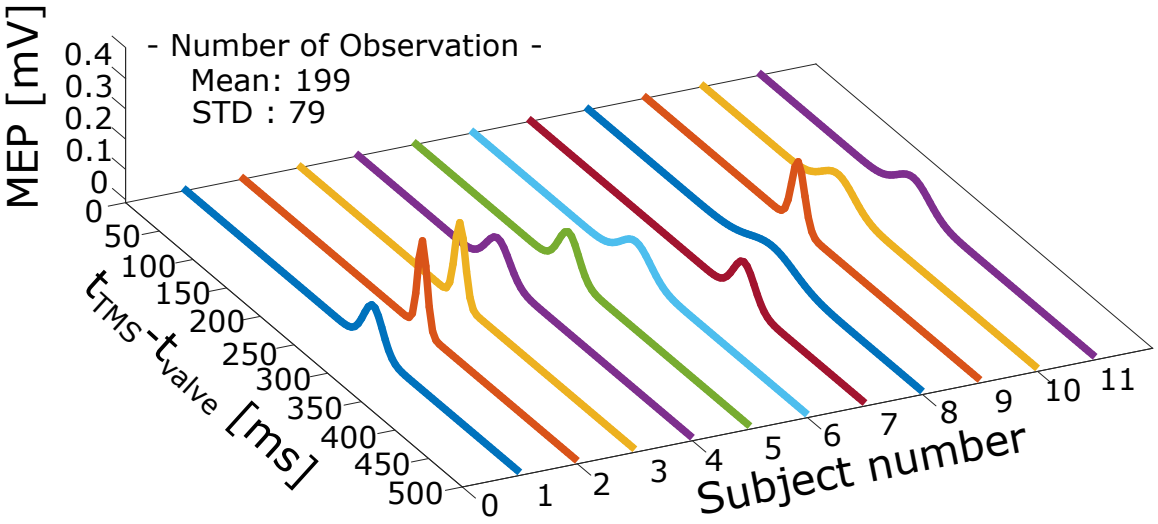

Figure 4.14: Regression results of PF

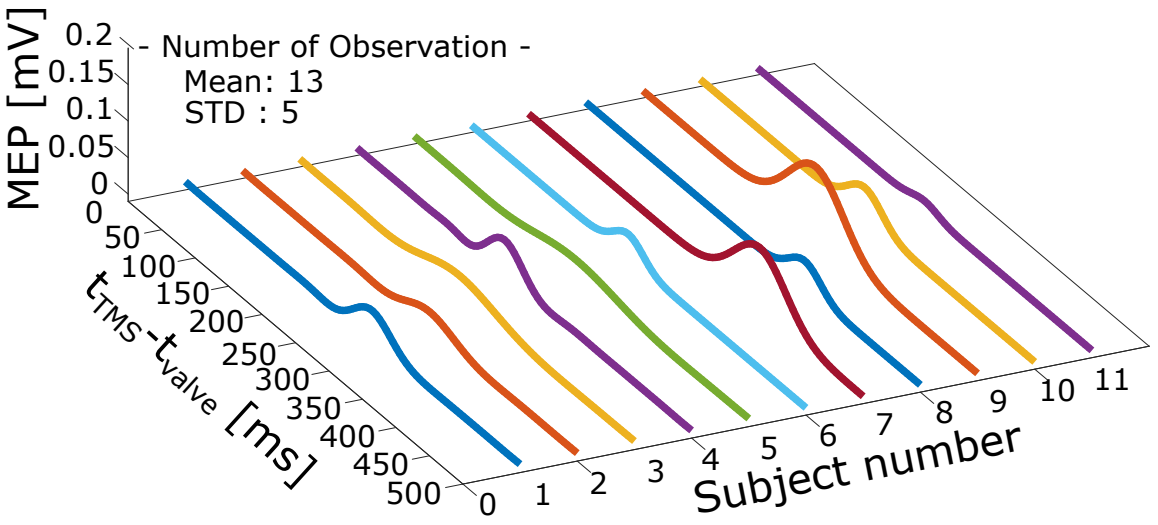

Figure 4.15: Regression results of NR

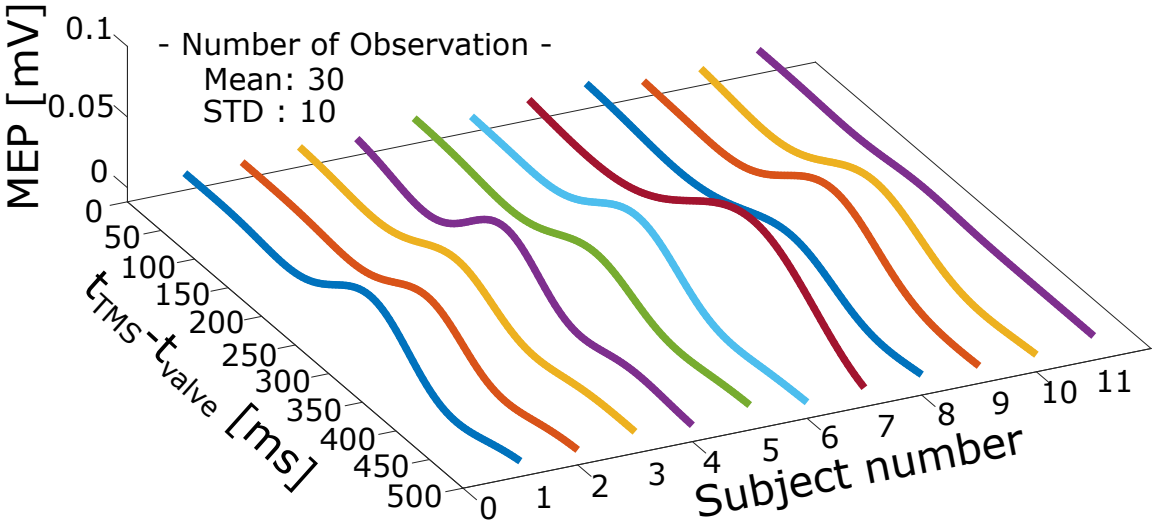

Figure 4.16: Regression results of SVMR

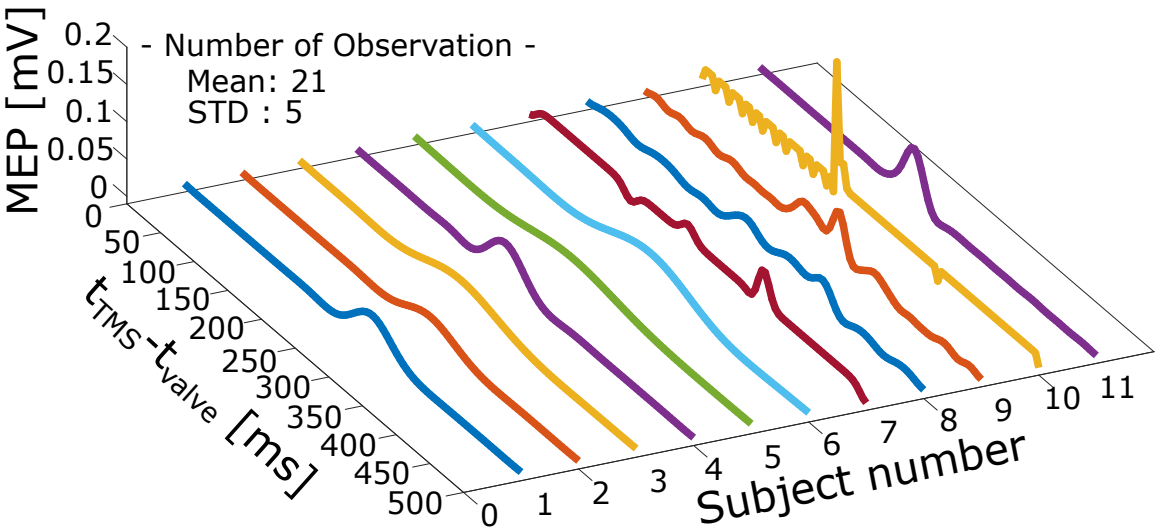

Figure 4.17: Regression results of GPR

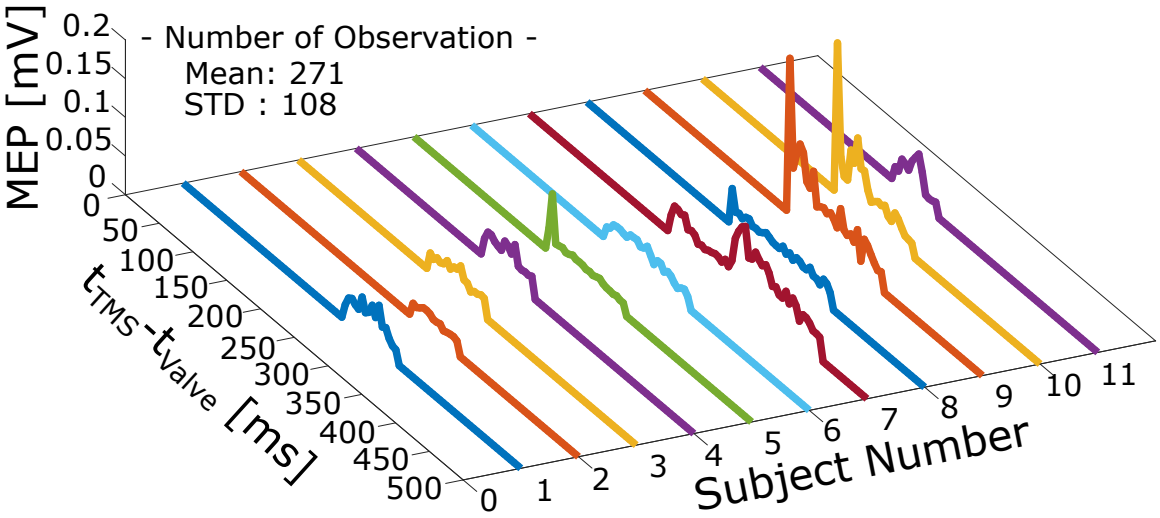

Figure 4.18: Ground truth MEP masurement

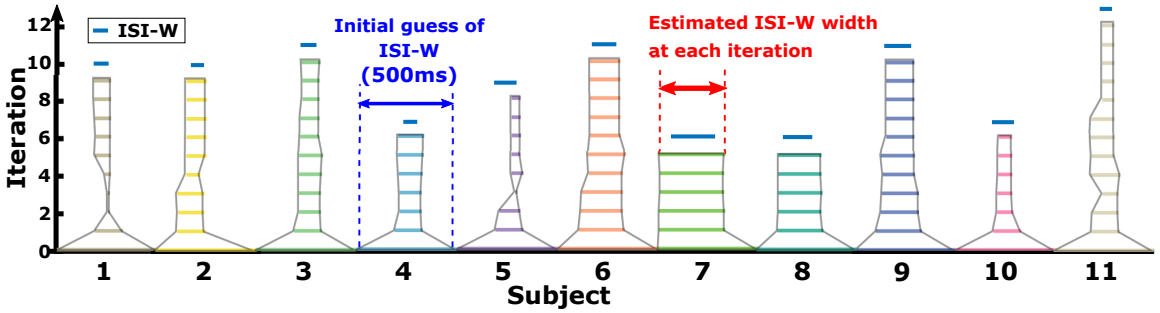

Figure 4.19: Result of ISI-W estimation with 7 initial observations by GPR. Horizontal bar represents estimated ISI-W at each iteration. The blue bar on top is ISI-W determined from the conventional incremental measurement as ground-truth.

age of trials that have converged before reaching the maximum iterations of 99.

4.3.1 NR, SVR, GPR and PF Procedure

NR, SVMR, GPR and PF procedures are shown in Algorithms 1,2,3 and 4

Algorithm 1: Nonlinear Regression for estimating individual ISI-W

---

procedure NONLINEAR REGRESSION

$\{t_{TMSinitial}\}$ ▷ Determine initial t_{TMS}

$iteration \leftarrow 1$

$t_{TMS} = t_{TMSinitial}$ ▷ Update t_{TMS}

while $variance1 \geq 50$ and $variance2 \geq 50$ and $iteration \leq 100$ **do** ▷ Stopping criteria

get $\{MEP(t_{TMS})\}$ ▷ Measure MEP for each corresponding t_{TMS}

$y_{regression} = f(t_{TMS}, MEP)$ ▷ Regression result from NR

$y_{regression}(ISI - W_{start}) = max(y_{regression}) * 0.135$ ▷ Find $ISI - W_{start}$

$y_{regression}(ISI - W_{end}) = max(y_{regression}) * 0.135$ ▷ Find $ISI - W_{end}$

$t_{TMSnext} \leftarrow acquisitionfunction$ ▷ Determine next t_{TMS} from acquisition function

$t_{TMS} = t_{TMSnext}$ ▷ Update t_{TMS}

if length($ISI - W_{start} \geq 5$) **then**

$variance1 = variance(ISI - W_{start}(end - 5 : end))$ ▷ Check variance

$variance2 = variance(ISI - W_{end}(end - 5 : end))$ ▷ Check variance

$iteration \leftarrow iteration + 1$ ▷ Repeat until convergence

return $y_{regression}$

Algorithm 2: Support Vector Machine Regression for estimating individual ISI-W

procedure SUPPORT VECTOR MACHINE REGRESSION
$\{t_{TMSinitial}\}$ ▷ Determine initial t_{TMS}
$iteration \leftarrow 1$
$t_{TMS} = t_{TMSinitial}$ ▷ Update t_{TMS}
while $variance1 \geq 50$ and $variance2 \geq 50$ and $iteration \leq 100$ **do** ▷ Stopping criteria
get $\{MEP(t_{TMS})\}$ ▷ Measure MEP for each corresponding t_{TMS}
$y_{regression} = f(t_{TMS}, MEP)$ ▷ Regression result from SVMR
$y_{regression}(ISI - W_{start}) = max(y_{regression}) * 0.135$ ▷ Find $ISI - W_{start}$
$y_{regression}(ISI - W_{end}) = max(y_{regression}) * 0.135$ ▷ Find $ISI - W_{end}$
$t_{TMSnext} \leftarrow acquisitionfunction$ ▷ Determine next t_{TMS} from acquisition function
$t_{TMS} = t_{TMSnext}$ ▷ Update t_{TMS}
if length($ISI - W_{start} \geq 5$) **then**
$variance1 = variance(ISI - W_{start}(end - 5 : end))$ ▷ Check variance
$variance2 = variance(ISI - W_{end}(end - 5 : end))$ ▷ Check variance
$iteration \leftarrow iteration + 1$ ▷ Repeat until convergence
return $y_{regression}$

Algorithm 3: Gaussian Process Regression for estimating individual ISI-W

procedure GAUSSIAN PROCESS REGRESSION
$\{t_{TMSinitial}\}$ ▷ Determine initial t_{TMS}
$iteration \leftarrow 1$
$t_{TMS} = t_{TMSinitial}$ ▷ Update t_{TMS}
while $variance1 \geq 50$ and $variance2 \geq 50$ and $iteration \leq 100$ **do** ▷ Stopping criteria
get $\{MEP(t_{TMS})\}$ ▷ Measure MEP for each corresponding t_{TMS}
$y_{regression} = f(t_{TMS}, MEP)$ ▷ Regression result from GPR
$y_{regression}(ISI - W_{start}) = max(y_{regression}) * 0.135$ ▷ Find $ISI - W_{start}$
$y_{regression}(ISI - W_{end}) = max(y_{regression}) * 0.135$ ▷ Find $ISI - W_{end}$
$t_{TMSnext} \leftarrow acquisitionfunction$ ▷ Determine next t_{TMS} from acquisition function
$t_{TMS} = t_{TMSnext}$ ▷ Update t_{TMS}
if length($ISI - W_{start} \geq 5$) **then**
$variance1 = variance(ISI - W_{start}(end - 5 : end))$ ▷ Check variance
$variance2 = variance(ISI - W_{end}(end - 5 : end))$ ▷ Check variance
$iteration \leftarrow iteration + 1$ ▷ Repeat until convergence
return $y_{regression}$

Algorithm 4: Particle Filter for estimating individual ISI-W

procedure PARTICLEFILTER

$\{x_0^{(1:M)}, \omega_0^{(1:M)}\} \sim p_0(.)$ ▷ Initialize particles and weights

$k \leftarrow 1$

while $variance \geq \epsilon^2$ **do**

for $i \leftarrow 1, \ldots, M$ **do**

sample $x_k^{(i)} \sim p\left(x_k | v_k, x_{k-1}^{(i)}\right)$

$\omega_k^{(i)} = p\left(z_k | x_k^{(i)}\right)$

$\omega_k^{(i)} = \omega_k^{(i)} / \sum_{i=1}^{M} \omega_k^{(i)}$

$\{x_k^{(1:M)}, \omega_k^{(i)}\} =$Resample$(x_k^{(1:M)}, \omega_k^{(1:M)})$

$p(x_k|z_k) = \sum_{i=1}^{M} \omega_k^{(i)} \delta(x_k - x_k^{(i)})$

$E\left[p(x_k|z_k)\right] = \sum_{i=1}^{M} \omega_k^{(i)} x_k^{(i)}$

$k \leftarrow k + 1$ ▷ Repeat until convergence

return $E\left[p(x_k|z_k)\right], p(x_k|z_k)$

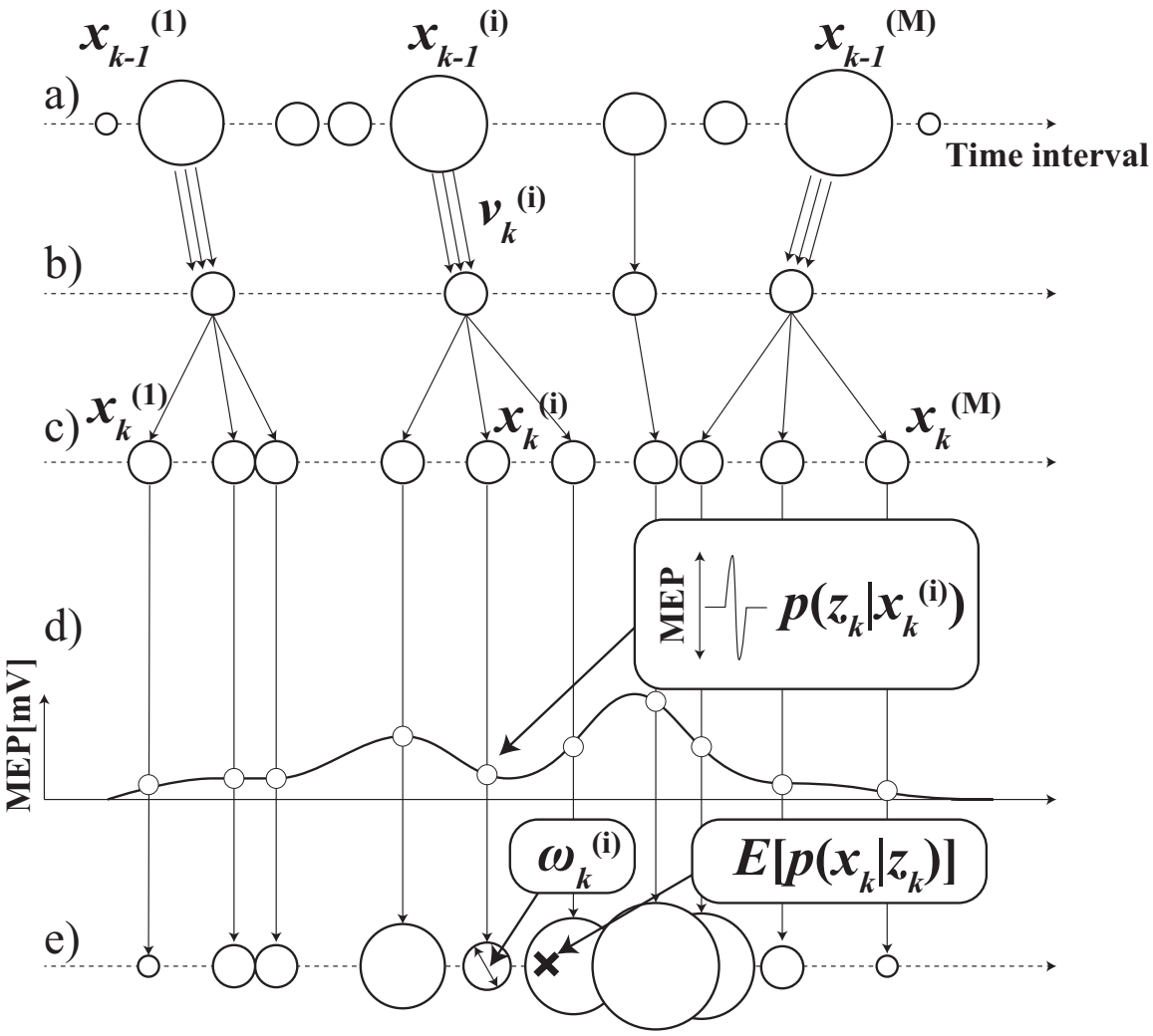

Figure 4.20: Particle Filter for estimating individual ISI.

4.3.2 Particle Filtering

The principle of the particle filter is illustrated in Figure 4.20, and the implementation is described below. Let k be the number of iteration ($k = 1, 2, 3, \cdots$). Consider M particles. The i-th particle is assigned to a discrete time of $x_k^{(i)}$ $(i = 1, 2, 3, \cdots, M)$ (with a time step of 5ms) with a weight of $\omega_k^{(i)}$ in the k-th iteration. The probability distribution $p(x_k)$ is defined as:

$$p(x_k) = \frac{1}{M} \sum_{i=1}^{M} \delta(x_k - x_k^{(i)}), \tag{4.1}$$

where $\delta(\cdot)$ is the Dirac delta function. The particles are then redistributed based on a Gaussian distribution representing the human system noise $v_k^{(i)}$ given as:

$$x_k^{(i)} = x_{k-1}^{(i)} + v_k^{(i)}. \tag{4.2}$$

The weights are updated based on MEP peak-to-peak values observed by redistributed particles. The particles are resampled based on measurement likelihoods by following the sequential importance resampling (SIR) filter proposed by Gordon [88]. The measurement likelihoods $p(z_k|x_k^i)$ are computed from MEP peak-to-peak values of the ISIs to which the redistributed particles are assigned. The normalized weights $\omega_k^{(i)}$ of particles are recomputed by:

$$\omega_k^{(i)} = \frac{p(z_k|x_k^{(i)})}{\sum_{i=1}^{M} p(z_k|x_k^{(i)})}. \tag{4.3}$$

As a result, each particle has a different weight as shown in Figure 4.20. The posterior distribution of effective ISIs, where a high value of MEP is observed, is computed from the particles and their weights as follows:

$$p(x_k|z_k) = \sum_{i=1}^{M} \omega_k^{(i)} \delta(x_k - x_k^{(i)}) \tag{4.4}$$

where the posterior expectation is also computed by

$$E\left[p(x_k|z_k)\right] = \sum_{i=1}^{M} \omega_k^{(i)} x_k^{(i)}. \tag{4.5}$$

Initial particles $x_0^{(i)}$ are uniformly distributed within the search time range with a uniform weight of $\omega_0^{(i)} = 1/M, \forall i$. A pseudo code of this particle filtering is shown in Algorithm 4. This process is iterated until the particles converge. Variance of the particles may

be used to observe the convergence. The convergence criterion is given by:

$$\epsilon^2 \geq \sigma^2 = \frac{1}{M} \sum_{i=1}^{M} \left(x_k^{(i)} - \bar{x}_k \right)^2 \tag{4.6}$$

where $\bar{x}_k$ is an average of the particles. ϵ= 25 [ms] was used for the current implementation. The posterior distribution is estimated within a 3σ ($\pm$ 75ms) interval with respect to the posterior expectation.

4.4 Experimental Results

4.4.1 Effective ISI for Observing Mstim-enhanced MEP

The author explored instantaneous and transient neuromodulation of M1 by observing the emergence of the combined effects of subthreshold Mstim to a wrist flexor tendon and a subthreshold TMS of M1 for a wrist flexor muscle (flexor carpi radialis) as shown in Figure 1.6. A subthreshold TMS (90% of resting motor threshold) was applied targeting the muscle at various ISI from Mstim, using the tendon tapping robot [80]. See section for details.

When the subthreshold Mstim or TMS alone was applied, the absence of an evoked response was confirmed as shown in Figure 4.21 top and bottom traces. With a combination of sub-threshold Mstim and TMS at various ISIs with 5-ms steps, evoked responses were observed (red arrows in the 2nd-14th traces) when the range of the time interval from the Mstim robotic command to TMS was 60 ms (i.e., from 245 ms to 305 ms) in this setup. Within this 60 ms window, the combined effect of Mstim and sub-threshold TMS was substantial enough to activate the motor neurons to observe enhanced MEP. Figure 4.22 shows a representative plot of enhanced MEP versus ISI with a subthreshold TMS in one subject showing an effective ISI-W of 70 ms (subject 4), but individual ranges of ISI-W were variable as shown in Table 4.1 (mean 108ms, std 45ms). Timing of the onset of Mstim also varied among subjects who had variable experimental arrangements.

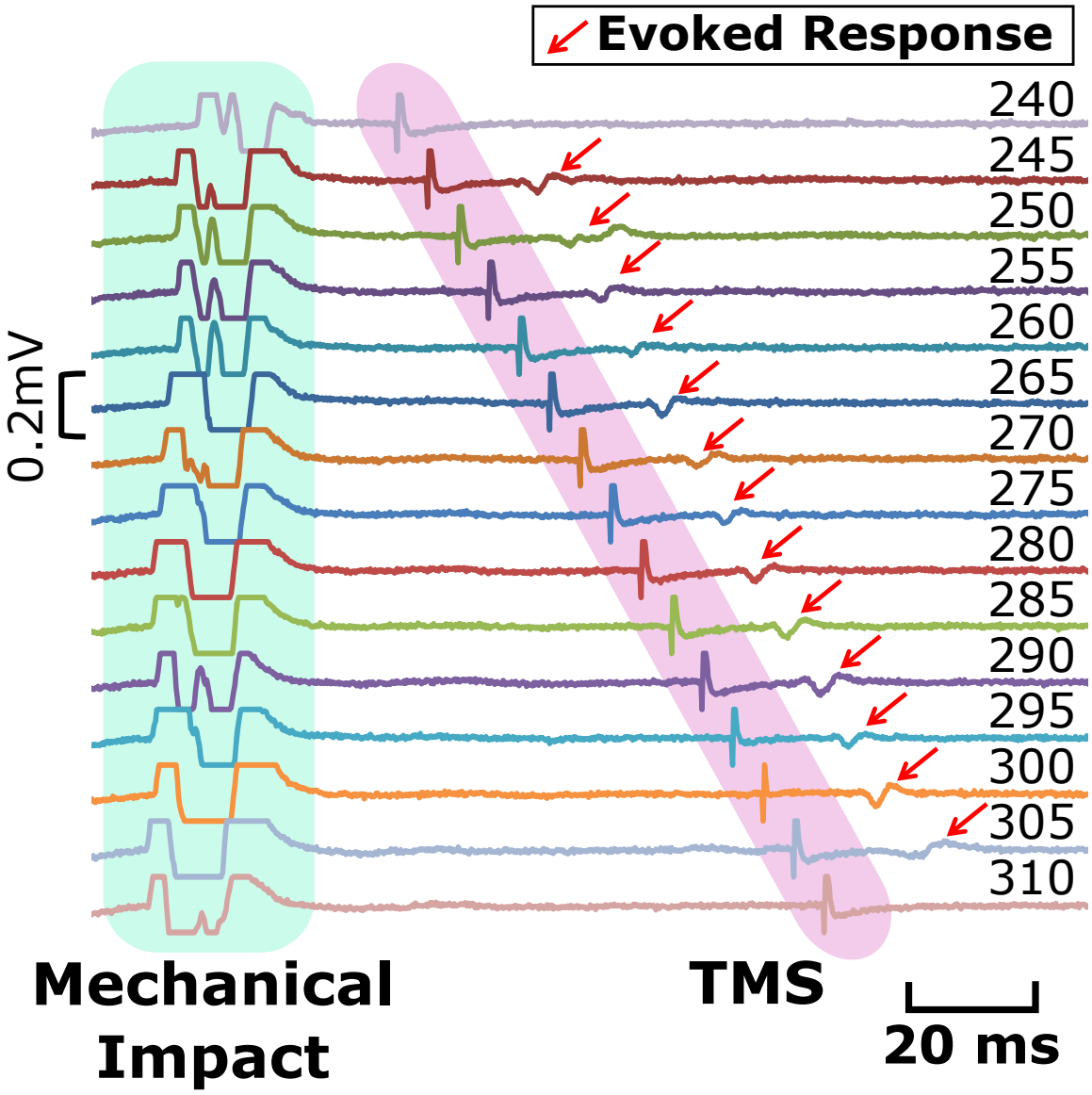

Figure 4.21: Enhanced MEP response with intervals between Mstim and TMS (Subject 1). Values shown at the right indicate time intervals in milliseconds between t_{valve} and t_{TMS}. t_{valve} was fixed and t_{TMS} was changed. Artifacts were observed in EMG due to both Mstim and TMS. Artifacts due to Mstim are not fully shown as the plots were trimmed to 0.2 mV and the mechanical impact timings are not fully shown. Red arrows indicate MEP when Mstim and TMS are overlapped over the motor cortex. Note that no MEP was observed on the top and bottom traces where the timing interval between Mstim and TMS was outside of the effective ISI-W that observes enhanced MEP.

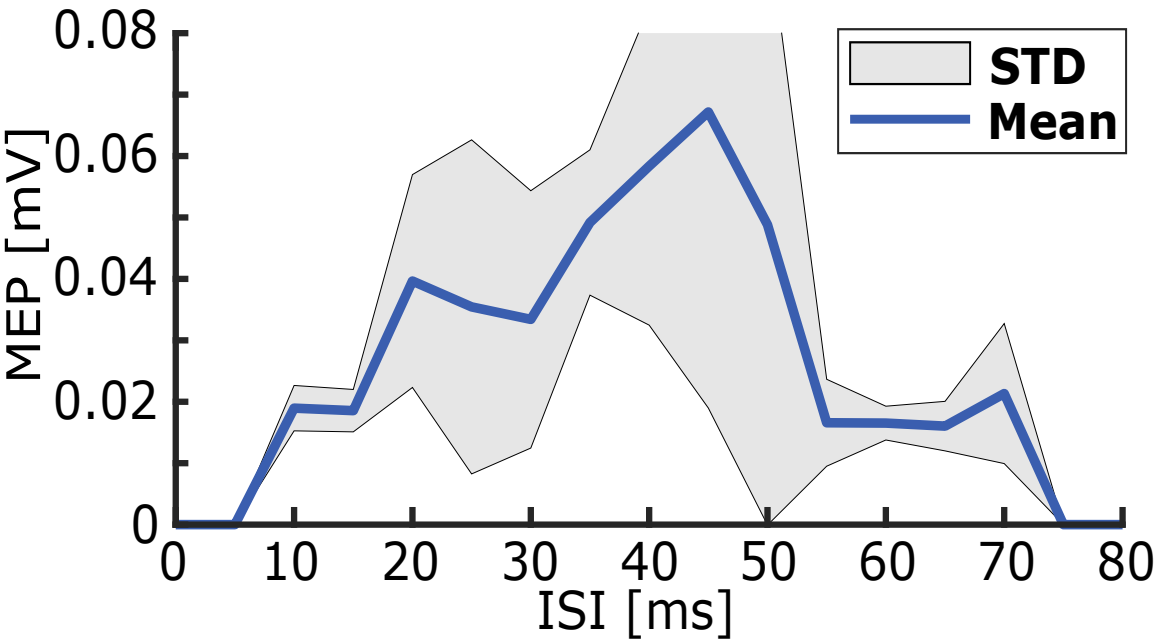

Figure 4.22: Enhanced MEP ISI-W with Mstim and sub-threshold TMS. Enhanced MEP amplitude changes with varying ISI ($t_{\text{TMS}} - t_{\text{hit}}$). MEP was measured for ten times at every 5-ms increment of ISI. Effective ISI-w to observe enhanced MEP was 70 ms (from 5ms to 75 ms) in this particular subject.

The width of an effective ISI-W due to Mstim is comparable to our observation of the reflex-based latency window size in a hand muscle (50ms) [72, 73]. When sub-threshold TMS was applied with sub-threshold Estim of the median nerve, however, the effective interval window size was 15-20 ms [89] which is supported by previously reported work [55]. Hence, the effective ISI-W size with Mstim appears to be larger than Estim, (i.e. more dispersed response), possibly because of the desynchronized activation of mechanoreceptors (e.g. muscle spindles) in response to Mstim. Mechanical peripheral stimulus produces a dispersed afferent volley in comparison to the impulse response to electrical stimulation. While this has been known since at least 1983 [90], limited work has investigated the mechanism for this diffuse firing or its impact on stimulation-based neuromodulation. These results confirm the presence of Mstim-induced transient neuromodulation of M1 and assure the importance of determining the effect in comparison to Estim.

Table 4.1: Normality test of enhanced MEP measurements.

	ISI-W width [ms]	Normality test
Subject1	75	pass
Subject2	65	pass
Subject3	80	pass
Subject4	70	pass
Subject5	110	pass
Subject6	120	pass
Subject7	220	fail
Subject8	145	pass
Subject9	135	fail
Subject10	110	fail
Subject11	60	pass
All	108 (STD:45)	8 out of 11

4.4.2 Reduction of Mstim-TMS trials for Individual ISI window Estimation

Previous studies utilized a fixed ISI or a few manually chosen ISIs [54, 45] to characterize neural responses associated with Estim. It should be noted that these ISIs were mostly determined based on empirical knowledge of neural conduction times. Other previous studies [58, 46] incrementally varied the interval between TMS and Estim to identify an ISI which would achieve the highest long-term potentiation in MEP amplitude. The presented work applied statistical sampling and regression methods to reduce trials for the estimation of individual ISI-MEP profiles by applying systematically chosen ISIs between Mstim and TMS, instead of incrementally sweeping a predetermined range of ISI.

In addition to individual differences, usually large variability in MEPs is observed in a single subject. ISI-W estimation methods must consider the stochastic nature of the human neuromotor system responses as shown in Figure 4.22 where large variation in MEP amplitudes was observed. The author has developed methods with other statistical regression tools for further improvement of ISI-W estimation performance as shown in Figure 4.7. In particular, a performance comparison was conducted between four statistical

estimation methods: 1) Nonlinear Regression with a Gaussian Model (NR), 2) Support Vector Machine Regression (SVMR), and 3) Gaussian Process (GP), in addition to the previously reported 4) Particle Filter (PF). Details are described in Materials and Methods.

All of the regression methods required a certain number of initial observations distributed within an initial guess of ISI-W. When the accelerometer is available, it can detect the onset of Mstim or t_{hit}. The period between t_{valve} and t_{hit} can be excluded from regression as facilitation must occur after t_{hit}. The use of the accelerometer helps to narrow the search-range that may improve performance.

Performance was evaluated based on 1) the total number of observations, 2) cross correlation, 3) F1 score, and 4) the percentage of convergence. Numbers of observations required for convergence are shown in Figure 4.24. All the regression methods significantly reduced the number of observations compared with the conventional incremental method that required an average of 272 observations when the experimenter was allowed to manually terminate data collection. While PF improved the performance, It still required many more observations and produced greater variance than NR, SVMR and GPR did. On average, NR, SVMR, and GPR required an order of magnitude smaller observations than PF and the conventional incremental method with smaller variance. The use of the accelerometer further improved the performance by reducing the number of observations up to 56%. The results of a cross correlation analysis is shown in Figure 4.23, evaluating how close the estimated MEP profiles were to the profiles from full measurements as the ground truth. Overall GPR showed the highest correlation coefficient. GPR's correlation coefficient was 31.67% higher than that of NR (p <0.05), and 12% higher than that of PF (p <0.05). SVMR's correlation coefficient was 16.67% higher than that of NR (p <0.05). There was no statistical significance difference observed between SVMR & GPR, NR & PF and SVMR & PF. The F1 score is an appropriate evaluation metric to evaluate the accuracy of ISI-W estimation as shown in Figure 4.25. Among the methods, GPR obtained an F1 score greater than 0.8. The use of the accelerometer overall improved performance. As

shown in Figure 4.26, there were a small number of cases that did not converge and reach the maximum number of iterations, showing satisfactory robustness to different data sets.

Overall for mPBS paired with sub-threshold TMS, a single Gaussian model worked well to estimate the ISI-W. The total number of observations required was only 6.5% of that of the conventional incremental method for NR. NR would be a good choice in terms of reducing the number of observations. GPR would be a good choice in terms of improving F1 score. There was a trade-off between the parametric methods and nonparametric methods. Parametric methods tended to lower the number of observations, but also reduced the F1 score. Nonparametric methods tended to improve the F1 score, but also increased the number of observations. NR was sufficient to approximate the ISI-W with relatively high F1 score and the lowest number of observations. In some cases, GPR resulted in over fitting due to the nature of GPR procedure. Estimation performance may be further improved by optimizing the parameters.

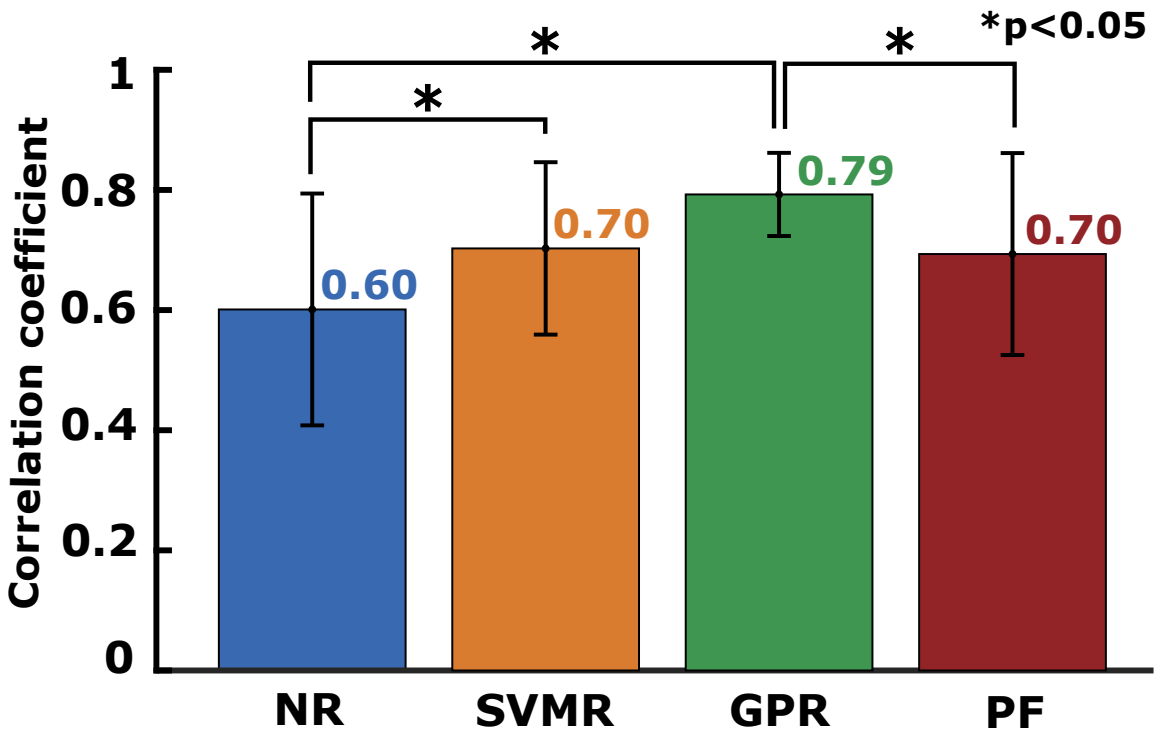

Figure 4.23: Correlation analysis of MEP profile estimation. Correlation coefficients comparing estimated MEP profiles and MEP measurements as ground-truth. Initial number of observations, 6, 7 and 7, were used for NR, SVMR and GPR respectively and 30 particles for PF (n=11).

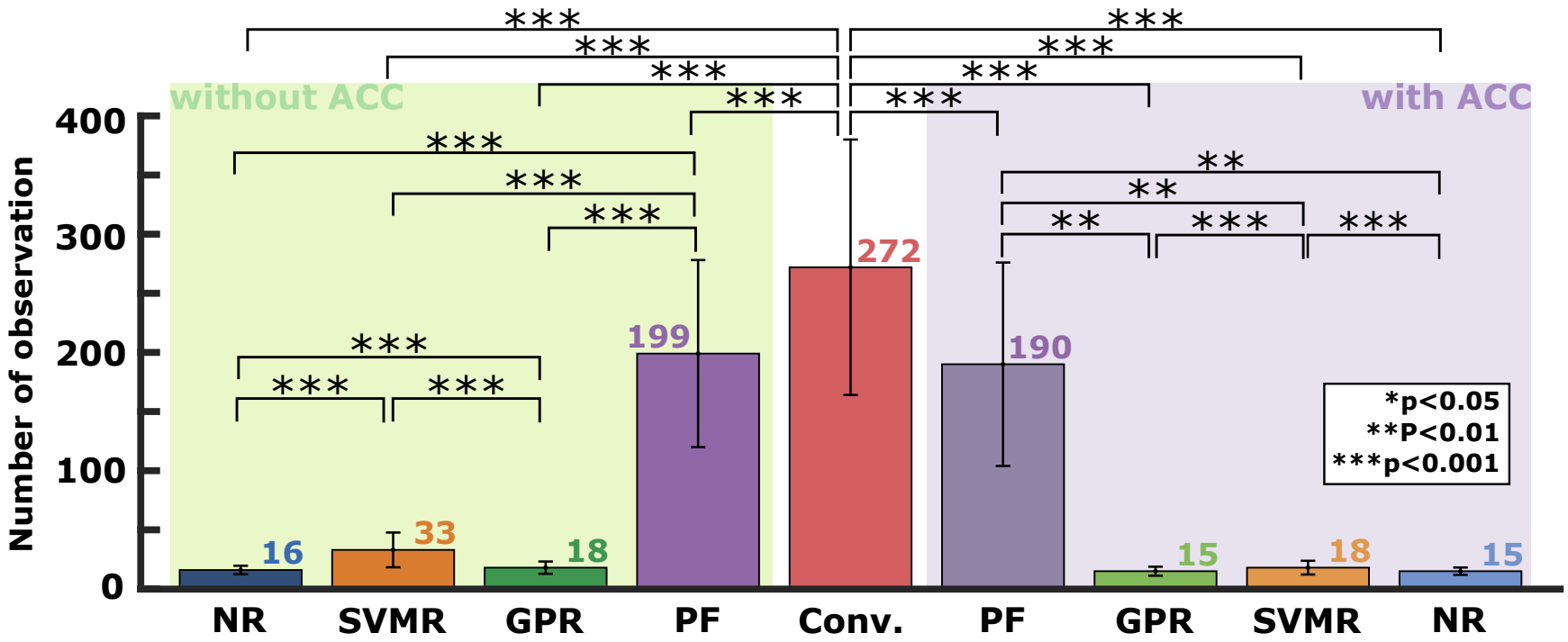

Figure 4.24: Numbers of total observations to obtain final estimation of ISI-W. For the conventional incremental measurement method (center bar), the total number of observations varied allowing the experimenter's judgement to terminate the trial where a maximum of 600 observations were required to fully sweep the predetermined search window without manual termination. In the left half, bars show results without the use of the accelerometer (ACC) (n=11). In the right half, bars show results with the use of the accelerometer (n=5).

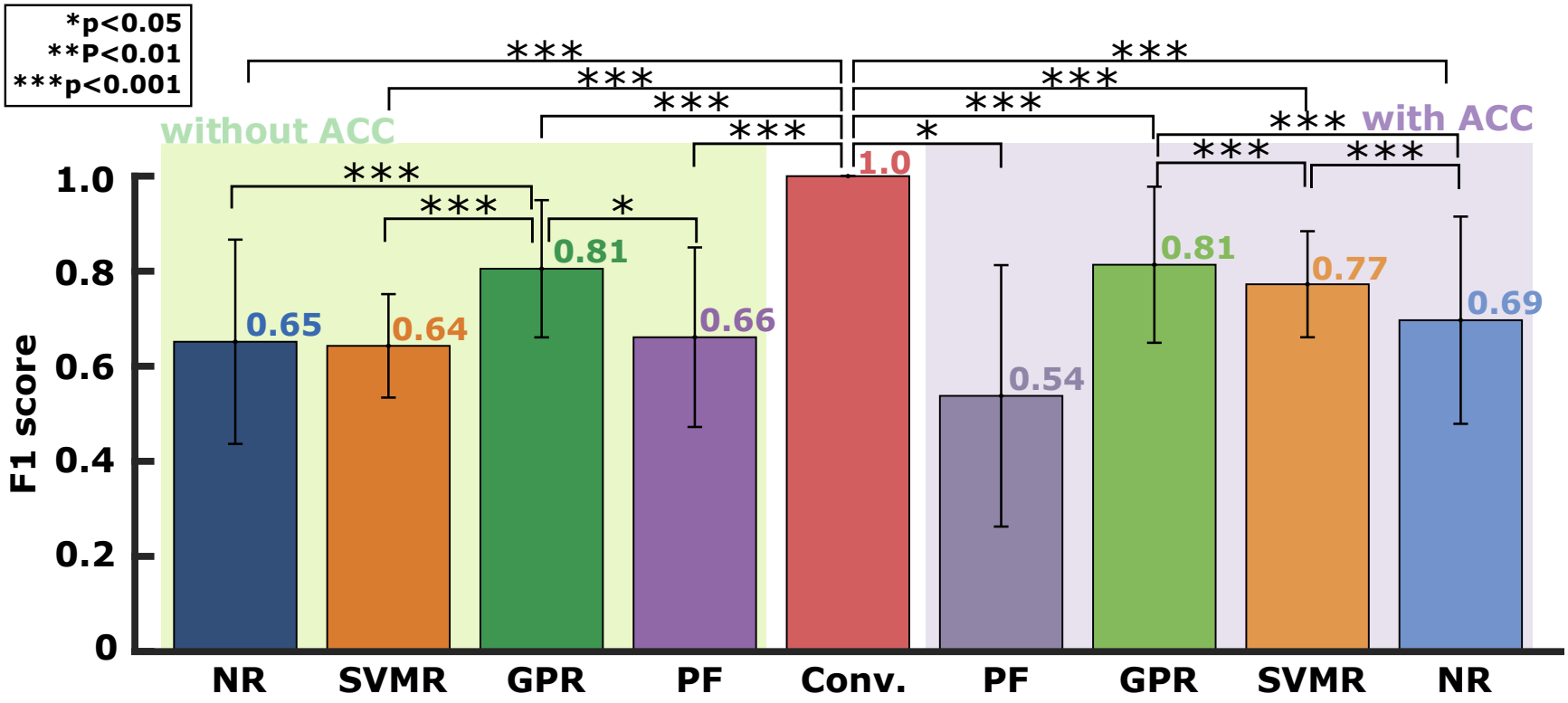

Figure 4.25: Performance of ISI-W estimation evaluated by F1 scores. Data is displayed in the same manner as in Fig. 4A. Measurements from the conventional incremental method were used as ground-truth data shown in the center.

	without ACC	with ACC
NR	99.33%	96.15%
SVMR	82.33%	94.09%
GPR	91.33%	94.84%
PF	100%	100%

Figure 4.26: Percentage of convergence.

4.4.3 Particle Filtering Result

The individualized ISI estimation technique was applied to the data collected from 11 subjects. The results are shown in Figure 4.27. The distribution of observed MEP responses is also shown in red as the ground truth. The centroid of the observed MEP is defined as a "sweet spot" or the optimal ISI to induce cortical facilitation.

An estimated range of effective intervals using the particle filter is shown based on a 3σ interval with respect to the posterior expectation. Each estimation run was iterated until the condition Eq. (4.6) was met; therefore, the numbers of iterations were different between subjects as well as that of individual estimation runs. Figure 4.29 shows representative converged particles, distribution, and ground-truth MEP responses. In the majority of the results shown in Figure 4.27, the estimated distribution of ISIs converged closely to the target MEP distribution at the end of the iteration although the convergence was not precise. It should be noted that the posterior expectation converges to the "sweet spot" at an earlier iteration. This would be advantageous for clinical application. Overall, the proposed algorithm successfully demonstrated its effectiveness.

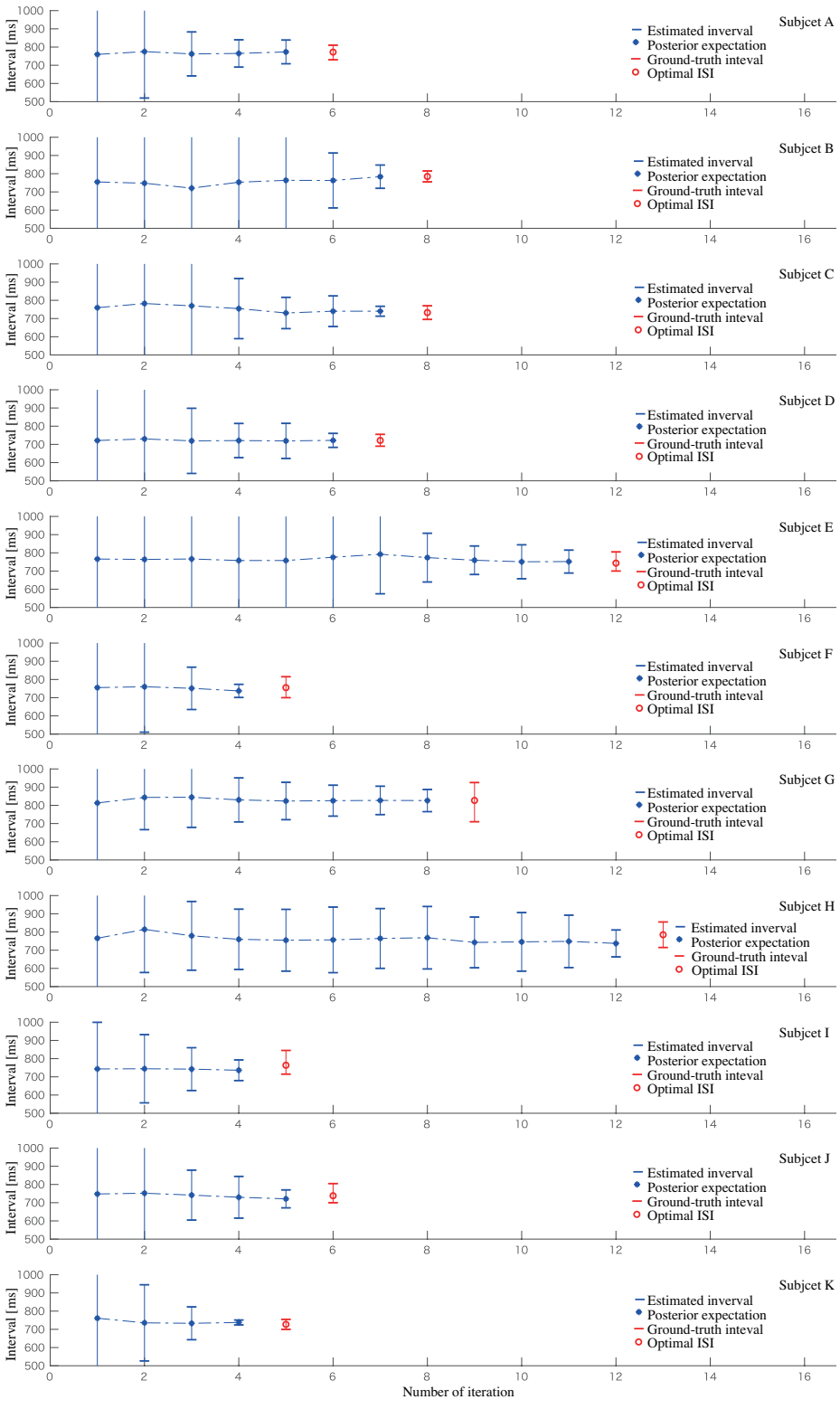

Figure 4.27: Progression of individualized ISI estimation with 30 particles ($M = 30$) (in blue). Range of MEP distribution and its centroid from incremental measurement as the ground truth are shown in red.

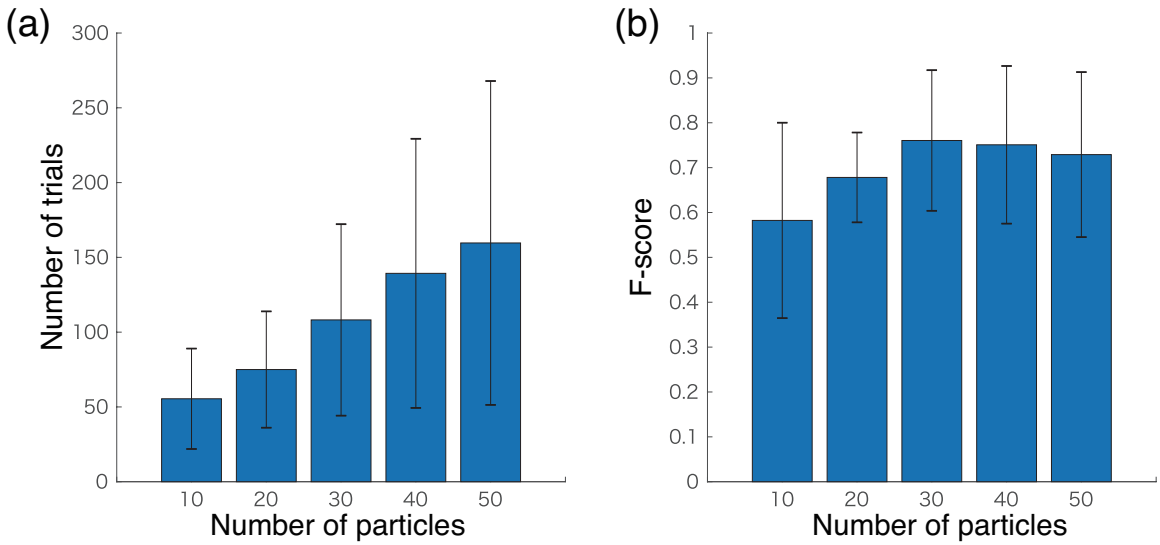

Figure 4.28: Comparison of the number of trials for 10, 20, 30, 40 and 50 initial particles for estimating individual inter-stimulus timings. (a) number of trials until convergence, (b) F-scores

4.4.4 Number of Particles and Performance

The total number of iterations was highly dependent on the number of particles M. In general, using a smaller number of particles reduced the number of trials per iteration, but would reduce estimation accuracy, requiring a greater number of iterations, and vice versa. To examine a possible trade-off between M and the resultant performance, five test cases with different M values, M=10, 20, 30, 40, and 50, were considered. Figure 4.28(a) shows the total number of trials for each number of particles. The number of trials until convergence was reduced as the number of particles decreased as expected. However, when M is small, some cases poorly converged due to insufficient observations. To address the trade-offs F-scores were computed for all the cases as shown in Figure 4.28(b).

Using the observed MEP amplitude values as the ground truth, true positive, true negative, and false negative were counted between two distributions as shown in Figure 4.29 for computing F-scores. While no statistical significance difference was observed between the F-scores, the mean F-scores for 10 and 20 particle cases were observed to be lower than other cases. For these cases, the distribution of the particles was not wide enough to

cover the distribution of MEPs after convergence, resulting in large estimation errors. As presented in Figure 4.28(b), using 30 or 40 particles was a reasonable choice which would require 3-4 iterations or a total of 100-150 trials from Figure 4.28(a). Compared to the conventional incremental method that required 500 trials, approximately 70%-80% reduction is expected by using the proposed algorithm.

4.4.5 Narrowing Search Space by using Accelerometer

The current implementation of particle filtering presented in the previous section assumes no prior knowledge on the location or shape of target MEP distribution. Particles were uniformly distributed (see Figure 4.27 at k=1) between t_{valve} (at t=0.5s) and t_{Valve} +0.5 (at t=1.0s). However, there should not be any long-latency responses between t_{valve} and t_{hit} as shown in Figure 4.6, thus this timing region can be excluded. An accelerometer attached to the medical hammer of the RNRS detects t_{hit} and contributes to narrowing the search space.

Figure 4.30 shows changes of the variance of particles (mean and standard deviation for five subjects) at each iteration with different numbers of particles from 10 to 50. When the accelerometer is used, the same number of particles are distributed between t_{hit} and t_{hit} +0.5. As can be observed in the figure, narrowing the search space improves the speed of convergence for all cases. In particular, the improvement is evident at the beginning of the estimation process. After k=5 or 6, differences become almost unnoticeable. Consequently, when faster ISI estimation is preferred for the mechanical PBS, detection of hammer impact time using an accelerometer is advantageous.

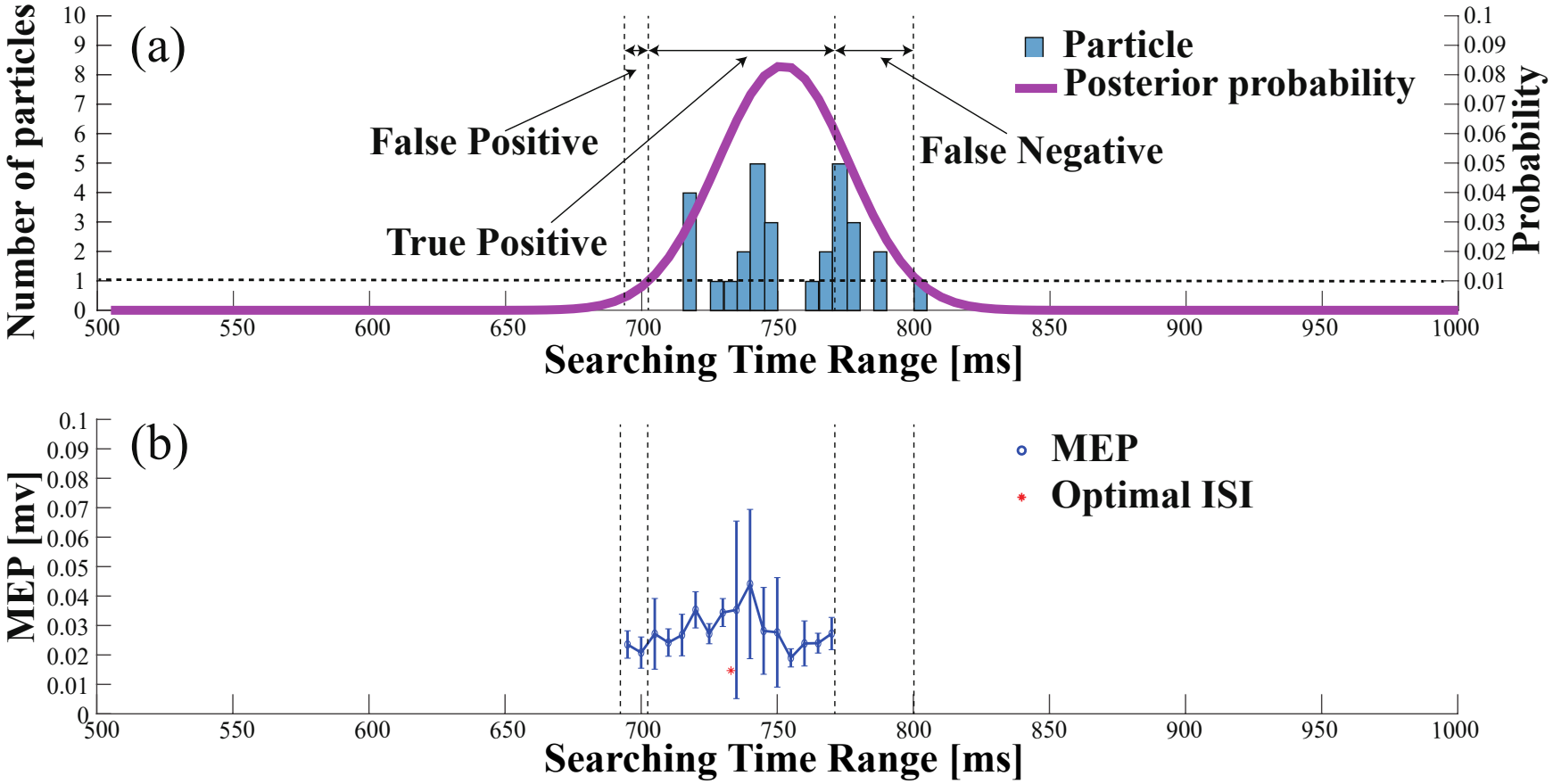

Figure 4.29: Representative final distribution of ISIs, (a) particles, and (b) magnitudes of motor evoked potential (subject 3).

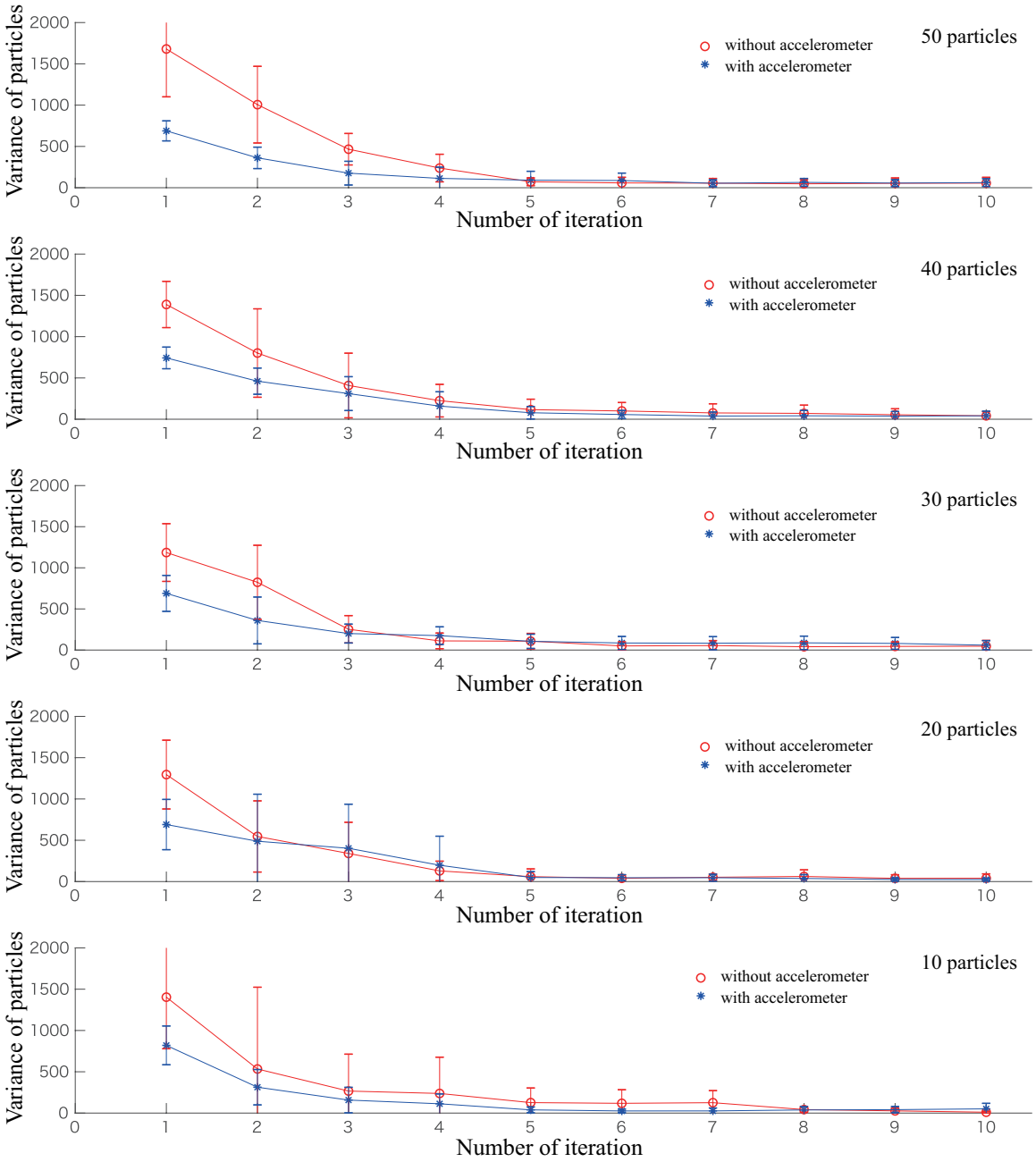

Figure 4.30: Convergence of particle filters with and without using the accelerometer readings: Variance of particles is displayed in each iteration. Results when the hammer travel delay was compensated by using the accelerometer are shown in blue. Results without using the accelerometer are shown in blue.

4.4.6 Further Improvement of ISI estimation

It is important to consider an initial distribution of particles for improvement in addition to the number of particles and the use of an accelerometer. In the current implementation, the particles were uniformly distributed by assuming no prior knowledge of PBS-induced MEP profiles. However, particles may be better distributed in a nonuniform fashion by utilizing largely collected data and establishing predictive individualization techniques. Generating prior probability distributions using prior knowledge would further improve the performance of ISI estimation.

4.4.7 Optimal Number of Initial Observations

NR, SVMR and GPR procedures require initial data points (initial observation of MEP) to begin regression that must be specified by the user. The choice of the initial number of observations, or n_{ini}, impacts the performance. The nominal searching period was given as [t_{valve} t_{valve}+500 ms]. For example, evenly distributed initial ISIs within the searching period of 500 ms would be 500ms, 650ms, 850ms, 1000ms when $n_{\text{ini}} = 4$. With the use of the accelerometer, the range can be reduced to [t_{hit} t_{valve}+500 ms], which may improve the performance.

Figure 4.31, 4.32 and 4.33 show comparisons of the F1 score and the number of total observations required to converge with n_{ini} from 2 to 9 with and without the accelerometer. In each graph, statistical significance was evaluated between neighboring bar plots within the same condition: without ACC and with ACC. For NR shown in Figure 4.31, the F1 score increased significantly from n_{ini}=7 to n_{ini}=8 without ACC and increased from n_{ini}=6 to n_{ini}=9 with ACC. The total number of observations was low for $n_{\text{ini}} < 7$ without ACC and $n_{\text{ini}} < 5$ with ACC. For SVMR shown in Figure 4.32, the F1 score took the highest value for n_{ini}=4 without ACC and for n_{ini}=3 with ACC. The total number of observations was low between n_{ini}=4 and n_{ini}=8 without ACC and low after $n_{\text{ini}} > 3$ with ACC. For GPR shown in Figure 4.33, the F1 score indicated the highest value for n_{ini}=6 without ACC and

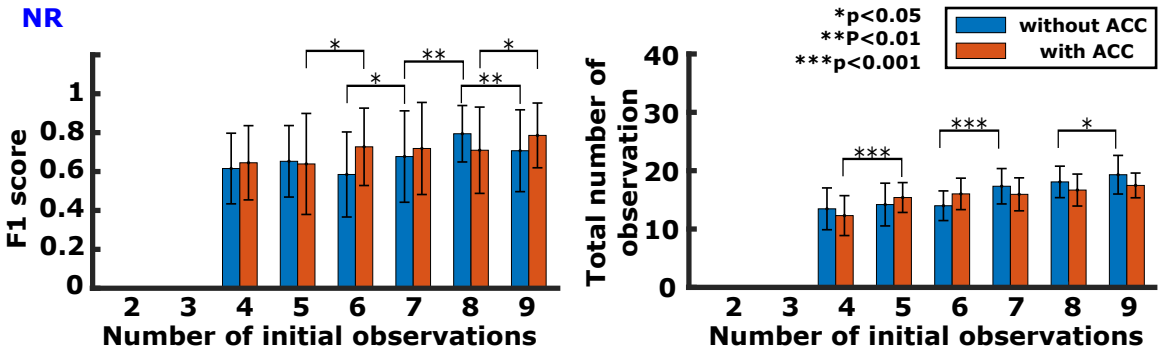

Figure 4.31: Comparison of regression performance with different numbers of initial observations. NR with F1 score (left) and Total Number of Observations (right). There is no data for n_{ini}=2 and 3 since initial data points are too few to run the algorithm.

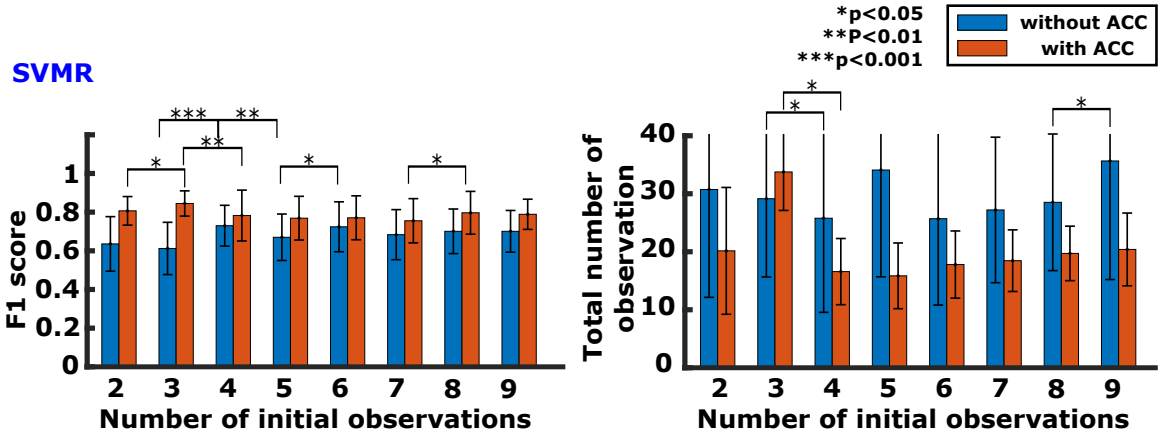

Figure 4.32: Comparison of regression performance with different numbers of initial observations. SVMR with F1 score (left) and Total Number of Observations (right).

$n_{\text{ini}} < 8$ with ACC. Total number of observations was low for $n_{\text{ini}} > 2$ with ACC and low for $n_{\text{ini}} < 8$ with ACC.

In practice, at least 1-2 non-zero enhanced MEP responses must be observed as initial data points for a regression algorithm to successfully progress. Given an average ISI-W of 108 ms in this dataset, $n_{\text{ini}} = 6$ or 7 would meet this requirement.

4.4.8 Gaussian Modeling of Mstim-induced MEP Enhancement

For Estim-induced neuromodulation in terms of conditioned stimulation, other groups reported correlations between ISI and MEP amplitudes [74, 22, 23, 24, 77]. Mathematical representation of MEP induced by peripheral or cortical stimulation has been reported in

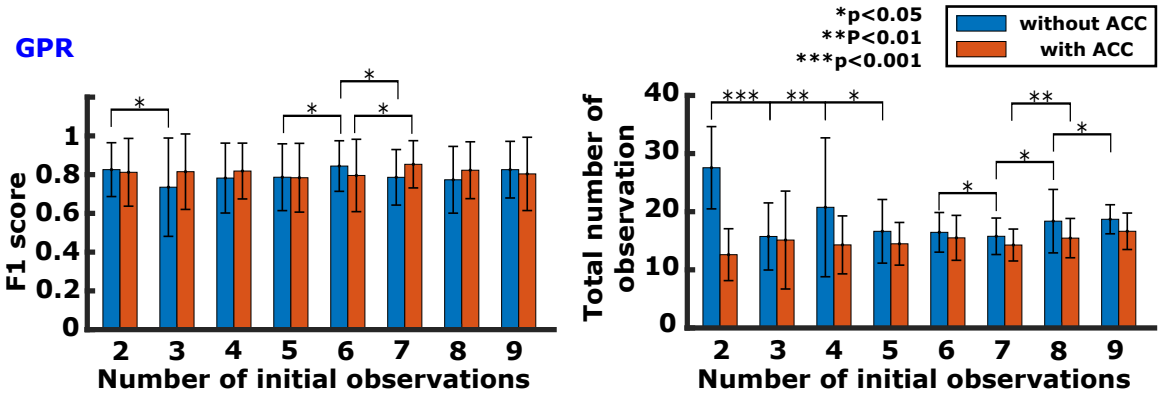

Figure 4.33: Comparison of regression performance with different numbers of initial observations. GPR with F1 score (left) and Total Number of Observations (right).

the literature. For example, a statistical model of MEP induced by electrical pulse trains to simulate the firing pattern of MEPs was proposed [91]. Another work developed a regression MEP model with different TMS intensities (i.e., input-output curve) [92, 93]. Gaussian modeling was adopted to fit the ISI-MEP relationship with a different number of Gaussian functions [94, 95, 96, 97, 98].

To the best of author's knowledge, there are even fewer works that studied ISI-MEP association with Mstim and its modeling by using an automated tendon-tapping robot. The majority of MEP profiles associated with ISI reported in the literature exhibited a single MEP distribution as well as the ones we collected along ISI as shown in Figure 4.22. While the objectives of Gaussian curve-fitting in the past studies are different from the objective of time-efficient ISI-W estimation in this chapter, the use of Gaussian models seems a reasonable choice. As far as Mstim with sub-threshold TMS for effective ISI-W estimation is concerned, a single-Gaussian model may be sufficient for parametric modeling of enhanced MEP profiles.

A Shapiro-Wilk test was applied to the current MEP data. This test verified the null hypothesis that the samples came from a normally distributed population. The mean MEP values at different ISIs were applied to this test to examine whether the MEP distribution is normal or not. Measured MEP distributions from eight subjects out of eleven did not reject the null hypothesis as shown in Figure 4.1. A two-Gaussian model was tested to see how

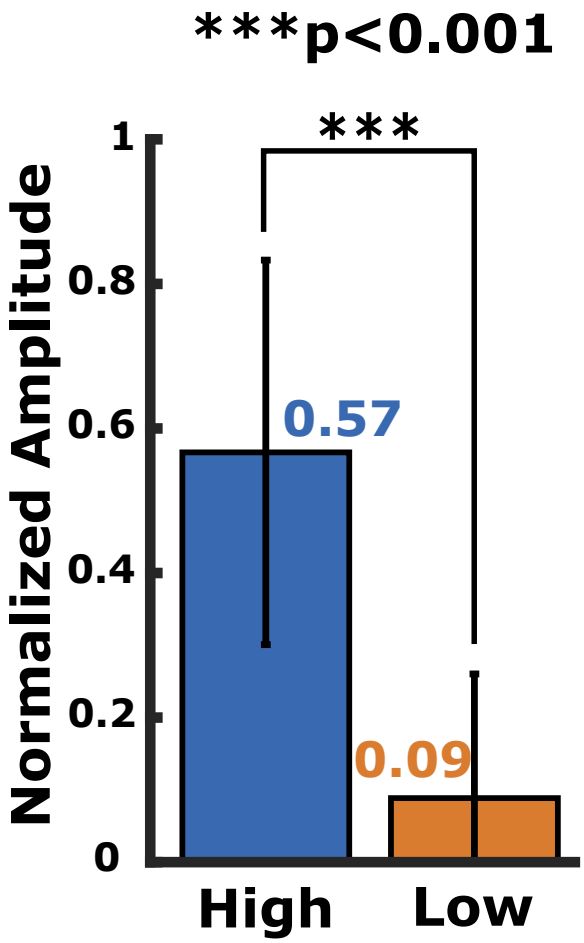

Figure 4.34: Modeling of enhanced MEP profile with two Gaussian functions by NR. The amplitude of the first Gaussian function converged significantly more than the amplitude of the second Gaussian; enhanced MEP profiles may be modeled by a single Gaussian function.

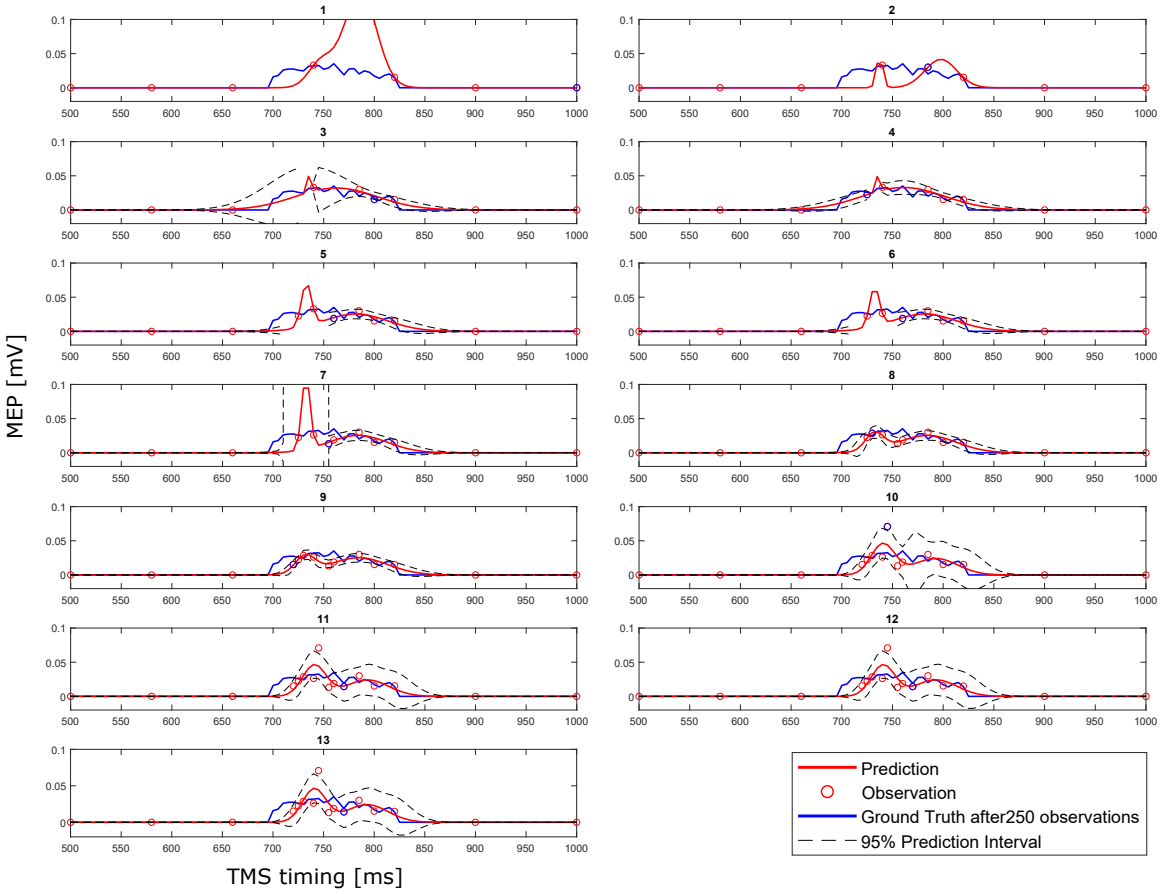

Figure 4.35: Example of NR regression with two-Gaussian model where converged two Gaussian distributions yielded comparable amplitudes. High: 0.046 mV and Low: 0.024 mV.

two Gaussian peak amplitudes are determined in NR for all subjects (n=11) for ten times each. In each trial, a greater amplitude was labeled as "High" and the smaller amplitude was labeled as "Low" as shown in Figure 4.34. Amplitudes were normalized for each subject for comparison across subjects. The amplitude of the Gaussian model with a higher amplitude was 6.3 times greater on average than the lower one. In addition, in 70% of the trials, the amplitude of the second Gaussian converged to zero, supporting the practical usefulness of single-Gaussian modeling even though it would reduce precision to some extent. Two-Gaussian model regression example for one subject when the both two Gaussian peaks have comparable amplitudes each other is shown in Figure 4.35. Predictions (i.e., Red solid line) clearly show two peaks in each iteration.

Given that typical MEP profiles may be oversimplified by a single Gaussian model with time delay, the speed of convergence and issues associated with over-fitting would improve, which is suitable for robust estimation of individual ISI-W by PF and NR as shown in Figure 4.26. On the other hand, as MEP profiles are variable, this work applied both SVMR and GPR as nonparametric methods for better precision.

4.5 Contribution of the Work

This chapter discussed Aim 2 of the research. In this work, a robotically enabled experimental procedure for the study of neuromodulation induced by peripheral mechanical stimulation has been developed. The size of ISI-W observed using enhanced MEP with Mstim by means of tendon tapping was found to be larger than that with sub-threshold Estim of the median nerve, possibly due to the different involvement of mechanoreceptors. This was because the response to mechanical stimulation is more dispersed in time due to the desynchronized activation of muscle spindles compared to impulsive nerve response induced by electrical stimulation [84]. A single-Gaussian model was applied to enhanced MEP profiles for parametric regression. The combination of the robotic tendon tapping and statistical regression reduced the number of observations to individually determine effective ISI to observe enhanced MEP up to 6.5 % (GPR with ACC), leading to a reduction of the physical burden on the subject who would otherwise receive many high intensity stimulation trials for more than two hours. Parametric models (NR and PF) that utilized a single-Gaussian model achieved high convergence. The high timing precision of the tendon tapping robot (STD $<$ 5 ms) enabled the developed procedure. This line of research is expected to produce a reliable tool which would clarify unique neuromodulations of the motor cortex with an application of robotic Mstim to muscles, in comparison to the conventional Estim of a peripheral nerve, and its paired central stimulation. The outcomes might allow for evidence-based implementation of mechanical stimulation paired with brain stimulation into individually tailored robotic rehabilitation for hemiparetic stroke survivors and possi-

bly other disabilities. Future work involves (1) the application of the developed robotic system to the investigation of both the enhancement and depression of MEP associated with Mstim-induced neuromodulation and (2) the evaluation of long-term neural plasticity with Mstim-TMS paired stimulation.

CHAPTER 5
AUTOMATED PAIRED BRAIN STIMULATION

5.1 Problem Statement

A common method to determine the occurrence of neuromodulation with Mstim is to record EMG signals on the targeted muscle and observe resultant motor evoked potential (MEP). This can then be compared to that of the baseline MEP from unpaired TMS to quantify the magnitude of neuromodulation. MEPs are observed approximately in 15 to 35 ms after application of TMS, depending on physiological parameters. For this neural facilitation paradigm to be most effective, TMS must be administered when the afferent sensory signals reach the corresponding region of the brain, allowing the signals to overlap [99]. When using mechanical tendon stimulation, this range was between 40-60 ms [7]. The inter-stimulus interval (ISI) is the key factor for this process to be repeatable. In the analysis of 97 different upper limb PAS experiments, the majority of them used an ISI of 25 ms for electrical median nerve stimulation [100]. This ISI appeared to have been selected based on an estimation of the overall latency taking 20 ms for the peripheral sensory input to reach the somatosensory cortex and additional 3 ms to reach the motor cortex [16]. Despite this, it was found that different ISIs could induce MEPs of different amplitudes in individuals [75]. Reasons for this variability include a diverse range of biological characteristics of those undergoing paired brain stimulation [16].

To efficiently induce neural facilitation and observe MEPs, a specific range of ISI should be identified and used for each individual. Finding effective ISI windows, however, is usually a time-consuming process with the conventional method as shown in Chapter 4.4.1 [87]. In order to reduce time to identify an effective ISI window for an individual, statistical estimation techniques were used in one study [87], resulting in a faster discovery

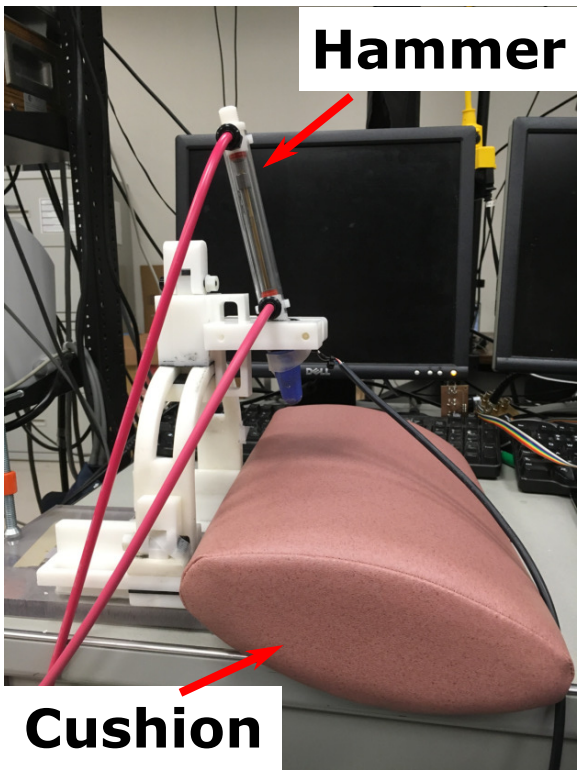

Figure 5.1: Experimental setup with cushion positioned under the tendon hammer.

of ISI validated by offline analysis. This approach can be further extended so that ISI-W can be adjusted automatically and online.

The objective of this chapter was to test effective statistical regression algorithm in the real experiment for individual ISI-W estimation. By feeding ISIs and corresponding MEPs into the statistical regression algorithm, the algorithm outputs an estimated ISI-W and determines the next ISI to continue the regression process. This iteration repeats until the stopping criteria meet and terminates the iteration procedure. In addition, MEP amplitude measurement system and impact timing detection system were tested to verify their performance.

5.2 Experimental Procedure and Methods

5.2.1 Impact Timing Precision Test Setup

In order to determine the accuracy of mechanical impact timing detection, a set of pre-determined ISIs was compared with the timestamps realized by the robot and detected by the developed algorithm. To simulate tendon tapping, a cushion was placed under the mechanical stimulator as a target object as shown in Figure 5.1. Five different ISIs were tested (10, 30, 50, 70, 90 ms) for 100 times each. Data was recorded, and the actual ISI was calculated by subtracting the accelerometer hitting time from the TMS triggering time. Note that TMS was not actually triggered, but instead, the timestamp of TMS triggering was taken for the purpose of ISI calculation. The difference between this realized ISI and the desired ISI was evaluated to quantify the error in each trial using Equations 5.1 and 5.2. The same process was repeated for four other sets of ISI that increased in smaller increments (51, 52, 53, 54 ms). A total of nine different ISIs (10, 30, 50, 70, 90, 51, 52, 53, 54 ms) were tested in this experiment.

$$ActualISI = T_{\text{TMS}} - T_{\text{hit}} \tag{5.1}$$

$$ISIError = ActualISI - TargetISI \tag{5.2}$$

To determine possible causes of variability in ISI production, timestamps were collected when the Mstim and TMS were triggered. Differences of these two were taken in each of the 100 trials for the 9 tested ISI sets. The standard deviation of the time difference of Mstim and TMS as well as the standard deviation of the ISI error were compared to examine if variability was due to mechanical properties of the Mstim robot or the accelerometer impact time detection method used in the algorithm. A Gaussian distribution was used to determine the probability that an ISI error was introduced within a particular time range

during a trial. The standard deviation for this model was determined by repeating identical 900 trials as mentioned above. To avoid differences between experimental groups, standard deviation was calculated after the respective average ISI error was subtracted from the error of every trial within a single ISI set. This process removed a trend from the data, making an average of cumulative data to be zero but still preserving its standard deviation. To determine the effectiveness of the MEP detection, previously recorded EMG data sets were entered into the MEP detection portion of the program to examine if it could properly localize and quantify resulting MEPs. These values were then compared with manually detected MEPs and then the percent differences were determined. Note that offline analysis was conducted without MEP observation as TMS was not applied to subjects during this investigation.

Figure 5.2 depicts an example of accelerometer and EMG measurement collected from one of experimental trials. At t_{start}, the trial began. At t_{valve}, the mechanical stimulator was triggered. At t_{hit}, the hammer made contact with the cushion (simulating the wrist tendon) where the accelerometer returned to the baseline value. A slight delay was introduced, followed by the triggering of the ISI. At t_{TMS}, TMS was triggered. A range from 15 to 35 ms after t_{TMS} was used when the algorithm searched for MEP. Finally, the trial finished at t_{end}. The entire system setup of this evaluation test is illustrated in Figure 5.3.

5.2.2 Impact Timing Detection

The hammer impact time, t_{hit}, was detected by the accelerometer attached to the hammer. The procedure started by setting a baseline level from the accelerometer reading. The first value of the accelerometer reading, which was the measurement when the hammer was still at the initial position, was used as the baseline level. This baseline was detected only once at the beginning of each trial. Once the baseline level was determined, the system kept reading accelerometer measurements until it detected the first falling edge that crossed the baseline level (i.e., the impact time) within a predefined hysteresis as shown in Figure 5.4.

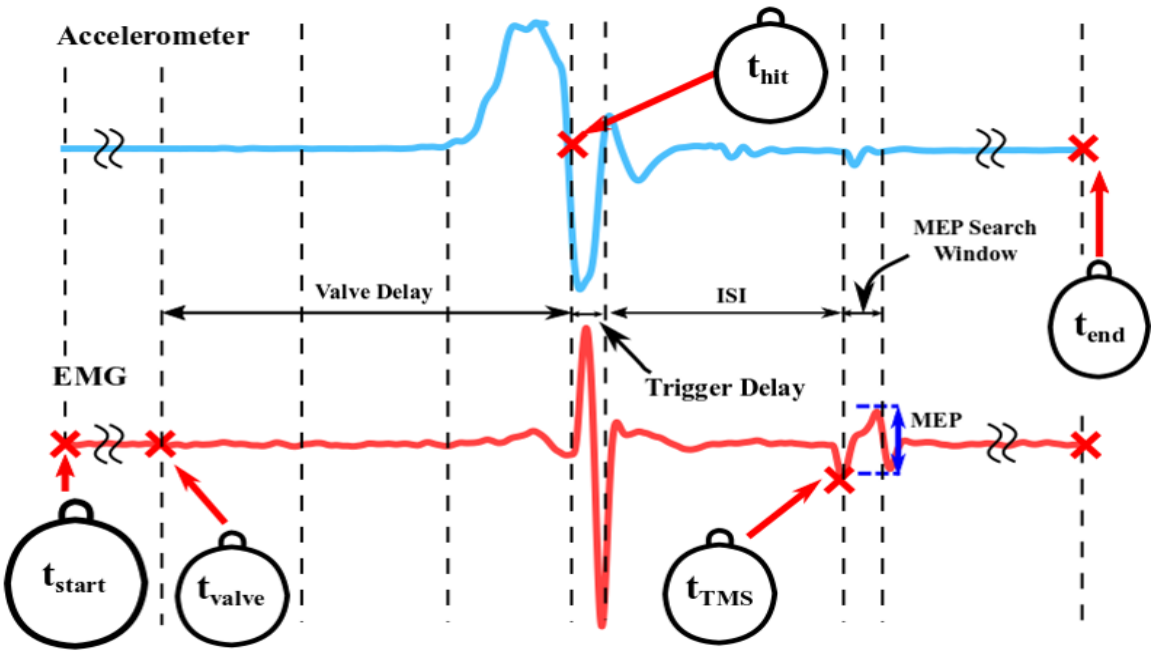

Figure 5.2: Example accelerometer and EMG data with key timestamps.

5.2.3 MEP Measurement

MEP measurement was conducted by executing a MEP detecting MATLAB code via LabView. As shown in Figure 5.5, when the two stimuli are overlapped over the motor cortex and induce neural facilitation, MEP facilitaiton should be observed within a 15 to 35 ms range (i.e., period of 20ms) after TMS triggering. The MEP detection code then extracted the initial time stamps, EMG data and t_{TMS} after the paired stimulation was given. Then, based on the t_{TMS} value, it determined the MEP search range as [t_{TMS}+15, t_{TMS}+35] ms. Within the search range, the program detected the maximum and the minimum values of the EMG reading and subtracted them to determine the peak-to-peak MEP amplitude as shown in Equation 5.3. A visual representation of this portion of the program is shown in Figure 5.6.

$$MEPamplitude = MaxEMG - MinEMG \tag{5.3}$$

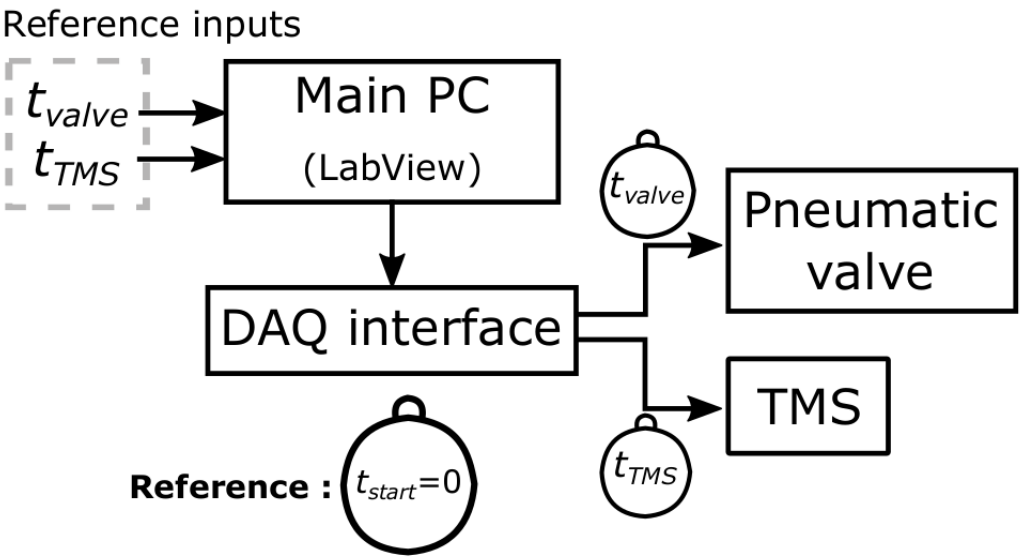

Figure 5.3: System configuration diagram. Main PC operates Mstim and TMS devices based on t_{valve} and t_{TMS} via a DAQ (Data Acquisition) interface.

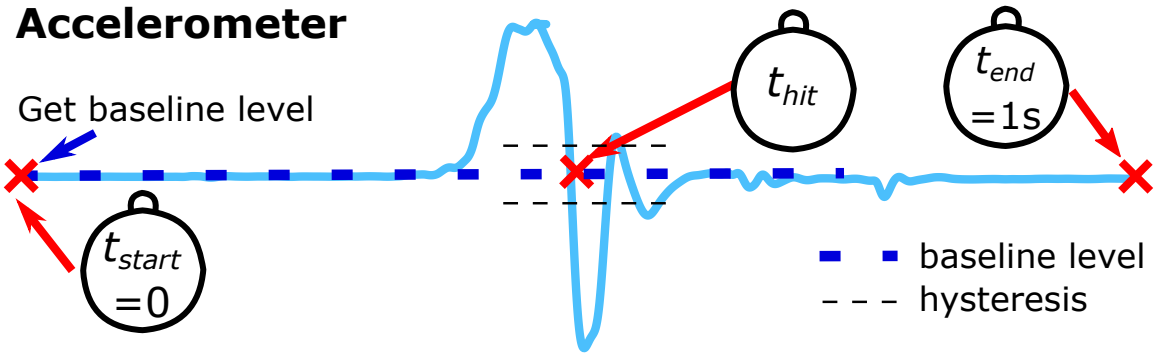

Figure 5.4: Hammer impact time detection.

5.2.4 Online ISI-W Estimation with Human Subjects

In order to verify the online ISI-W estimation using statistical method, real human experiments were conducted with two subjects. Among four statistical regression methods, nonlinear regression with Gaussian model was adopted which resulted in the lowest total number of observations before stop as shown in Chapter 4.4.2. Online ISI-W estimation algorithm and the *Signal Software* were used for this experiment. Triggers for mechanical stimulation and TMS were outputted from the *Signal Software* with a certain ISI between two. The measure MEP amplitudes and ISIs were fed into the algorithm which outputted

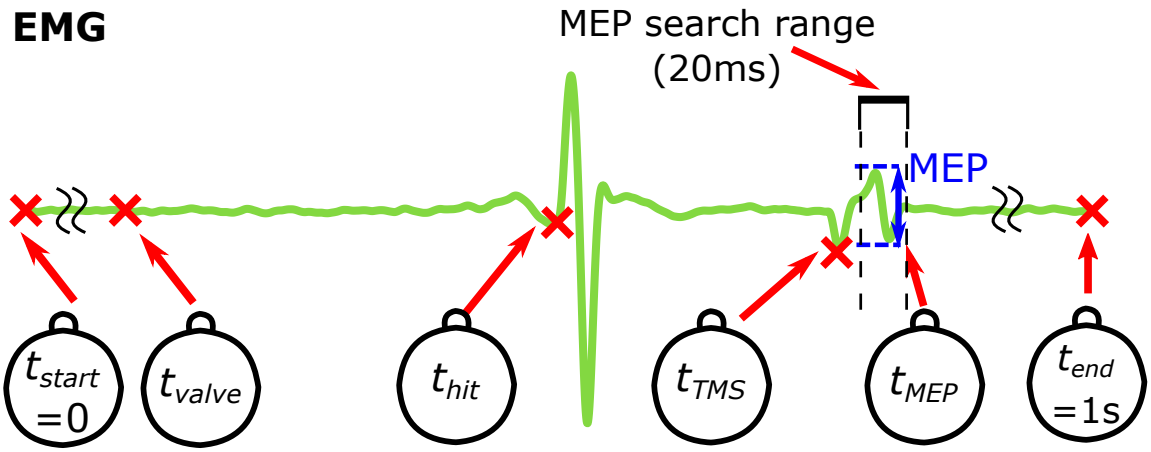

Figure 5.5: MEP search window.

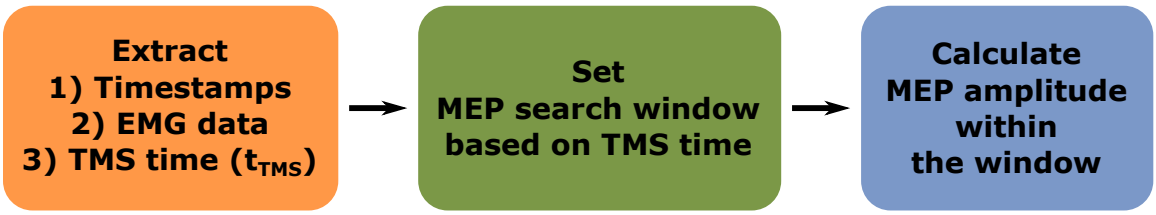

Figure 5.6: Flow chart of MEP detection program.

the ISI-W estimation and suggested next ISI to observe. In Figure. 5.7, describes the overall estimation procedure. This iteration repeated until the algorithm stopped based on the stopping criteria.

5.3 Results

5.3.1 Open Loop Tapping Precision Test

Figure 5.8 shows the average ISI error of the 100 trials for each of the 9 inputted ISIs. On the x-axis, each of the 9 inputted ISIs are shown and the average error is shown in the y-axis. The error bars indicate the respective standard deviation of each group. The ISI error is found using Equation 5.1 and Equation 5.2. The highest average ISI error found was 1.5 ms. Some of the ISI errors returned were negative, meaning that the ISI was initiated before t_{hit} occurred. Any negative actual ISI was removed from the data set and were considered mistrials during the experiment. This occurred in 8 trials, or 0.89% of the trials, all of

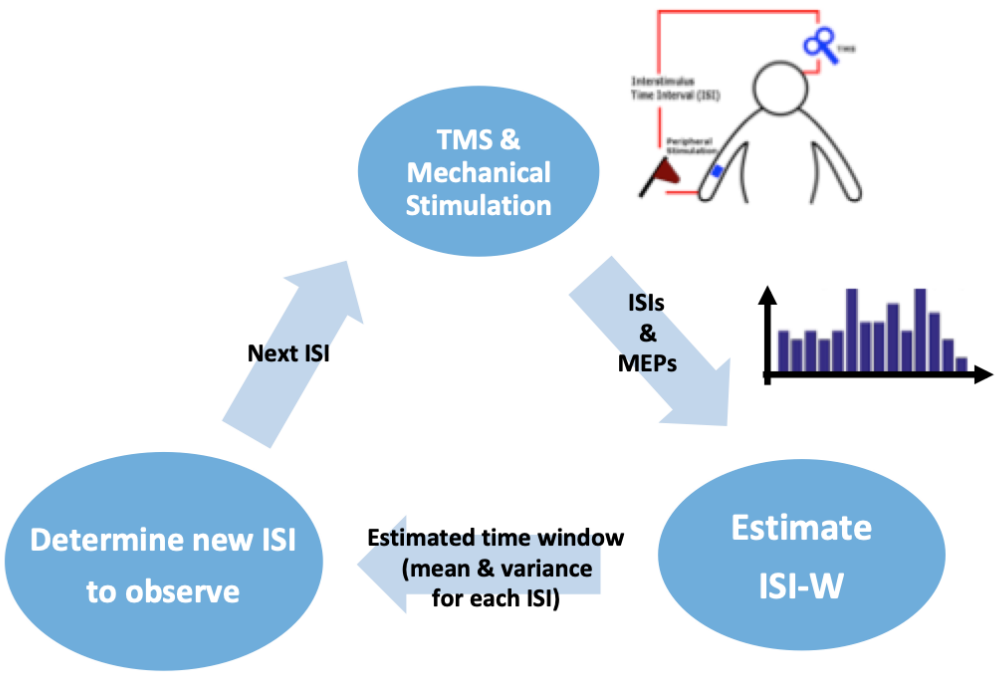

Figure 5.7: Online ISI-W estimation diagram.

which were in the first experimental group (ISI = 0.01).

Figure 5.9 shows the standard deviations of the differences between the TMS trigger time and the Mstim trigger time. The x-axis is divided in the same manner as Figure 5 with one group for each of the 9 inputted ISIs. The y-axis shows the standard deviation in ms. All groups had at least 1 ms of standard deviation with the highest being the 52 ms ISI group with a standard deviation of 7.46 ms.

Cumulatively, using the 900 trials, the standard deviation of the ISI error was calculated to be 1.93 ms. Using a Gaussian normal distribution, the probability at which the error would fall between a set range is shown in Table 5.1. As the distribution dictates, the probability of occurrence will decrease as the magnitude of the error increases.

Table 5.2 shows the offline MEP analysis using 12 previously recorded paired brain stimulation data. These trials were conducted with the same ISI. The resulting values were detected by the designed program. Percent difference from the manual calculation was also found for each trial shown in the third column of the table. In 8 of the 12 trials, the

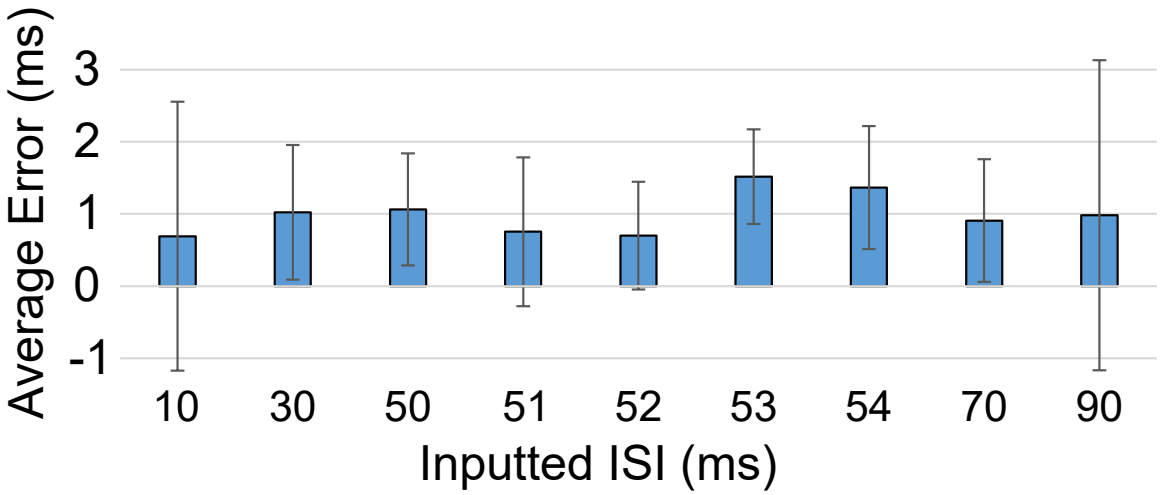

Figure 5.8: Statistical analysis of the trials for the 9 different inputted ISIs.

Table 5.1: Probability of an ISI error occurring with a specified magnitude

Magnitude of ISI Error (ms)	Probability of Occurrence
0 <E <1	39.62%
1 <E <2	30.44%
2 <E <3	17.98%
3 <E <4	8.16%
4 <E <5	2.84%
E >4	3.78%

manually detected MEP was the same as the value detected by the program. In 11 of the 12 trials, the percent difference was below 1%.

5.3.2 Online ISI-W Estimation Test

ISI-W estimation was done online with two subjects. For this test, the nonlinear regression estimation method among four methods was used for ISI-W estimation and the next ISI suggestion. Seven initial ISIs were determined by evenly distributing the ISIs between the t_{hit} and the end of the search window which is 1 s. Paired stimulation, estimated ISI-W and next ISI suggestion were in one iteration and this iteration was repeated until the algorithm stopped the procedure when the stopping criteria met the condition. Two online ISI-W

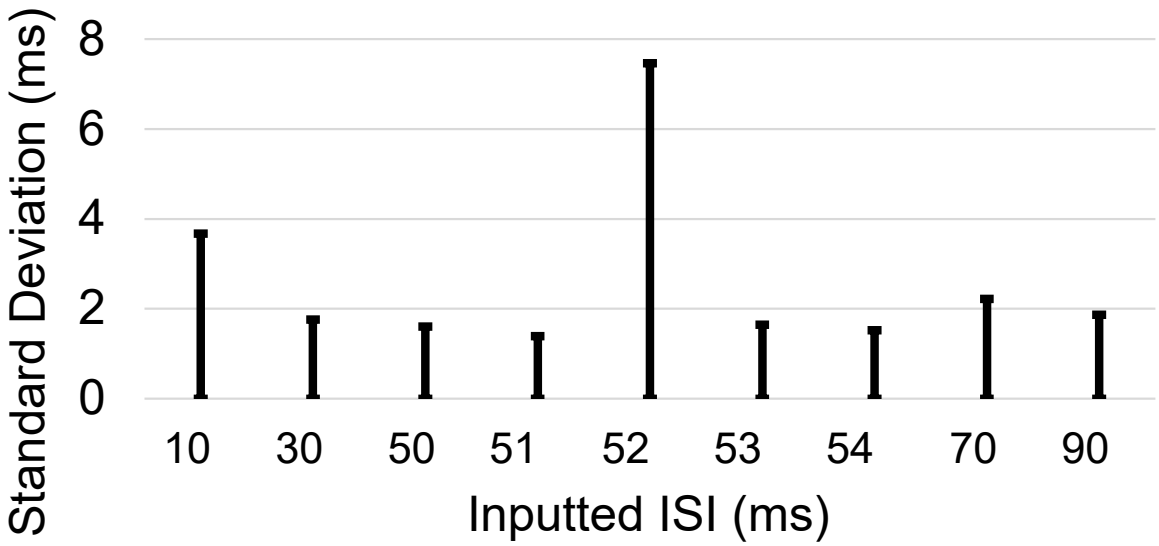

Figure 5.9: Standard deviations of the difference between the time of the TMS trigger and the time of the mechanical stimulation trigger

estimation results are shown in Figure 5.10 and Figure 5.11. The ISI-W profiles from the conventional incremental method were compared with the estimated ISI-W profiles as shown in Figure 5.12 and Figure 5.13. The numbers shown in the figures are correlation coefficients between two graphs. The correlation coefficients were about 0.83 and 0.85 and the total number of observations were 23 and 15 respectively. In Table 5.3, the estimated ISI-W and measured ISI-W results for both subjects are compared.

5.4 Discussion

5.4.1 Online ISI-W estimation

In order to converge this estimation, there are a few conditions to meet. First of all, the number of initial observations should be evenly distributed within the search range (i.e., possible ISI-W location which is 500ms long) to capture the profile of the ISI-W distribution. Considering the large variability of the ISI-W width which is varied from 40ms to 220ms and the t_{hit} timing, seven initial observations were appropriate for this online estimation to have 30-40ms intervals between the initial observations. Second, measuring MEP amplitudes at the two ends of the search range were helpful to converge the estimation.

Table 5.2: Offline detection of the MEP by the designed program

Trial	Program-Detected MEP Value (volts)	Percent Difference from Manual Detection
1	0.034146	0.135%
2	0.078486	4.054%
3	0.071351	0%
4	0.05759	0%
5	0.033635	0%
6	0.052494	0.983%
7	0.044339	0%
8	0.036185	0%
9	0.053003	0%
10	0.088678	0%
11	0.088167	0%
12	0.081544	0.001%

Table 5.3: Estimated ISI-W and measured ISI-W comparison

	Subject1		Subject2	
	estimated ISI-W	measured ISI-W	estimated ISI-W	measured ISI-W
Correlation	0.83		0.85	
Number of total stimulations	23	264	15	408

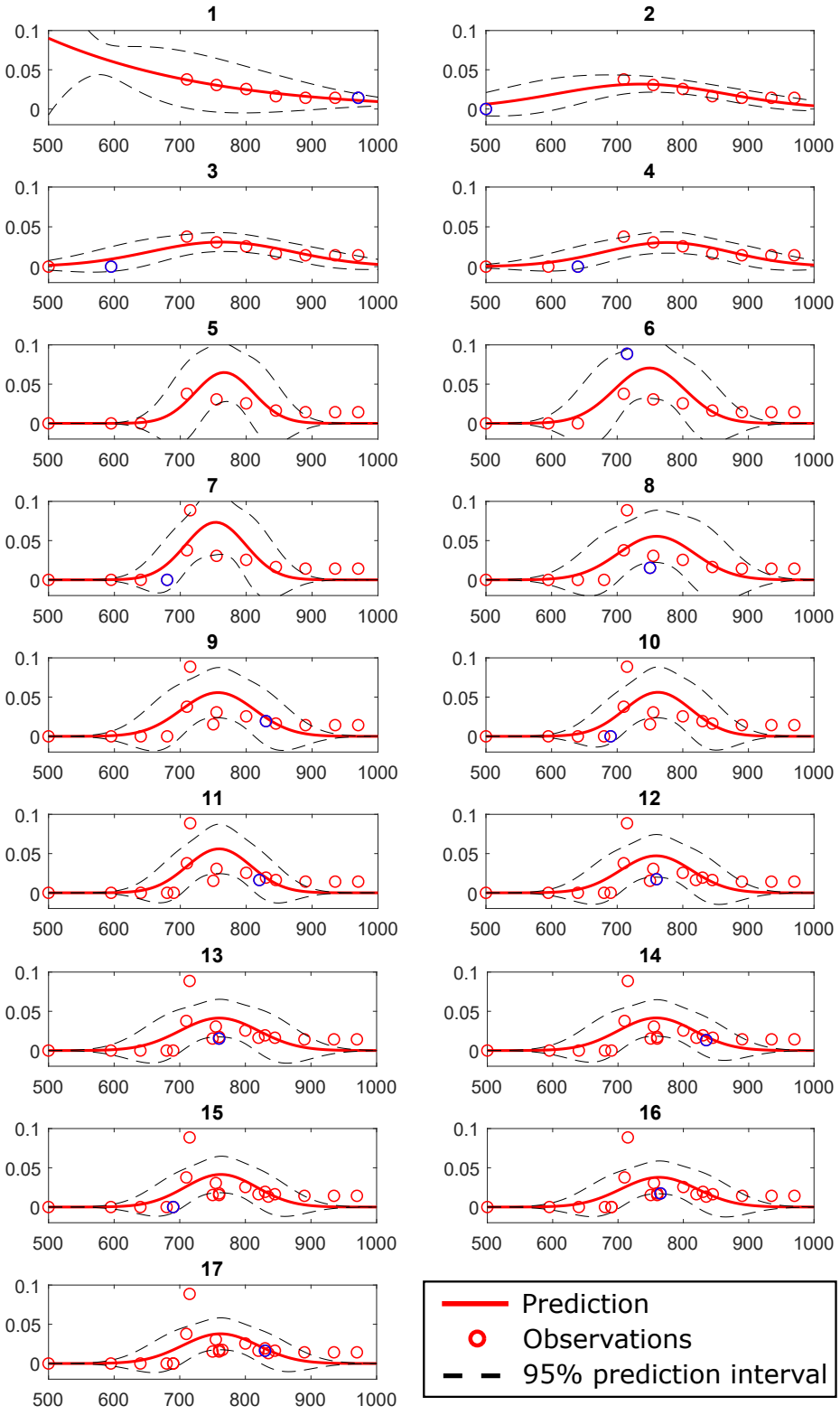

Figure 5.10: Online ISI-W estimation iterations example of Subject 1. Nonlinear regression was used for the estimation and seven initial observations were used.

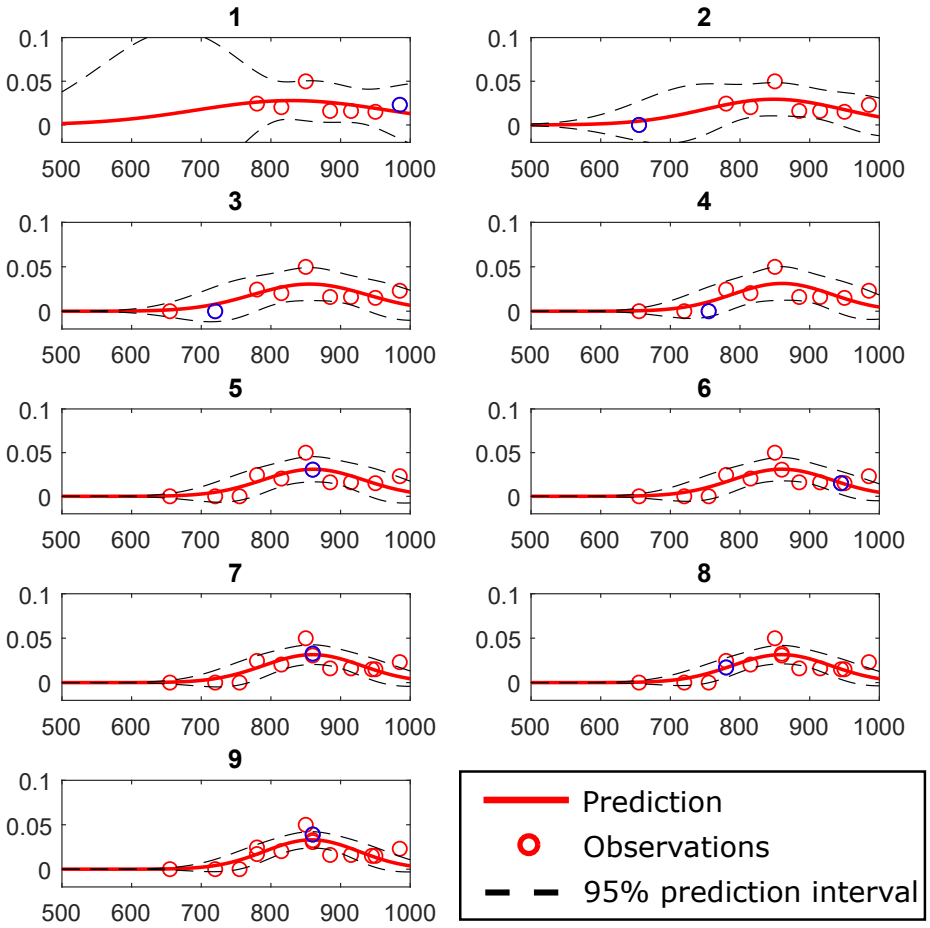

Figure 5.11: Online ISI-W estimation iterations example of Subject 2. Nonlinear regression was used for the estimation and seven initial observations were used.

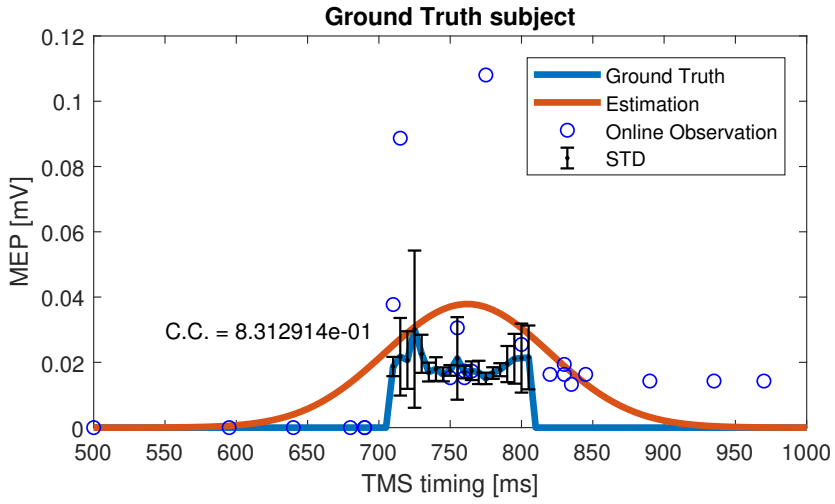

Figure 5.12: Ground truth (Measured ISI-W) and estimated ISI-W comparison of Subject 1. C.C. represents a correlation coefficient.

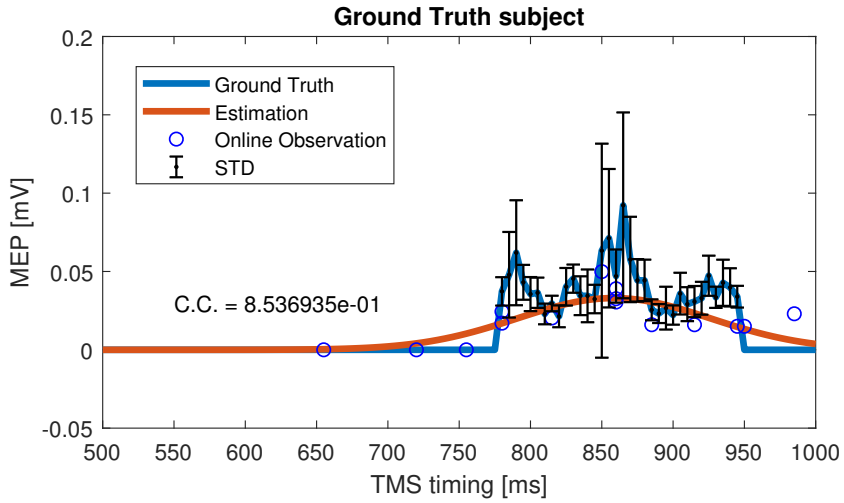

Figure 5.13: Ground truth (Measured ISI-W) and estimated ISI-W comparison of Subject 2. C.C. represents a correlation coefficient.

Since we assumed a single distribution of ISI-W profiles with subthreshold TMS stimulation, the two search range ends which were located outside of the ISI-W profile would have small and negligible MEP amplitudes. Defining these two possible two ends of the Gaussian estimation of ISI-W profile helps the estimation to converge quickly.

Human neuromodulation responses are not deterministic but probabilistic to external stimuli in nature. For this reason, with a subject with a high variability in responses, it was difficult to estimate the effective ISI-W since the estimated distribution won't converge. In addition, the estimated ISI-W was not well matched with the ground truth (measured) ISI-W. Each paired stimulus applied during the ISI-W impacted the overall neural excitability and it eventually kept changing the MEP measured ISI-W every time the stimuli were applied. However, with a subject with responses which are still probabilistic but overall responses are consistent with small variability, the estimation converged and outputted a final estimated ISI-W.

5.4.2 Convergence Conditions

In order to make this nonlinear regression to converge quickly, there are a few things to consider. First of all, since this NR is an iterative search algorithm that finds the best graph

that follows the observations, it is better to narrow the search range as possible. For this particular experiment, the range could be narrowed by using the t_{hit} timing measured by the accelerometer. Second, the starting value of the parameters should be closer to the expected final values. In other words, the parameters of the Gaussian model that was utilized for NR should be chosen so that the mean, variance and the amplitude of the Gaussian is close to the final value. Therefore, the initial parameters were chosen so that the mean of the Gaussian model was located in the middle of search range, and the variance and the amplitude were chosen based on the prior knowledge of the ISI-W.

5.5 Contribution of the Work

This chapter discussed Aim 3 of the research. In this study, the system performances of each portion of the system had been investigated. In addition, the online ISI-W estimation was tested with two subjects. The correlation coefficient between the estimated ISI-W and the measured ISI-W was 0.84 in average. Online estimation required the number of observations which were 8.7% and 3.7% of the number required in the conventional incremental methods for each individual.

CHAPTER 6
VARIABILITY IN MANUAL TIME INTERVAL PRODUCTION

6.1 Problem Statement

Similar to the PAS intervention discussed before, the interstimulus interval (ISI) between the two stimuli, mechanical stimulation and the patient's intention to move, is considered to be crucial for motor functionality recovery in RFE. However, in the current RFE procedure, there is no described protocol for determining or adjusting the ISIs for individual patients. In other words, there is no systematic way for physical therapists to adjust the ISI beyond each physical therapist's experience. Because the ISI that is expected to enhance corticospinal excitability is significantly less than one second, it would be difficult for non-skilled therapists to provide a consistent ISI over trials. It is anticipated that skilled therapists are able to adjust the timing between the peripheral stimulation and the verbal cue to instruct the patient to move (i.e., intention to move) relying on their experience treating many other patients. In the development of future robot mediated therapies, it is important to quantify how much timing variability may be introduced to ISI when timing-critical therapies such as RFE is performed manually. This issue has not yet fully addressed.

The work presented in this chapter focused on the investigation of the variability in manual time interval production by human subjects. A time interval production test was conducted to quantify human performance in adjusting time interval production. Previous time interval production tests in the literature [101] merely instructed subjects to produce a fixed target time interval by providing simple auditory feedback informing the time that should be produced by the subjects. In this study, the time interval production test was extended to four different forms of visual feedback, including a bar graph, on/off light indicator, numerical display of time intervals produced and absolute errors.

6.2 Methods

6.2.1 Subjects

Four healthy volunteers at Georgia Institute of Technology participated in this experiment. This experiment didn't require IRB review because it did not meet the definition of research with "human subjects" as set forth in Georgia Tech policies and procedures and federal guidelines.

6.2.2 Experimental Method

National Instruments LabVIEW was used to develop a graphical user interface (GUI) for this experiment shown in Figure **??**. Subjects sat down in front of a monitor and used two buttons on a keyboard as a 'start' button and an 'end' button to create a time interval as shown in Figure 6.2. Visual feedback was provided through the GUI to the subjects. Subjects were asked to adjust time interval to reproduce a target time interval, not disclosed to the subjects, based on one type of visual feedback out of four. The experimental scene is shown in Figure 6.3. Subjects continued feedback modes until it reached 200 trials.

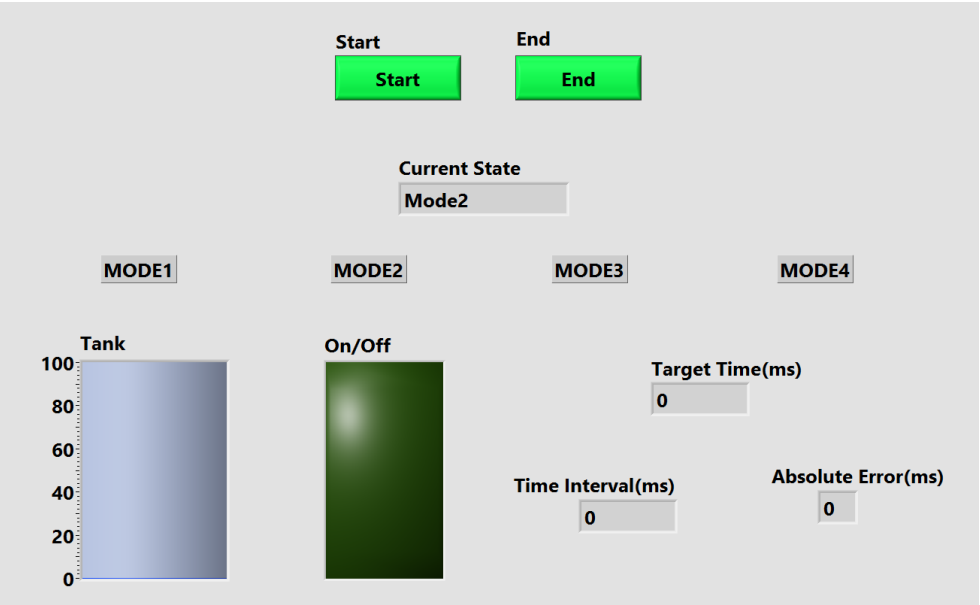

Figure 6.1: LabVIEW graphical user interface.

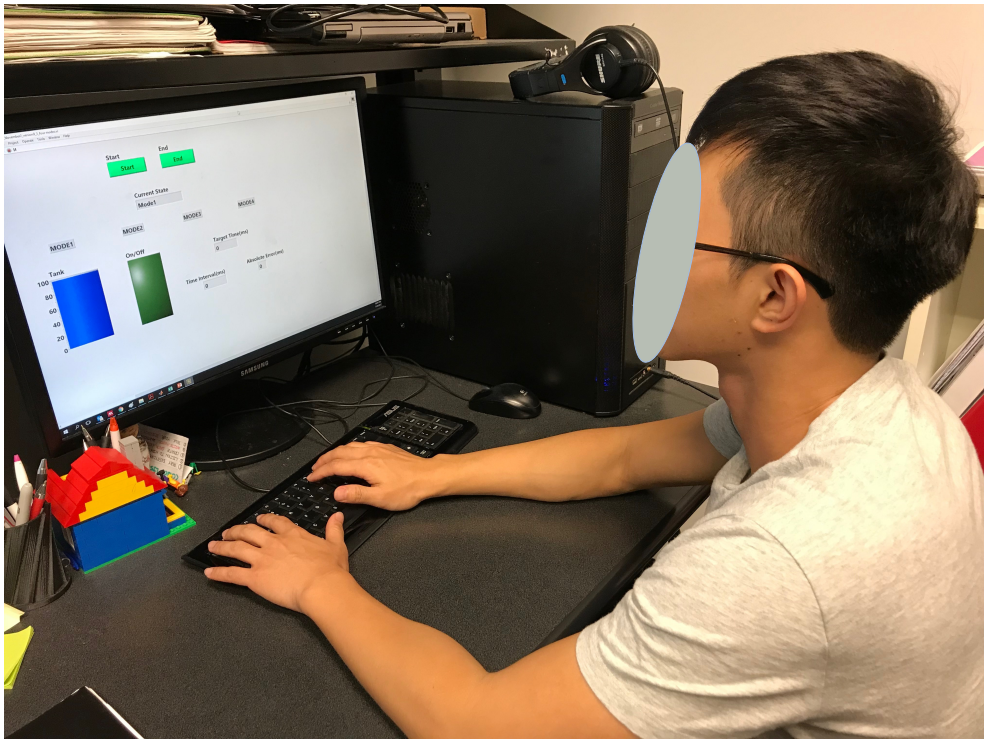

Figure 6.2: Experimental setup.

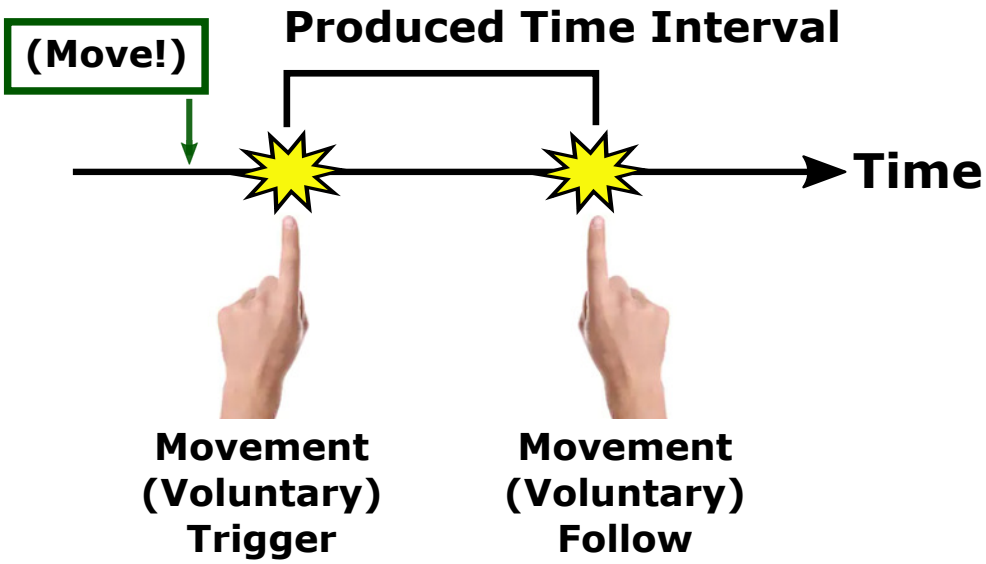

Figure 6.3: Manual time interval production

6.2.3 Procedure

Each subject completed three experimental sessions. The first and second sessions consisted of four feedback modes with two hundred trials each. Each of four different types of visual feedback was used in each session. Table 6.1 summarizes all the feedback modes used in the experiments. In Mode 1 and 2, subjects were instructed to produce a predefined target time interval without any information of the target explicitly given. In Mode 1, a tank bar gave a score to the subjects immediately following each trial using the Gaussian model shown in Equation (6.1). In Mode 2, a light indicator turned on immediately following each trial with a probability corresponding to the score, providing binary (i.e., on/off) visual feedback. These two feedback modes are illustrated in Figure 6.4. For example, when a subject produces a 294 ms time interval, a corresponding score of 70 is calculated by the Gaussian model. This value is then indicated in a tank bar for Mode 1. This value is used as a probability to determine whether the indicator illuminates or not in Mode 2.

$$Score = Ae^{-(\frac{t-M}{V})^2}$$

$$\text{A: Scaling Factor (between 1 to 100)}$$

$$\text{M: Peak Location Time} \qquad (6.1)$$

$$\text{V: Variance}$$

In Modes 3 and 4, the target time interval was explicitly informed to the subjects. The time interval that the subject created in each trial was numerically displayed on a monitor in Mode 3 and the absolute error between the target time interval and that the subjects created was given as feedback in Mode 4.

A target time interval of (or the peak time at) 300ms, variance of 100ms, and scaling factor of 100, were used for the Gaussian model shown in Equation (6.1) for the first session. A target time interval of 500ms, variance of 100ms, and scaling factor of 100, were used in the second session. Mode 2 was designed to partially reproduce a possible situation

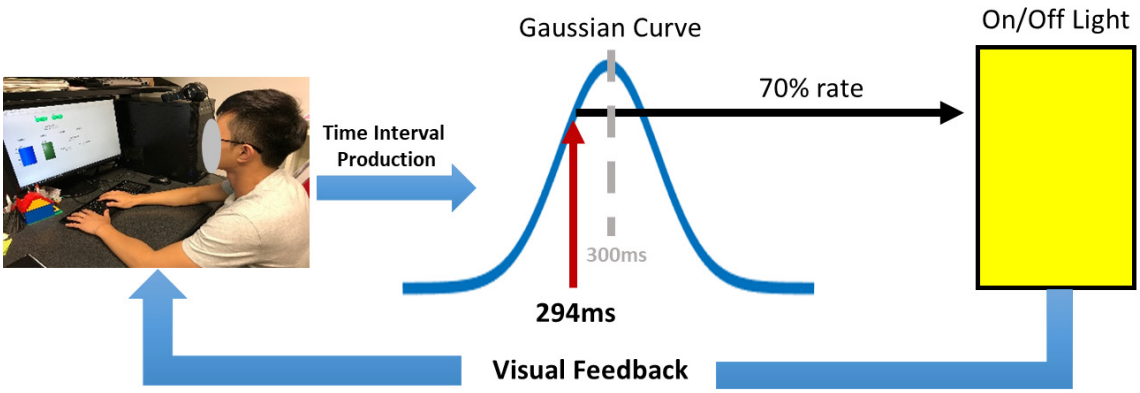

Figure 6.4: Descriptions of Mode 1 and Mode 2. Mode 1 provides an analog visual score using a tank bar. Mode 2 provides a binary score using an on/off light indicator. Both the analog score and the light on/off probability are determined by the Gaussian model.

Table 6.1: Mode description.

	Mode Description
Mode 1	Visual score bar using Gaussian model
Mode 2	LED on/off using Gaussian model (mimic RFE)
Mode 3	Target Time & Time interval produced
Mode 4	Target Time & Absolute error

in the RFE procedure. When two stimuli are paired over the motor cortex in an appropriate timing, the long latency response, which indicates neural facilitation, should be observed in electromyography and resultant muscle twitch. In contrast, no muscle twitch should be observed when neural facilitation did not occur. Note that, in mPBS, it is unlikely to observe a long latency response in every trial even though paired stimuli are applied with an inter-stimulus interval as shown in Figure 6.5 primarily due to subject variability. This figure shows two sets of data that counted the number of long latency responses observed when two stimuli are paired in different time intervals [80][102]. This binary information (i.e., existence or non-existence of the long latency response and associated muscle twitch) according to a certain probability was represented by indicator on/off feedback. In order to address the challenge in the Mstim-initiated long latency response, the third session was

designed. The third session consisted of Mode 1 and Mode 2 of two hundred series of trials. This session was the same as the first session except for the scaling factor was changed to 50 in order to simulate the low occurrence rate of the long latency response. A two-minute break was given between modes and between sessions. The experiment took approximately 60 min in total.

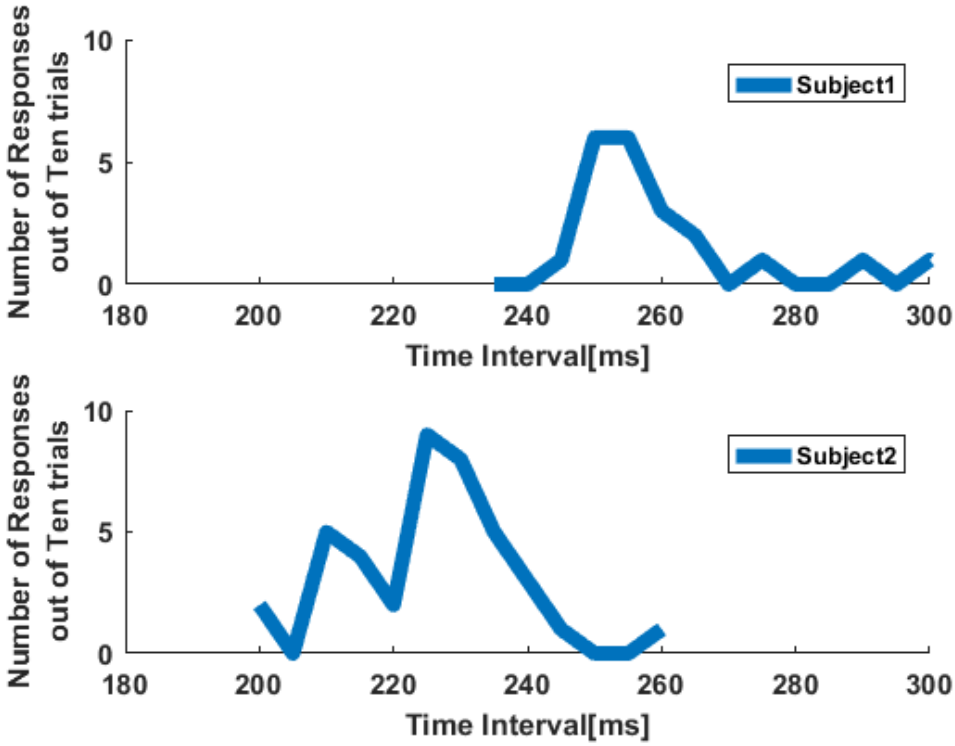

Figure 6.5: Frequency of observation of long latency responses due to Mstim paired with subthreshold TMS (n=2). Graphs show numbers of observed MEP out of ten trials versus each tested ISI. This procedure was repeated with different time intervals. The probability to observe MEP is still less than 1 even at the ISI that provides the maximum number of responses.

6.3 Results

6.3.1 Repeatability of Manual Time Interval Production

Figure 6.6 shows the error between target time interval, mean interval produced, and standard deviation for each feedback mode. Regardless of the feedback mode used, the standard

Table 6.2: Mean and standard deviation of each mode for each session. Four subjects' data were used.

	Session1				Session2			
	Mode1	Mode2	Mode3	Mode4	Mode1	Mode2	Mode3	Mode4
Mean[ms]	294	311	300	282	499	500	496	474
Standard Deviation[ms]	68	64	36	50	93	93	58	59

deviations of the time interval produced increased as the target time interval increased from 300 ms to 500 ms. This trend followed the result from Wearden et al. [101] where the mean time interval produced was a function of target time interval and the standard deviation varied with the mean. The standard deviation of Mode 3, which explicitly informed the time interval that subjects produced, had the lowest value at 36 ms and 58 ms for target times of 300ms and 500ms, respectively. This may be because that Mode 3 displayed the time interval subjects created explicitly, providing the most direct feedback information among the four modes. Even though Modes 1 and 4 used some form of the absolute error as feedback, Mode 1's standard deviations (18 ms and 33 ms, respectively) were greater than that of Mode 4 for target times of 300ms and 500ms. In addition, the error was greater in Mode 4 compared with that of Mode 1. This implies that Mode 1's visual feedback was more informative for interval time determination (i.e., low error), but not for interval production (high standard deviation).

The previous chapter showed that the average range of time intervals that increased corticospinal excitability was approximately 40 ms and the profile of observed MEP could be represented by a Gaussian distribution [102]. In other words, changes in the excitability would occur when ISI is somewhere close the peak of the Gaussian distribution within about $\pm$ 20 ms tolerance (i.e., 40ms length). As shown in Table 6.2, standard deviations for each mode are greater than 20ms which means the percentage of time intervals within $\pm$ 20ms to the target time is less than 68.2%. This may be directly comparable to the precision of the robotic tapping device which can precisely produce time interval within

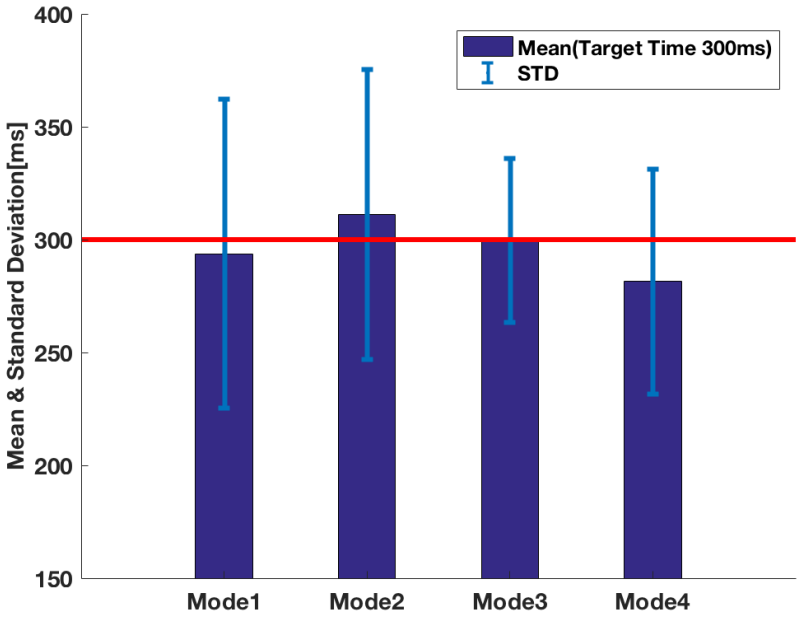

(a) Target Time : 300ms

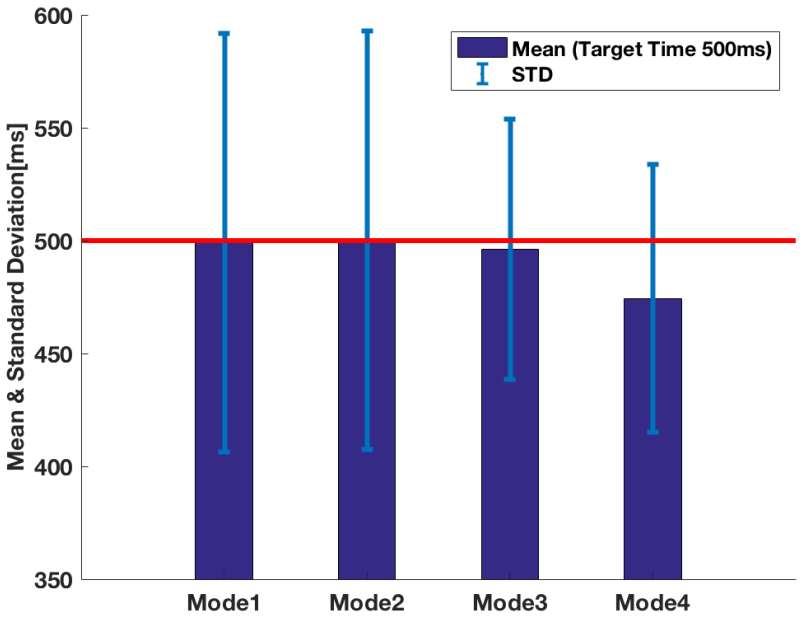

(b) Target Time : 500ms

Figure 6.6: Error between the target time and the mean interval produced and standard deviation against types of feedback. Four subjects' data were used.

a standard deviation of 5 ms [7]. The high precision achieved by the robotic device can virtually realize any ISI within an effective ISI window, which is a significant advantage over human manual timing production.

6.3.2 Mock RFE

In the real RFE procedure, the long latency response which is basically on/off doesn't occur 100% even at the optimal time interval. The optimal time interval represents the peak in the number of responses, but frequently this peak represents a response rate as low as 50% with healthy subjects as shown in Figure 6.5. This is because of underlying variability in the human sensorimotor system. In order to simulate this real RFE procedure, session three was conducted using the same equation (6.1) with scaling factor 50. This scaling factor modifies the feedback so that even when subjects correctly produce the given target time the indicator will turn on with the probability of 50% for Mode 2.

For scaling factors of both 50 and 100, the mean times produced were similar to each other for Mode 2. They were 311ms for the scaling factor of 100 and 312ms for the scaling factor of 50. However, the standard deviation of the time produced increased for the lower scaling factor. The standard deviation increased to 74ms from 64ms as shown in Figure 6.7. This is because when the scaling factor is 50, the light indicator feedback does not turn on 100% when subjects produce the target time, making the feedback an unreliable measure of performance for the subjects.

Figure 6.8 shows the distribution of time intervals more clearly for both cases. Even though both targeted 300ms, Figure 6.8(a) with scaling factor 50 shows highly distributed data compared to Figure 6.8(b). As mentioned in the previous section, the average range of time intervals that possibly increase the corticospinal excitability is 40ms. 54% of time intervals were produced within $\pm$ 20ms to the target time of 300ms when the scaling factor was 100. When the scaling factor was 50, only 27% of the time intervals were located within 40ms to the target time of 300ms.

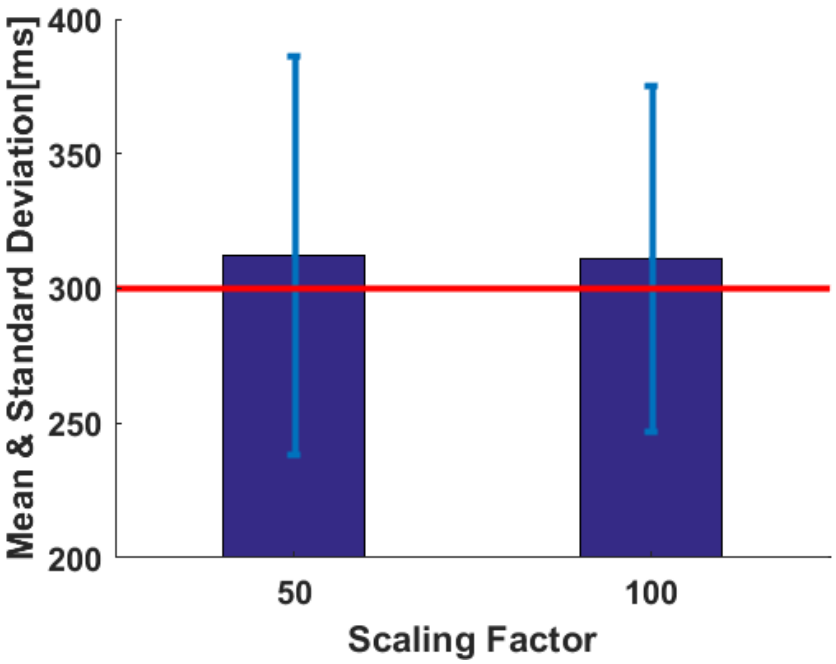

Figure 6.7: Comparison on mean and standard deviation with different scaling factors in Mode 2

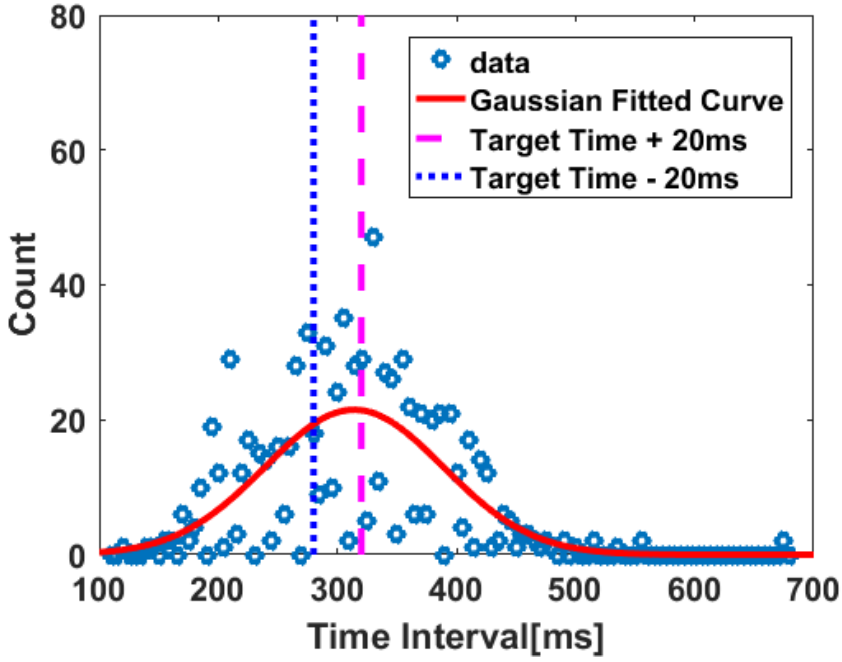

(a) Scaling Factor: 50

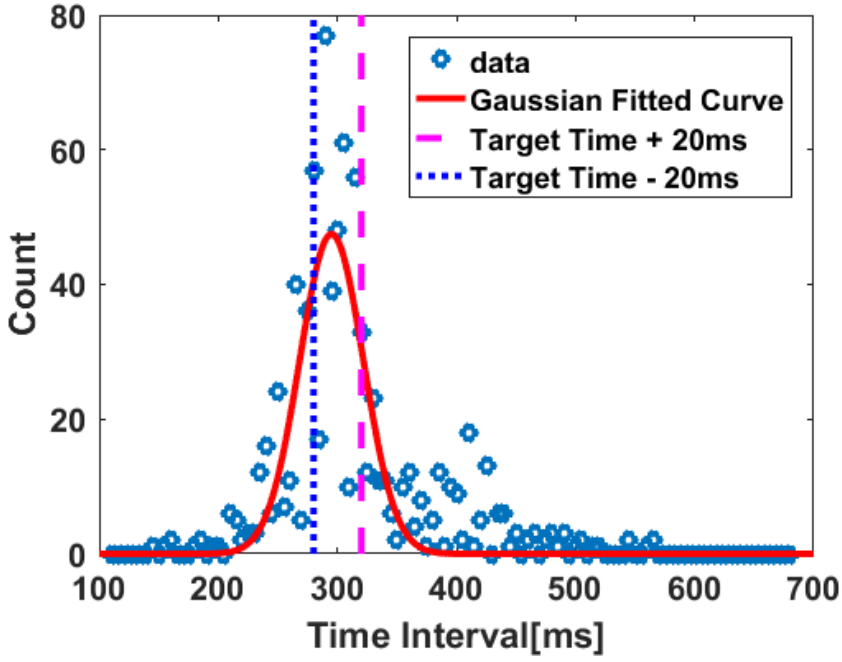

(b) Scaling Factor: 100

Figure 6.8: Time interval distribution with different scaling factors of four subjects. These are the results of time interval production tasks with mode 2 (on/off) feedback. Both (a) and (b) shared the exact same condition or mean of 300ms and variance of 100ms for the Gaussian model with only the scaling factors different. Four subjects' data were used.

6.3.3 Human and Computer Time interval Production Comparison

We observed the variability of the human subject side in the subsection. In this section, we compared the time interval production of humans with the time interval production results of the Bayesian Optimization Algorithm. Similar to the previous experiment, in this experiment, we asked subjects to produce time intervals using their fingers. And then, that time interval production was mapped to a probability via the predefined Gaussian Curve as shown in Figure 6.4 to produce visual feedback. We used on/off light feedback in order to replicate the long latency response in the EMG signal that appears when the two stimuli are temporally conditioned properly over the motor cortex. In the Bayesian Optimization algorithm, it searched different time intervals to find the target time interval that gave the highest chance of light on. It tried one time interval and observed the visual responses which were the binary information. Then it used that information to estimate the pattern of the effective time window and the acquisition function which recommended the next time interval to observe was determined based on the effective time window. They repeated this over and over again so that they could find the target time interval which outputted the most visual response which was light on. In addition, two different types of feedback were used. One feedback outputted with 100% chance at the target time and the other feedback outputted with 50% chance at the target time. 50% probability feedback was designed to replicate the low long latency response appearance from human body.

The results are shown in Figure 6.9 for 100% probability at the target time and in Figure 6.10 for 50% probability at the target time. Bayesian Optimization could find and reproduce the desired time interval more stably. Even in harsh conditions (50% response feedback), it gave a similar output as the 100% response feedback.

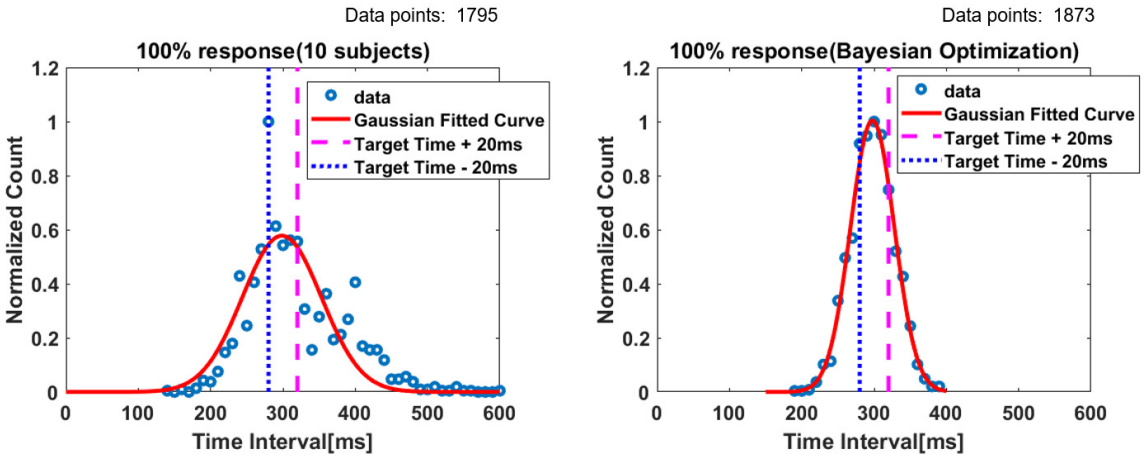

Figure 6.9: 100% probability result.

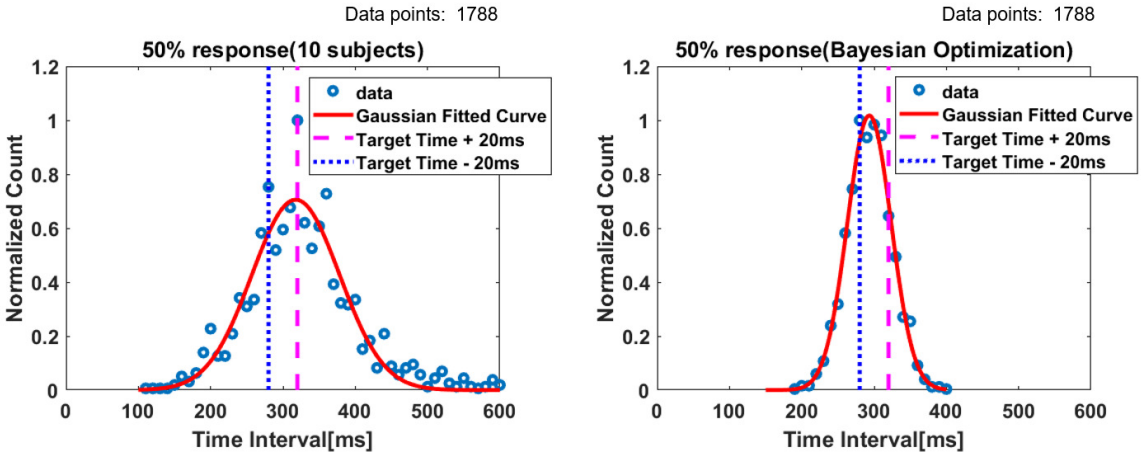

Figure 6.10: 50% probability result

Table 6.3: Time interval production result with 100% probability. Left: Human, Right: Bayesian Optimization.

mean	STD	min	max
323.1	70.7	144	1343

mean	STD	min	max
302	30.1	199	399

Table 6.4: Time interval production result with 50% probability. Left: Human, Right: Bayesian Optimization.

mean	STD	min	max
330.6	76	119	825

mean	STD	min	max
298.1	30.4	194	410

6.4 Discussion

6.4.1 Interval Production Feedback

This work showed important results that have direct application to the design of robot mediated therapeutic devices. While full automation of the RFE task may eliminate therapist associated timing errors, a potential implementation of robot assisted RFE or PAS will likely involve therapist monitoring and adjustment of stimulation parameters, as these are not constant between patients or over time. In this case, supplementation of the visual feedback provided by the patient's movements may be necessary, as a correct ISI may not even result in an observable response the majority of the time. The results of this study, specifically the performance of Mode 1 and Mode 2 in comparison to Mode 4 shows that graphic feedback is potentially a better modality than error reporting. While the larger variance shows that production of the interval is difficult for humans, the mean is very close to the desired value, demonstrating the ability to find the desired interval when given graphic feedback.

6.4.2 Human Delivered RFE

This work points to interval production as a significant obstacle to effective use of the RFE protocol as currently practiced. The mock RFE study conditions demonstrated limitations to the ability of humans to produce the necessary interval for effective RFE. It is important to note that the scale factor of 50 used (effectively a 50% response rate at the optimal ISI) was chosen based on data from healthy volunteers. It is very likely that those being treated with RFE will have much lower response rates, as the response rate is directly related to the neurological systems being treated. The mock RFE section of this study indicated that the interval production task was more difficult as the response rate (scale factor) decreased. This effect compounded the difficulty in producing the necessary ISI. The lack of responses made an already difficult therapeutic technique significantly more challenging. The 27%

of stimuli delivered within the effective window resulted in only a 13% response rate at best. Given that the response rate for stroke patients was likely to be significantly reduced, then the number of stimulation given in the effective window would also be much lower than even 27%. RFE therapy is predicated on delivery of the correct interval, and this work demonstrates the improbability of human therapists providing this even 50% of the time.

6.5 Conclusion

This study shows that the time intervals that subjects create for a given target time show huge variability, up to a 93ms standard deviation. This variability tends to increase as the target time increases. In addition, when the rate of on/off light feedback decreased to mimic variability in the RFE long latency response, only 27% of the time intervals were within $\pm$ 20 ms of the target time, which was the average range of time intervals that were expected for the response. In addition, graphic feedback was a better modality than absolute error feedback. This concludes that when designing a feedback method for RFE physical therapists, graphical feedback will better guide them to converge to the desired target more easily. In addition in order to minimize the time interval variability more effectively and enhance the rehabilitative effect of RFE, robotic assistance is necessary. The low success rate in interval production, combined with RFE's proven efficacy indicates that significant gains in stimulus delivery could be made through the use of a robotic device as a stimulus. The robotic device previously mentioned is capable of providing stimulation with a standard deviation of 5ms with the entire distribution fitting within the 40ms effective window.

CHAPTER 7
ROTATIONAL VANE ACTUATOR FOR RFE

During the RFE, a clinician applies mechanical stimulation to the dysfunctional muscle by tapping the muscle tendon and rotating wrist. In the previous chapters, a pneumatic tapping device was introduced in which mechanical simulation was inspired by the tapping action in RFE [103]. In this chapter, a rotational vane actuator for wrist rotation is introduced and dynamically analyzed to reproduce wrist rotation of RFE. Since rotation of the wrist joint follows tendon tapping in the RFE procedure, an active device that can accomplish wrist supination/pronation within a desired range and appropriate time period is necessary to reproduce the RFE-inspired robotic intervention.

7.1 Problem Statement

A rotary actuator for wrist supination/pronation must satisfy several dynamic and spatial constraints in order to be considerable for RFE-inspired treatment. First of all, the actuator should be powered by pneumatic source, sharing the same power source as the mechanical stimulator. Also, a full cycle of rotary motion should be completed within one second based on the observations in the manual therapy. The actuator should be able to provide smooth motion, exerting torque large enough for rotating the forearm of a human subject. The range of wrist supination/pronation of the human forearm is reported to be $\pm 90^o$, when the elbow joint is loose and the range is less than $\pm 90^o$ if the elbow is constrained [104, 105]. Therefore, a full revolution (360^o) is neither necessary nor recommended for safety reasons. In addition, a crucial requirement for a successful RFE assessment is the timing precision in the initiation of a rotary action, which is related to the effective ISI window. A temporal precision of 40 ms - 60 ms is expected from the actuator [6, 29].

Pneumatic actuation makes for a convenient candidate for robotic applications to re-

duce magnetic resonance noise for future EEG measurements. It is relatively safer, more hygienic and creates a negligible imaging artifact compared to other conventional technologies [106]. Pneumatic actuators can make a back-drivable, compliant interface due to the compressibility of the air, providing extra safety for human-interaction tasks. One big disadvantage of MRI compatible pneumatic systems is the long transmission lines that have to be placed between the actuator and the magnetic valves that drive them. The transmission introduces a significant attenuation in the mass flow, limiting the bandwidth of the actuation. Pneumatic systems designed for rotational motion are consist mainly of vane actuators and linear actuators with pinion-rack type of gears. Vane actuators are simply the rotational equivalents of linear pneumatic cylinders: a rotating rod divides the cylindrical actuator chamber into two sides, creating a moment when there is a pressure difference in between. Since the MRI compatibility requirement enforces using plastic materials for building the mechanisms [107], linear actuators with gears are prone to severe friction and strength problems. Vane actuators can provide a greater torque without any need for gear reduction. For the described application, a compact actuator with less complexity and higher ability to withstand torsional stress is preferable. For these reasons, the authors chose to analyze the suitability of vane actuation with long transmission lines for RFE assessment.

Both the limited space in the closed bores of MRI machines, the timing precision and max torque requirements of the wrist rotation step in the RFE treatment, necessitate a thorough dimensional analysis on the design of a rotary vane actuator. Figure 7.1 shows a typical schematic of a vane actuator. Generally, a larger rotor height, h, would allow for a greater moment arm and rod area, satisfying the torque requirement with less pressurization. The radius of the actuator, hence the rotor height, is primarily determined by the available space around the patient in the MRI bore. Yet, the depth of the actuator is not constrained by the environment and could be arbitrarily chosen. The height and depth of the actuator cylinder have a non-trivial effect on the dynamics of the actuator, and requires

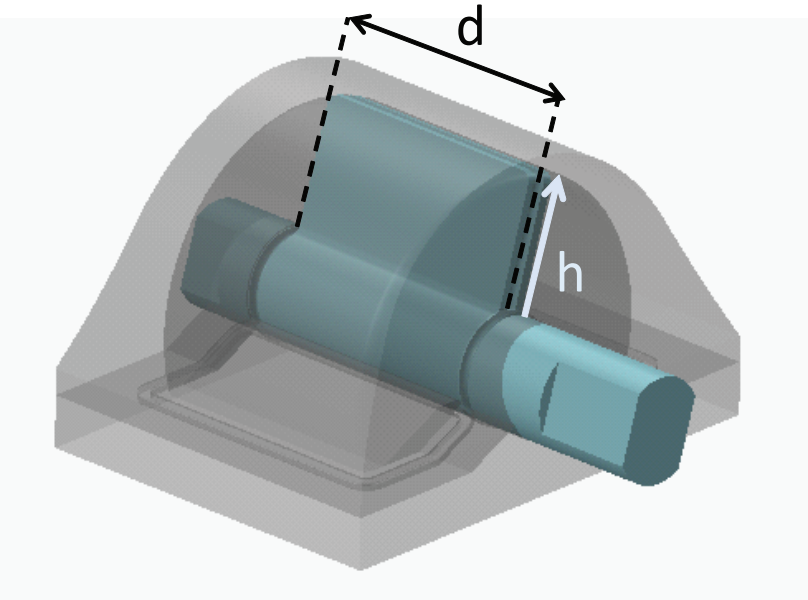

Figure 7.1: Proposed rotational actuator with rotor dimensions.

a nonlinear dynamic analysis. These parameters affect both the chamber volume and the resultant moment, causing a larger torque generation with the same pressurization but a slower pressure build up due to the larger volume. The rise time of chamber pressure becomes a greater problem when the actuator is driven via long transmission lines; therefore, the trade-off in changing the actuator volume needs to be elaborated. 3D printed version of the rotational vane actuator is shown in Figure 7.2

Vane actuators have been previously developed [108] and tested for MRI environments [109]; however, a pneumatically driven, tele-operated version is yet to be introduced and analyzed. Sorli et al, simulated the response of a given vane actuator; however, their study did not include significantly long transmission lines and was not aimed for a dimensional analysis [110]. This work aims to examine the feasibility of wrist supination/pronation for RFE-inspired treatment with a pneumatic vane actuator. The dynamic performance of the pneumatic system is simulated using a detailed model of a pneumatic system with long transmission lines [111], and rotor dimensions were varied to obtain a suitable actuator configuration for the aforementioned purpose.

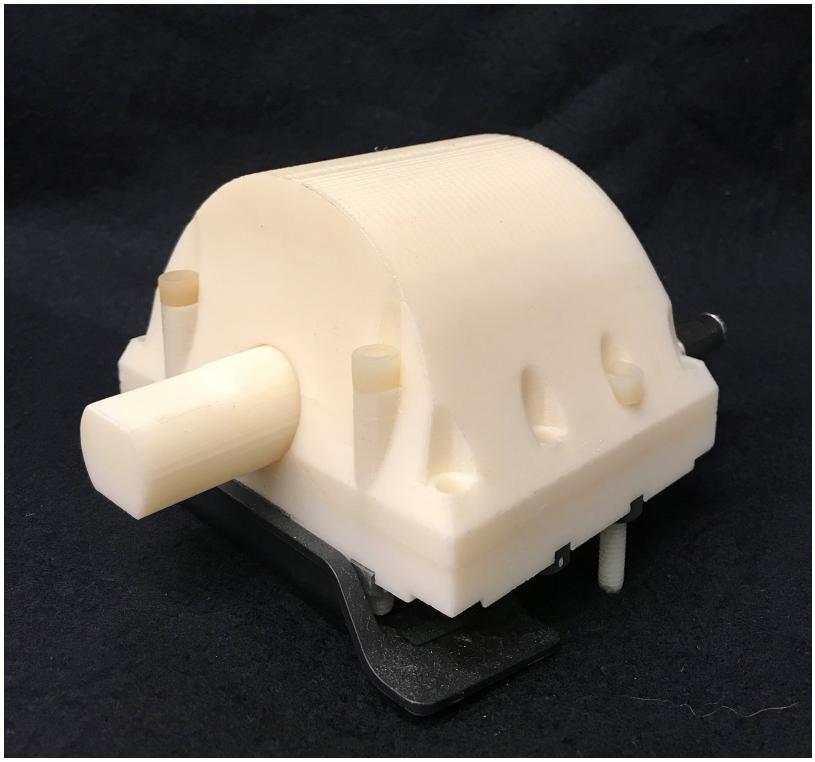

Figure 7.2: 3D printed version of the rotational vane actuator.

7.2 Previous Design

Previously, the first version of the pneumatic rotation device was developed and reported in [112]. This first version prototype assembly is shown in Figure 7.3 and 7.4. The first version with the tapping device (i.e., mechanical stimulator) attached together is shown in Figure 7.5. This first version consists of an arm rest, hand clamp, circle ring and the vane actuator. The arm rest supports the upper limb and the hand clamp holds the hand tightly so that it can rotate the wrist by the vane actuator. The circle ring is a ring with a guide that limits the angle of rotation up to 180 degrees. The vane actuator creates circular motion of the connected shaft to rotate the wrist. Figure 7.6 shows the working principle of this vane actuator. Compressed air flows into the left air port on the vane actuator to the left chamber while the right chamber has atmospheric air via the right air port. This rotates the shaft inside the vane actuator. Detailed CAD drawings can be found in Appendix A.2.

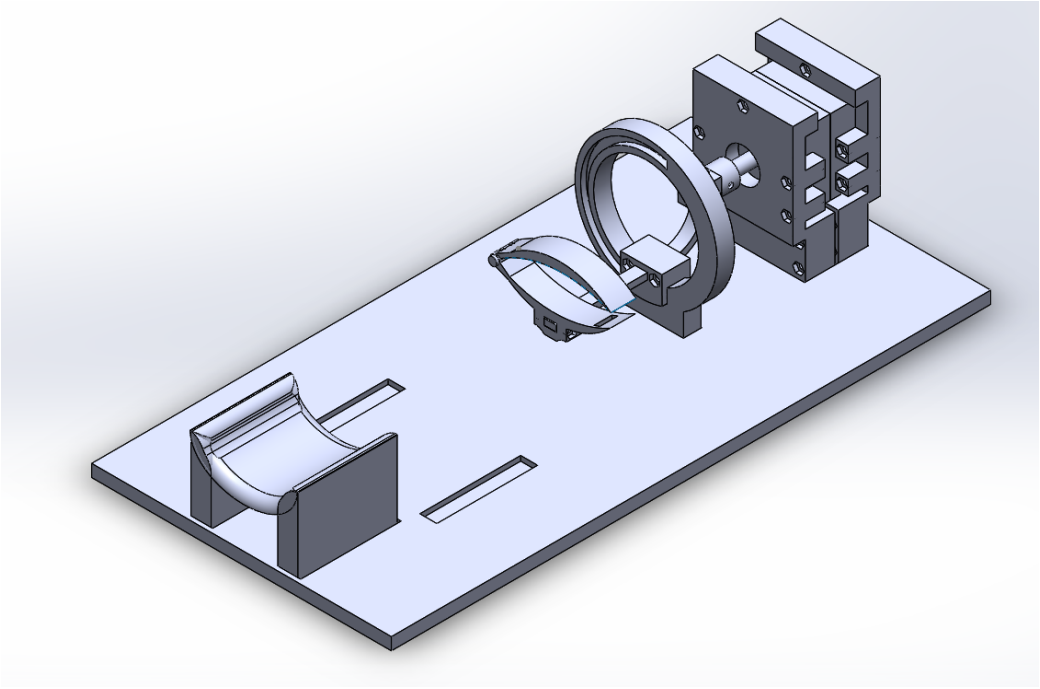

Figure 7.3: First version prototype CAD in isometric view.

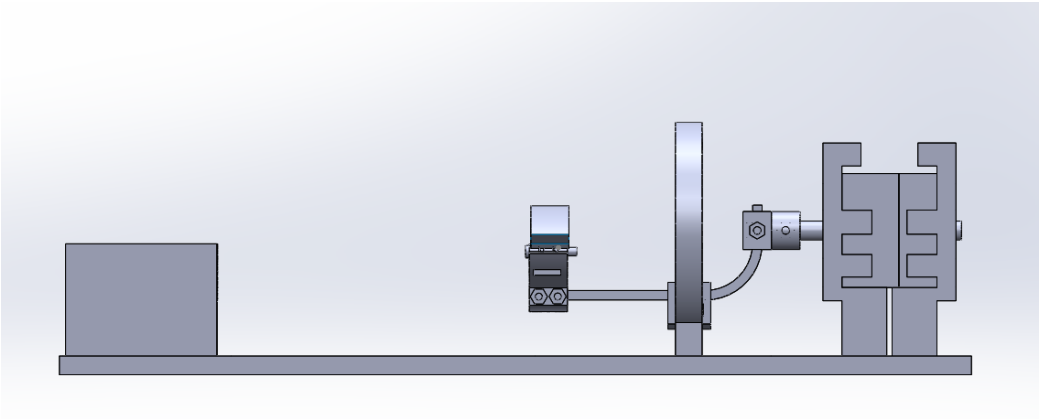

Figure 7.4: First version prototype CAD in side view.

7.3 Numerical Analysis

A complete model of the system that consists of a time-delayed pneumatic system model and the dynamic model of the rotor shaft was developed to estimate the range of output rotation within 1 second. Also, the initial time delay between the input command and the start of the motion was estimated to see a typical magnitude of break-away delay. These estimations were performed for a range of rotor height, h, and depth, d, values. This section

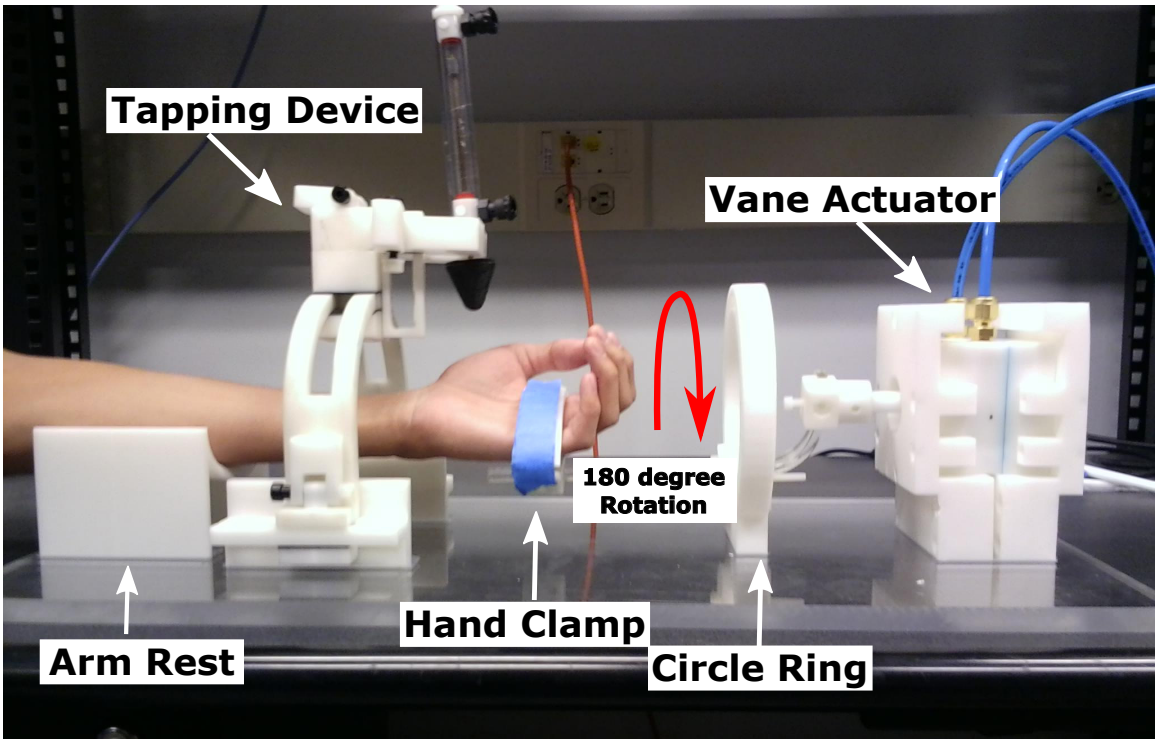

Figure 7.5: First version prototype.

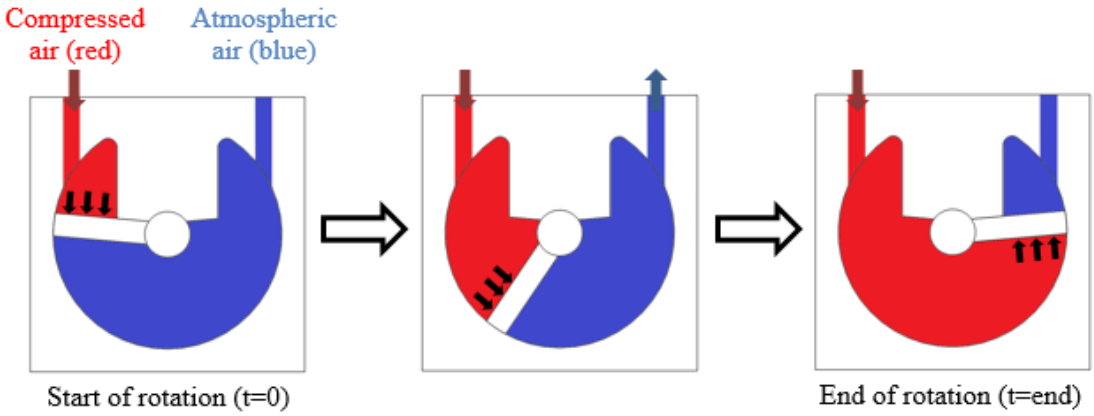

Figure 7.6: Diagram of how the vane actuator works.

describes the modeling effort and the physical parameters assumed for numerical analysis.

7.3.1 Pneumatic System Model

A simple, yet accurate method for pneumatic systems with long transmission lines has been introduced by the authors in an earlier study [111]. As shown in Figure 7.7, the line

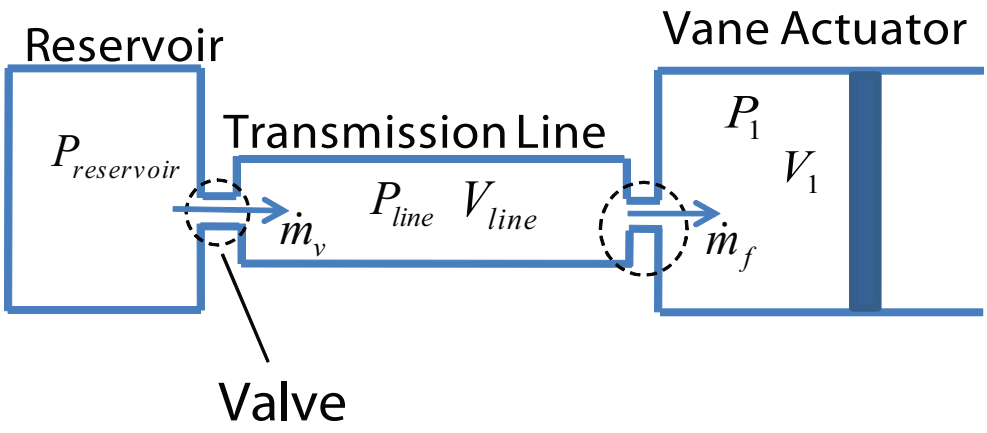

Figure 7.7: Pneumatic system model utilized for simulation [111]

was modeled as a separate volume serially connected between the valve and the actuator chamber, resulting in a total of three chambers serially connected. An actuation delay and pressure attenuation expected in the system can be predicted this way, enabling one to see the feasibility of a given actuator for robotic RFE-inspired treatment.

The flow from the reservoir to the line or from the line to ambient is provided through an isentropic orifice at the electronic valve that operates in the control room. The mass flow rate through a valve orifice is related to the area of the valve opening by a well-established formula:

$$\dot{m}_v = C_0 \psi(P_u, P_d) \tag{7.1}$$

where C_0 is the sonic conductance of the valve at a given input command, and ψ is a piece-wise function of the upstream P_u and downstream P_d pressures across the valve, defined as follows:

$$\psi(P_u, P_d) = \begin{cases} \frac{k_0 P_u}{\sqrt{T}} & \text{if } \frac{P_d}{P_u} \geq C_r \\ \frac{k_0 P_u}{\sqrt{T}} \sqrt{1 - \left(\frac{\frac{P_d}{P_u} - C_r}{1 - C_r}\right)^2} & \text{if otherwise} \end{cases} \tag{7.2}$$

where k_0 represents a combination of orifice flow parameters determined with respect to standard conditions [113], C_r is critical ratio of the pressures that determines whether the flow is choked or unchoked. C_0 defines the mass flow capacity of an orifice that is dependent on the area of the valve opening. The temperature at the orifice, T, is assumed as

constant and equal to the room temperature (293^oK) in our application. C_0 and C_r for the servo valve were obtained by calibration routines based on ISO-6358 standards [114].

The upstream and downstream pressures of the valve are determined by the direction of the flow, i.e. the sign of the valve area, as described below:

$$\psi(P_u, P_d) = \begin{cases} \psi(P_{reservoir}, P_{line}), & \text{if } C_0 \geq 0 \\ \psi(P_{line}, P_{atm}), & \text{if otherwise} \end{cases} \tag{7.3}$$

where $P_{reservoir}$ is the reservoir pressure, P_{line} is the chamber pressure and P_{atm} is the ambient pressure. The flow between the line and the actuator chamber is described assuming another orifice on the fitting that connects the line to the chamber of the actuator [113, 115]. The flow through the fitting is derived as follows:

$$\dot{m}_f = C_f \psi(P_u, P_d) \tag{7.4}$$

where the upstream pressure P_u is the higher one between P_{line} and $P_{actuator}$; and the direction of the flow is from the chamber with higher pressure to the other one. The discharge coefficient at the fitting C_f is obtained empirically.

The actuator and the transmission line are assumed as isothermal chambers, since the designed frequency of operation in this study is low; hence, these processes are slow enough to allow for a heat exchange [116, 117]. Therefore, the dynamics of the pressure in the actuator becomes:

$$\dot{m}_f RT = P_{actuator} \dot{V}_{actuator} + \dot{P}_{actuator} V_{actuator} \tag{7.5}$$

where R represents the thermodynamic gas constant. In addition to the mass flow rate through the fitting described in the original model, a leakage that is proportionate to the chamber pressures is added in this work. The maximum rate of volumetric leak is deter-

mined to be $0.5\frac{l}{min}$, which is a typical value for similar systems [113].

The line pressure, P_{line}, at the fitting is calculated using a similar dynamic equation. However, the mass flow through a transmission line has a finite velocity; hence, a time delay in the mass transportation between the two ends of a line is accounted. That transportation delay is calculated as follows:

$$T = \frac{L}{c} \tag{7.6}$$

where L is the length of the line and c is the speed of sound in air [118, 119]. The time delay attributed to the length of the line is added to the flow through the valve when the pressure dynamics of the line is computed:

$$\dot{P}_{line}(t)V_{line} = \dot{m}_v(t-T) - \dot{m}_f(t) \tag{7.7}$$

where V_{line} is the constant volume of the line.

7.3.2 The Load Dynamics

The dynamics of the actuator shaft can be characterized with a typical moment equation with respect to the central axis of the shaft. The equation below is established using the variables shown in Figure 7.8:

$$I\ddot{\theta} = (P_1 - P_2)A(\frac{d}{2} + r) - M_{ext} - M_f - B\dot{\theta} \tag{7.8}$$

where A is the area of the rotor, calculated by multiplying h with d and I is the total rotational inertia of the whole system. M_f represents the torque created by friction. M_{ext} is the combined moment on the actuator rotor induced by the external components such as the forearm, the added load and the shaft that fastens the arm to the actuator:

$$M_{ext} = (Gl + G_{shaft}l_{eq})\sin(\theta - \frac{\pi}{2}) \tag{7.9}$$

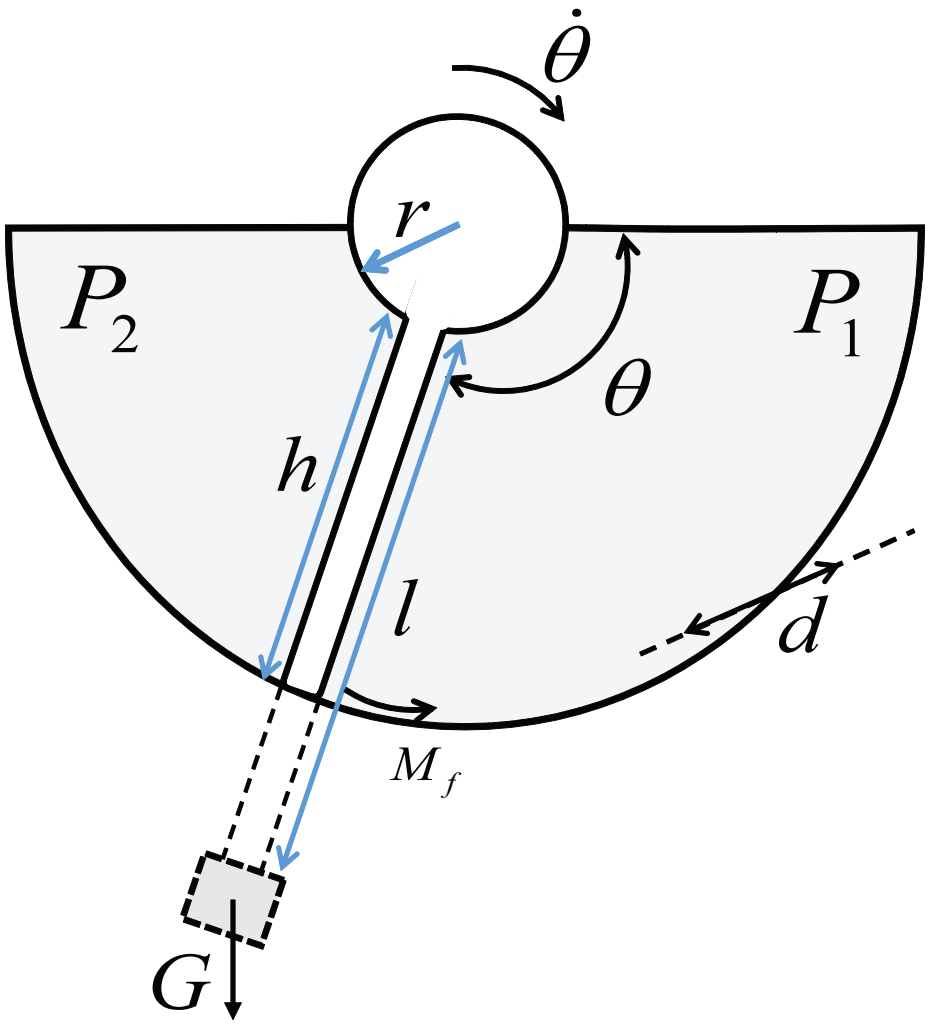

Figure 7.8: Parameters involved in the dynamics of the rotor shaft.

G, illustrated in Figure 7.8, stands for the combined weight of the load and the forearm which are modeled as equally distant to the center of the actuator. The radial location of the shaft's center of mass, represented by l_{eq}, differs from that of the load, l, and depends on the design of the shaft.

7.3.3 Simulation Parameters

The parameters utilized on both the pneumatic system model and the dynamic equation for the actuator rotor are listed in Table 7.1. During the simulation, the valve is given a full-range square wave excitation of 1 sec duration. Since the two outlet ports of the valve

Table 7.1: Simulation parameters.

Parameter	Value
r	$12.5mm$
l	$60mm$
l_{eq}	$25mm$
G_{arm}	$5N$
G_{load}	$1 - 10N$
G_{shaft}	$2N$
M_f	$2.7Nm$
B	$0.3\frac{Nm}{rad/s}$
I_{shaft}	$3.3e-4kgm^2$
I_{arm}	$7.2e-4kgm^2$
θ_0	$\frac{\pi}{2}$
P_{10}	$1bar$
P_{20}	$1bar$
h	$7.5mm - 37.5mm$
d	$12.5mm - 150mm$

do not have an equal flow capacitance, the duty cycle of the excitation signal is adjusted to obtain a symmetrical output. The reservoir pressure, $P_{reservoir}$, is set to be $4bar$ which is a moderate magnitude generally available in healthcare centers.

The angular range of the resultant motion and the time it takes for the system to overcome the break-away pressure are analyzed for a range of actuator depth, d, and height, h, values given in Table 7.1. The initial chamber position, θ_0, and pressures, P_{10}, P_{20}, are also listed on the same table.

The dimensional parameters utilized in (7.8) are obtained considering the CAD model, shown in Figure 7.1, that represents a suitable actuator. M_f is calculated assuming a highly conservative break-away pressure of 0.4 bar. A damping coefficient, B, is added to the equation in order to represent the cross-leakage between the cylinder chambers.

The inertia of the system is calculated combining the inertia of the shaft, arm and the added weight. The inertia of the shaft, I_{shaft}, is obtained using the CAD model via Solidworks software. Added weight is described as a point mass, hence its inertia, I_{load}, is

calculated accordingly. Approximating the inertia of the forearm, I_{arm}, is a complex task and it is not addressed in this work. Rather, the arm is modeled as a cylinder of 40 mm radius, being rotated about its longitudinal axis. The weight of that representative cylinder is assumed to be $0.9kg$, half of an average weight of a forearm [104].

7.4 Simulation Result

The results of the dimensional analysis are summarized in two contour plots, given in Figure 7.9. For a successful RFE assessment, a full range (180^o) of output displacement is required within 1 second. In addition, the magnitude of the initial time delay in the actuation should be low for a promising timing precision in the time of motion start. The contour plots show that a full-range output can be achieved on a certain subset of the analyzed parameter range. The relationship between the dynamic response of the system and rotor dimensions is not monotone, i.e. increasing both height and width does not result in a more agile actuation. In contrast, initial time delay has almost a monotonic relation. Excluding the sub-optimal range of very low rotor dimension values, a bigger actuator generally results in a lower time delay.

The resultant variation in the dynamic performance with regard to increasing rotor height can be seen in Figure 7.10. A rotor depth of 150 mm allows the rotor height to be between 10-17.5 mm, making the actuator comfortably compact. The delay in the same configuration appears to be 80-100 ms.

Figure 7.11 allows for a comparison between a high value of rotor depth to a lower one when the height stays constant. The output displacement and pressure difference between the actuator chambers are illustrated in time domain. The configuration with the smaller actuator volume has a faster pressure build-up, developing a faster motion within the same time frame.

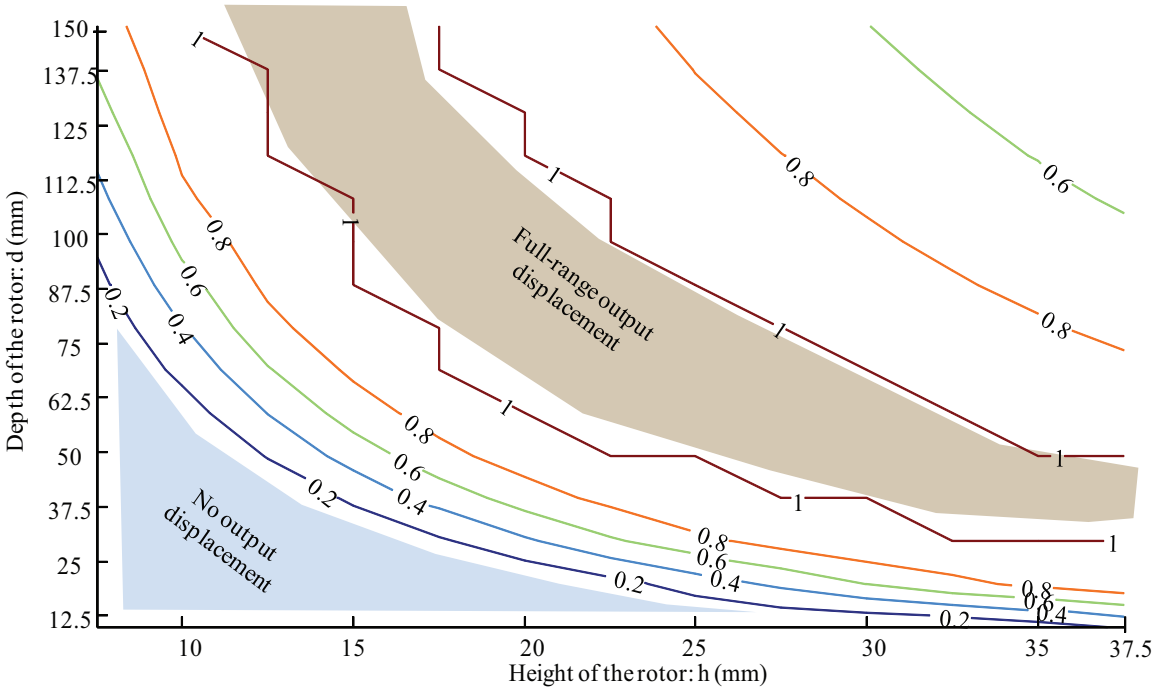

(a)

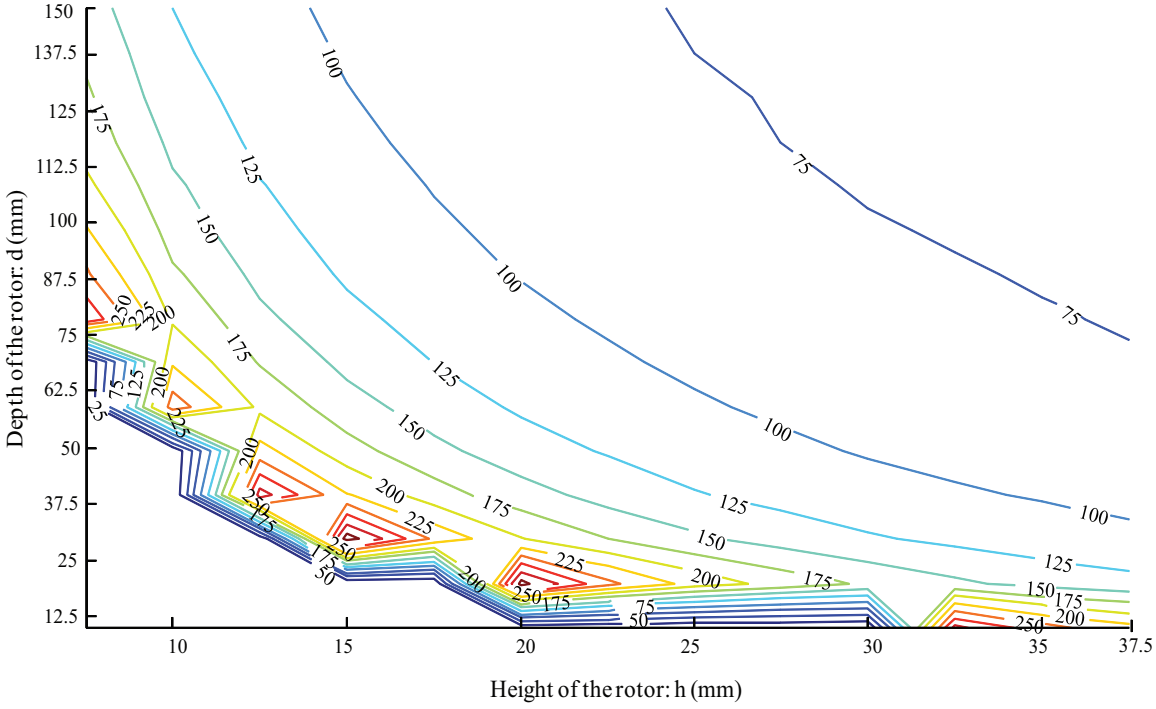

(b)

Figure 7.9: Contour showing the dynamic performance of the actuator for a range of depth, d and height, h (a) The normalized range of output displacement (b) The break-away time after the initial input command in ms

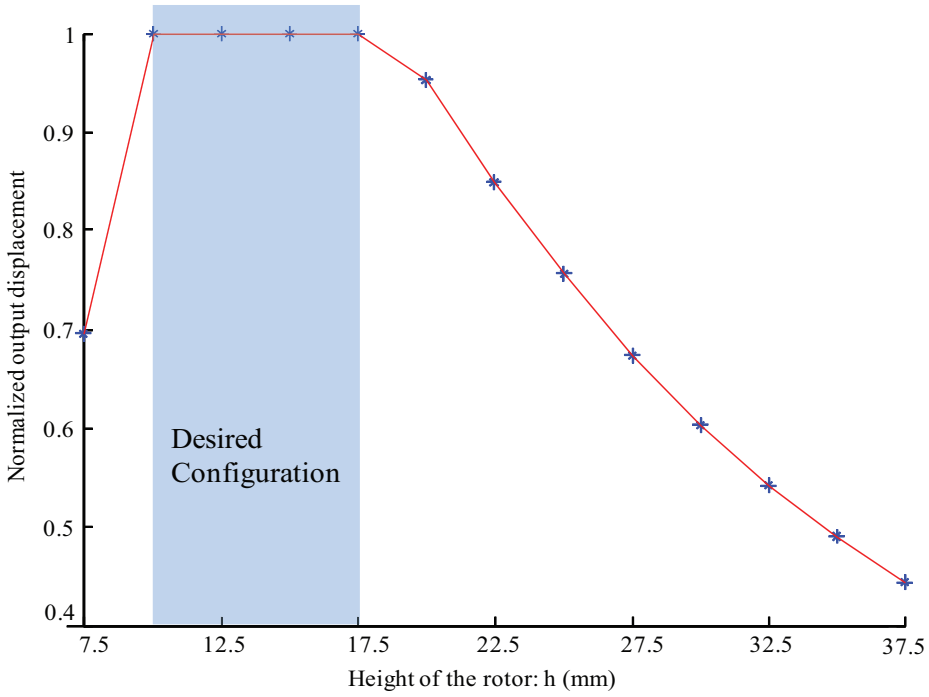

(a)

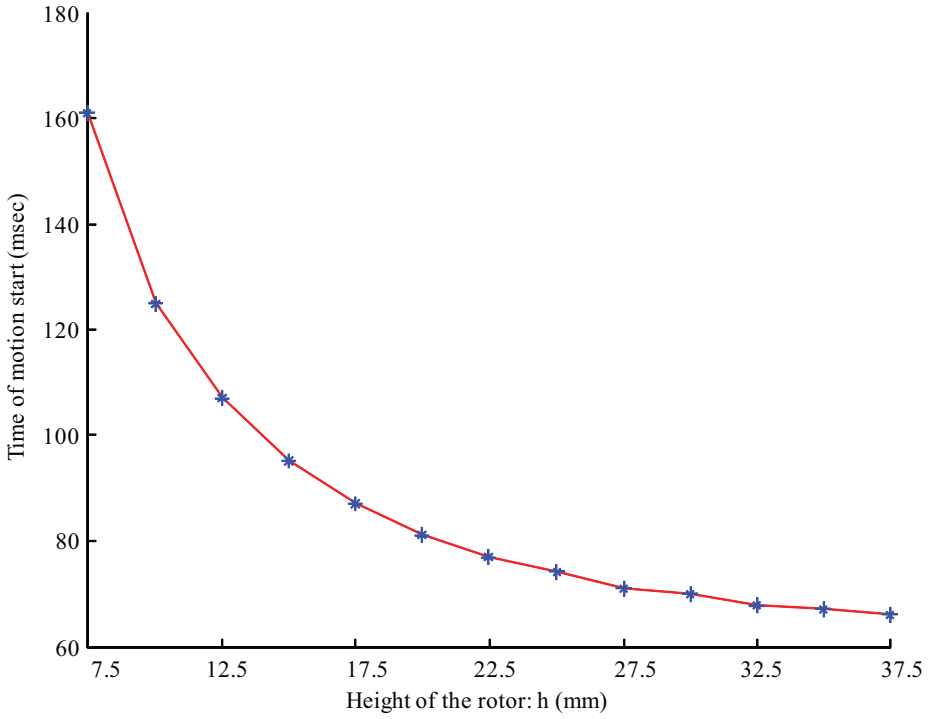

(b)

Figure 7.10: Dynamic response for various actuator height, h as d=150 mm (a) The normalized range of output displacement (b) The break-away time after the initial input command

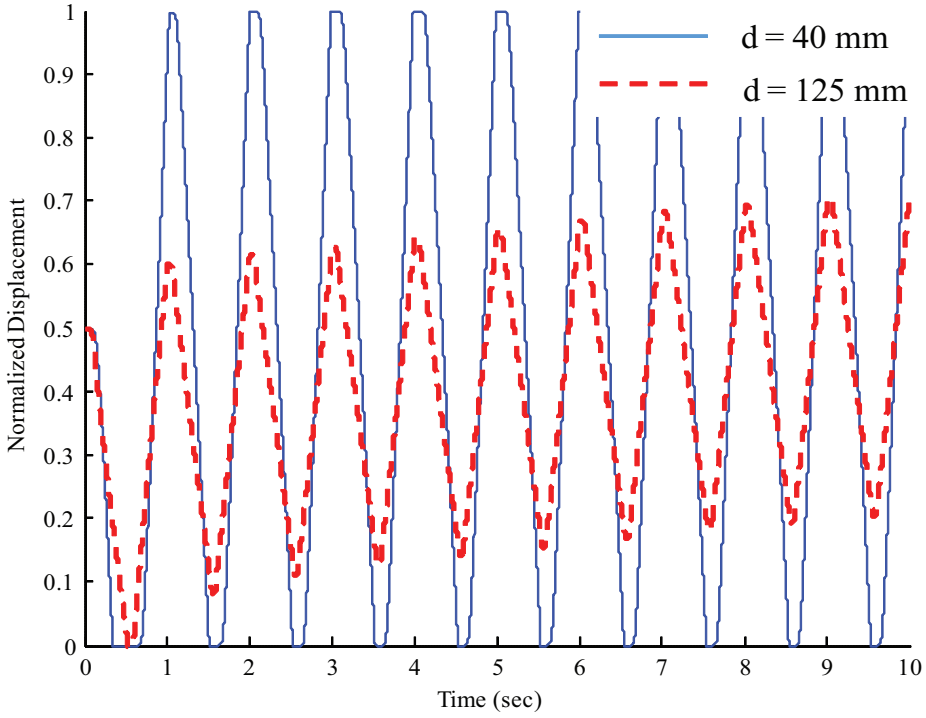

(a)

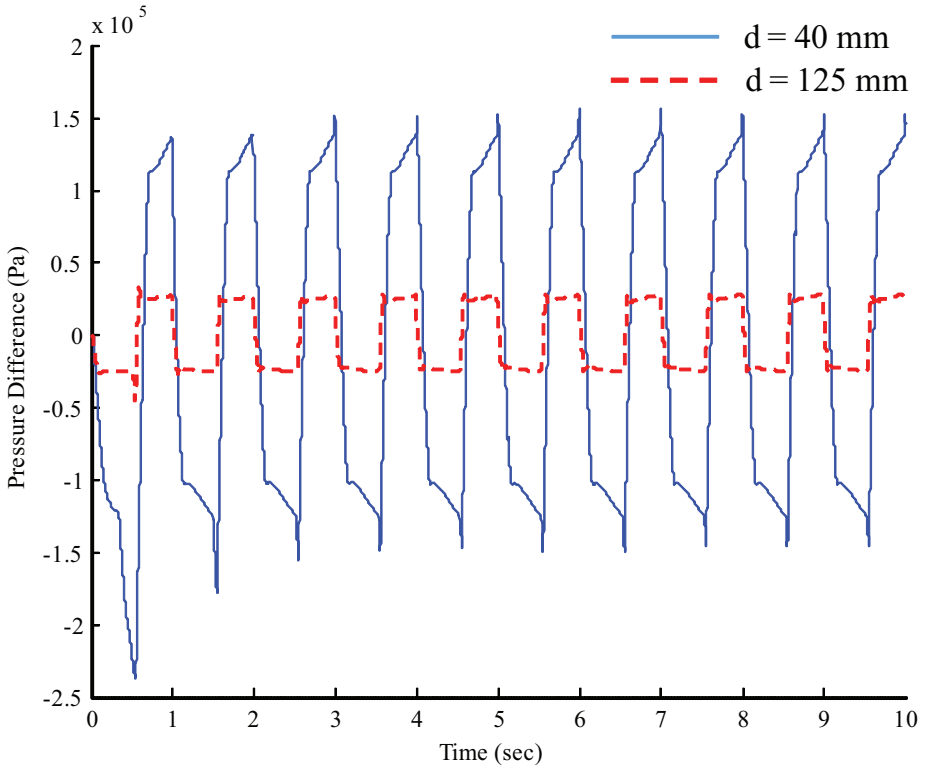

(b)

Figure 7.11: Comparison of the dynamic response of the actuator configurations with two different depths: 40 mm and 125 mm (a) the normalized displacement of shaft rotation. Each depth had normalized velocity, $\pm$ 2/sec and $\pm$ 1.2/sec, (b) the pressure difference between the actuator chambers

7.5 Discussion

The results of the analysis described in this work reveal important details on the feasibility of wrist rotation for RFE-inspired treatment, The analysis is made for a specific range of rotor height and depth, In that range, a bigger actuator does not always yield a better dynamic performance. Moreover, for a fixed value of actuator depth, there is no monotone relation between the speed of the actuation and rotor height. The actuator can be designed to serve better without occupying all the available radial space in the bore. This can be explained by considering the effects of rotor dimensions on the chamber volumes; hence, the inertia in the pressure dynamics. A higher volume can kill the advantages of having a greater maximum torque, by slowing down the pressure build-up in the chambers.

Another outcome of this study is the estimated initial time delay values. By choosing an optimal set of dimensions, a time delay of 80-100 ms is achievable. A timing precision of 40-60 ms in the motion initiation timing is required for successful RFE-inspired implementation [6, 29]. Although these estimations would not allow for a conclusion on the timing precision of the motion start, some deductions can be made by comparing these estimated delay magnitudes to those of a pneumatic, linear actuator with long transmission lines experimentally obtained in an earlier study [103]. MRI compatible linear actuators, utilized for tendon tapping, as in the first step of RFE treatment, presented an average time delay of 200 ms between the input command and tapping with a standard deviation of 5 ms. Given the similarity in the actuation types, vane actuation that has an even smaller magnitude of time delay can be promising. Admittedly, future experimental study is required for a conclusive argument.

The simulation results on the range of output displacement indicated that the pressure dynamics of the system has a superior influence on the motion compared to the load dynamics. The region of optimal actuator dimensions, shown in Figure 7.9, describe a unique range of actuator volume for the given task despite the variation in the effective moment

arm of the generated actuator force. The effects of the extra load on the shaft was also examined in this study. The dynamic performance of the system was not sensitive to a payload range of 0.1-1 kg indicating the dominant role of pneumatic on the motion. Dominance of pressure dynamics is particularly beneficial for it provides robustness against noise due to the variance in the size of the human forearm.

Structural properties of the actuator, such as leakage and the break-away pressure, affects the initial time delay of the motion start rather than the range of the motion. In this study, the magnitudes of such parameters were kept within the range of industrial standards. A further study might be needed in the case of non-standard leakage and stiction on the pneumatic actuator. A constant friction moment was assumed in the simulation model. An elaborate friction model is necessary for further analysis on the effects of dynamic friction and external load.

7.6 Conclusion

Pneumatic vane actuators provide a smooth and compliant rotary motion in a simple and compact way; therefore, these systems appear to be promising for tele-operated robotic rehabilitation in MRI. In this work, the feasibility of implementing an emerging physiotherapy technique developed for hemiparesis patients, or RFE, with a vane actuator is analyzed. Under the spatial constraints imposed by the tight space in the MR-scanner, the actuator is expected to initiate wrist pronation/supination at a certain timing instant and complete the motion in 1 second. A detailed pneumatic system model that involves the effects of long pneumatic transmission tubes is utilized to estimate the dynamic response of a vane actuator for a range of rotor sizes that would meet the spatial constraints. Our analysis revealed that a pneumatically driven, tele-operated vane actuator could realize the targeted rehabilitation procedure. The inertia in the pressure dynamics of the system plays a dominant role against the rotational dynamics of the actuator shaft, making a more compact actuator chamber more effective. The rotor size of the actuator can be adjusted for a

very comfortable fit into MR-scanners. This work is focused on a simulation-based feasibility analysis for vane actuators. The outcomes of this study will be experimentally tested and validated in future work.

CHAPTER 8
CONCLUDING REMARKS

In this thesis, the underlying mechanism of the paired brain stimulation with mechanical stimulation was investigated. Inspired by both the conventional PAS and RFE, this paired brain stimulation was coupled with mechanical stimulation. Changes in instantaneous neural excitability were observed by means of MEP. The human interval production experiment was conducted to examine how much variability manual mechanical stimulation by humans produced, motivating the necessity of a robotic system for mechanical stimulation. In order to provide reliable mechanical stimulation with precise timing, the mechanical stimulator was developed. This stimulator was able to apply mechanical stimulation to the wrist tendon with high timing precision within a 2ms STD. Four statistical regression methods were applied to estimate the effective ISI-W for each individual. These methods estimated the ISI-W with fewer stimulation trials compared with the conventional incremental method. The developed mechanical stimulator and the regression methods were integrated into closed-loop determination of ISI-W. With this automated system, the human operator's involvement to manually determine or adjust the ISI would not be necessary. In order to reproduce the RFE intervention, a rotational vane actuator was developed analyzed to perform the wrist pronation and supination.

The research described in this thesis provides original contributions as summarized below:

- The pneumatic mechanical stimulator was developed, and its timing precision was tested to provide reliable mechanical tendon tapping. The mechanical stimulator was designed with MRI safe materials for future study in an MRI scanner. The accelerometer attached to the hammer successfully detected the impact time of the hammer at specific tendon tapping times. These were repeatable under 5ms STD.

- Four statistical regression methods were applied to estimate the effective ISI-W of each individual efficiently. These regression methods reduced the number of observations to individually determine the effective ISI-W up to 6.5% of that of the conventional incremental method. This reduced the physical burden on the subject by reducing the number of stimulation trials and total experimental time.

- Online ISI-W estimation were tested in real experimental setup to validate it's performance. The system could adjust the ISI in each trial based on the MEP measurements and inform the next ISI. An online estimation algorithm had been applied to experiments with two subjects. ISI-W estimation results were highly correlated with the measured ground truth ISI-W, with the correlation coefficient around 0.83. The number of observations was less than 25 which was less than 8.7% of the number of observations required by the conventional incremental method.

- The human time interval production experiment was conducted to analyze the characteristics of human time interval production and to provide a proof of necessity of a robotic system for mPBS. This study showed that the time intervals that subjects created for a given target time had large variability, up to 93ms of standard deviation. Considering the average length of the effective ISI-W, 108ms, this large timing variability from human tapping motion would not be acceptable for performing timing-critical mPBS. Mechanical stimulation by the mechanical stimulator should be advantageous.

- A rotational vane actuator was developed to perform the wrist pronation/supination task in RFE and its design was discussed. This work focused on the actuator design and simulation-based analysis of the vane actuator. A pneumatic dynamic model including the effect of long pneumatic transmission lines was utilized to characterize the dynamic response of the vane actuator. A time delay of 80-100 ms which is the delay between the command and the real actuation was achievable.

8.1 Future Work

8.1.1 Somatosensory Evoked Potential Measurement in mPBS

In this thesis, the EMG measurement was utilized to observe the neural excitability change in response to the mPBS. In order to analyze the direct neuromodulation effect, electroencephalography (EEG) experiments will be required by measuring somatosensory evoked potentials (SSEPs) from the motor cortex [120].

8.1.2 Rotational Vane Actuator

To date, the rotational vane actuator has been developed and tested on a simulation-based feasibility analysis. The outcomes of this study can be experimentally tested and validated in subsequent investigations. In addition, in order to conduct the RFE procedure which includes both a tendon tapping task and a wrist rotation task, this vane actuator can be combined with the mechanical stimulator proposed in this study to reproduce RFE-inspired procedure, leading to further investigation of the efficacy of RFE using robotic systems.

8.1.3 Evaluation of mStim-induced Neuromodulation using Subthreshold and Suprathreshold TMS

For this thesis, subthreshold TMS (i.e., 90% RMT) was used for all of the experiments. With the subthreshold TMS, only enhanced neuromodulation was detected. Suprathreshold TMS (e.g., 120% RMT) allows for identifying not only facilitatory neuromodulation, but also inhibitory neuromodulation. As a result, MEP profiles tend to be more complex, providing more information. In order to conduct detailed measurements investigating the enhancement and depression of MEP amplitude, suprathreshold TMS experiments will be necessary. According to reported results on Estim induced neuromodulation, a transition from inhibition to facilitation is expected for a smaller ISI, appearing on the left of the MEP distribution. Smaller ISI increments will be required to characterize such responses.

Table 8.1: Normality test.

	Test Statistic	**p-value**	**Normality**
Subthreshold	0.9229	0.0992	1
Suprathreshold	0.9418	0.0398	0

As a pilot study toward the ultimate research goal, neuromodulation via mechanical stimulation combined with suprathreshold TMS was conducted and compared with the one from subthreshold TMS as shown in Figure 8.1 for a limited number of subjects. In this pilot measurement, an increment of 1 ms was used from an ISI ranging from 30 to 60ms to collect data for possible inhibition due to Mstim. Due to the complicated profile of ISI-W with the suprathreshold TMS, a single-Gaussian model may not be sufficient for modeling the MEP profiles. As shown in the normality test result in Table 8.1, the ISI-W profile of suprathreshold TMS is not normal. Figure 8.2 shows how a sample MEP profile with suprathreshold TMS can be appropriated by Gaussian fittings with a different number of Gaussian functions. Unlike the MEP profiles with Mstim and subthreshold TMS, a simple Gaussian approximation would not work for suprathreshold TMS. MEP with suprathreshold TMS should be characterized and the correlation between subthreshold and suprathreshold TMS results should be investigated. This observation motivates the use of solely facilitatory MEP using subthreshold TMS to roughly estimate the individual ISI-W as a first step and then utilize that window (i.e., ISI-W from subthreshold TMS) developed in this thesis for future neuromodulation analysis as a second step with suprathreshold TMS.

Note that suprathreshold experiments take even longer compared with subthreshold experiments, leading to an increased physical burden on subjects due to stimulation with high intensity. In addition, it would introduce other problems such as coil overheating [121, 122, 123]. Such issues should be addressed and resolved while conducting future research.

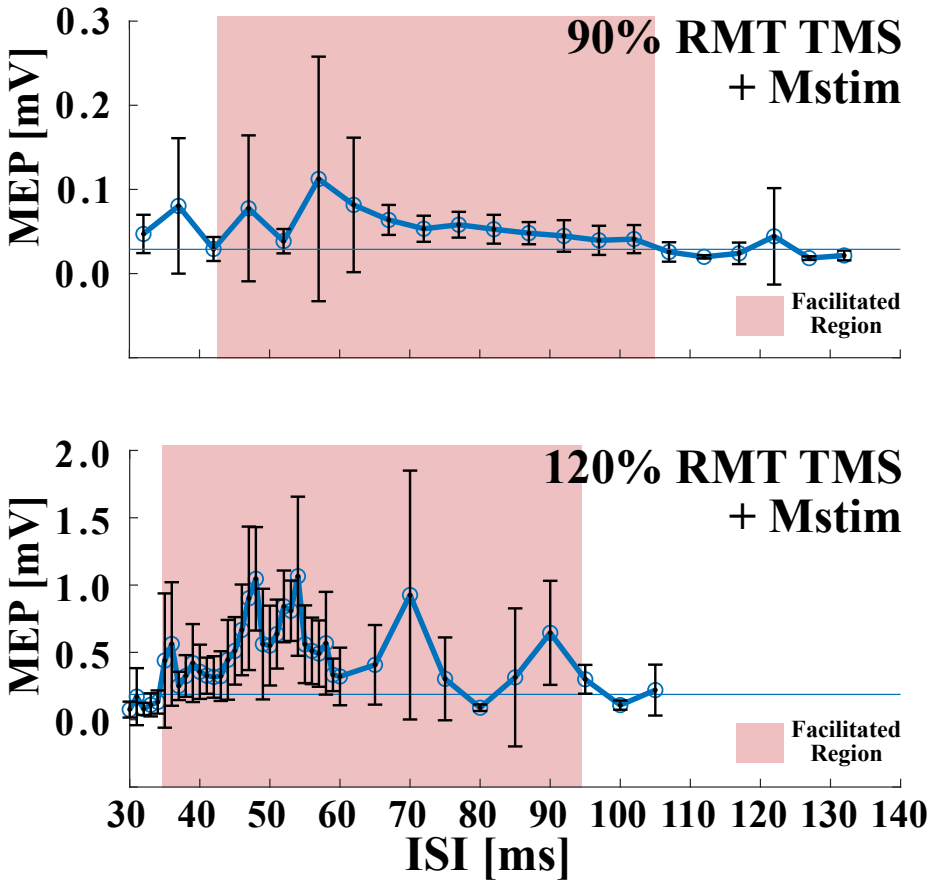

Figure 8.1: Characterization of MEP with supra-threshold TMS. Sub-threshold (90%RMT TMS, top) and Supra-threshold (120%RMT TMS, bottom) MEP measurements of one subject (n=1) with Mstim along ISI. MEP with sub-threshold TMS was between 0.0 0.3 mV whereas MEP with supra-threshold TMS was between 0.0 2.0 mV. Note that supra-threshold TMS induced approximately ten times greater MEP in amplitude than the sub-threshold TMS did.

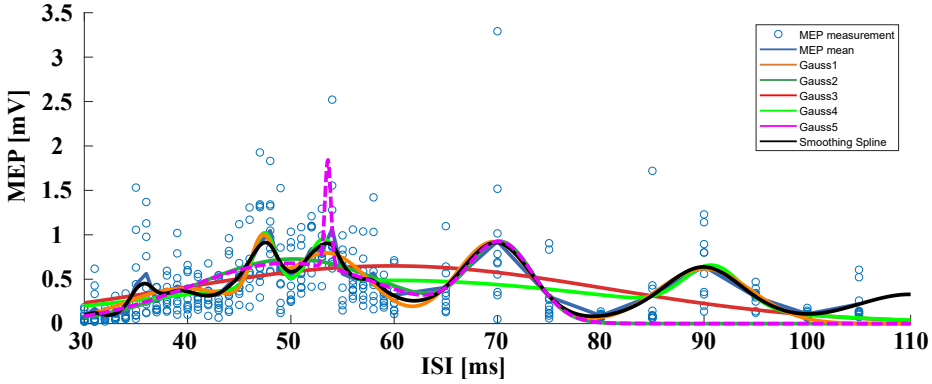

Figure 8.2: Gaussian curve-fitting of MEP with supra-threshold TMS (120% TMS) using one to five Gaussian functions and a smooth spline.

Appendices

APPENDIX A

MECHANICAL DEVICE PARTS

A.1 Mechanical Tapping Robot

A.1.1 3D Models

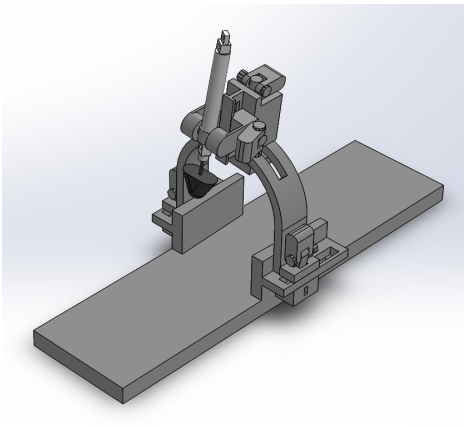

Figure A.1: 3D model of a mechanical tapping device assembly (Isometric view)

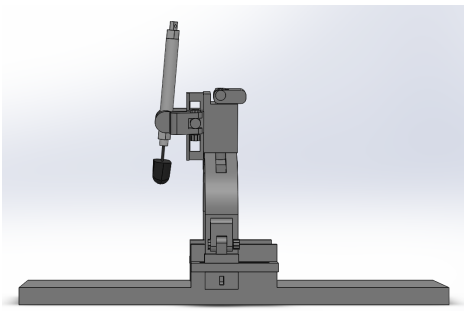

Figure A.2: 3D model of a mechanical tapping device assembly (Side view)

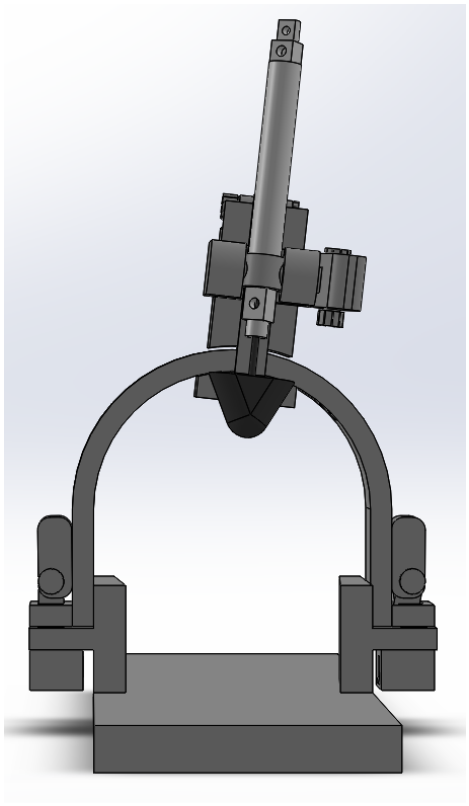

Figure A.3: 3D model of a mechanical tapping device assembly (Front view)

A.2 First Version of Rotational Device

Jonathan Lai and Johnathan Williams developed the first version of the pneumatic rotation device.

A.2.1 CAD drawings of parts

The dimensions shown in the figures are all in millimeters.

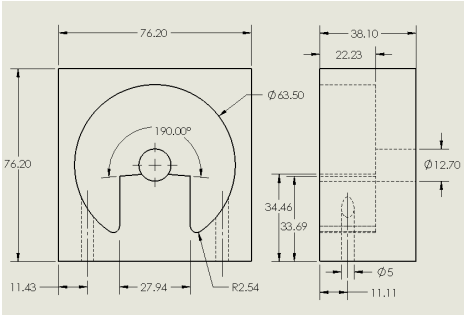

Figure A.4: CAD drawing of first half of vane actuator.

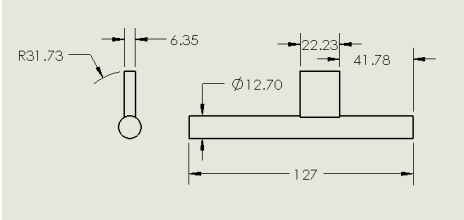

Figure A.5: CAD drawing of shaft with sliding seal

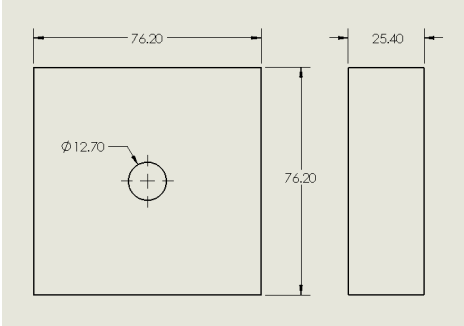

Figure A.6: CAD drawing of second half of vane actuator

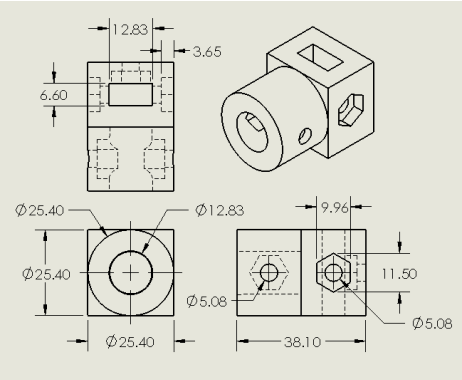

Figure A.7: CAD drawing of shaft coupler

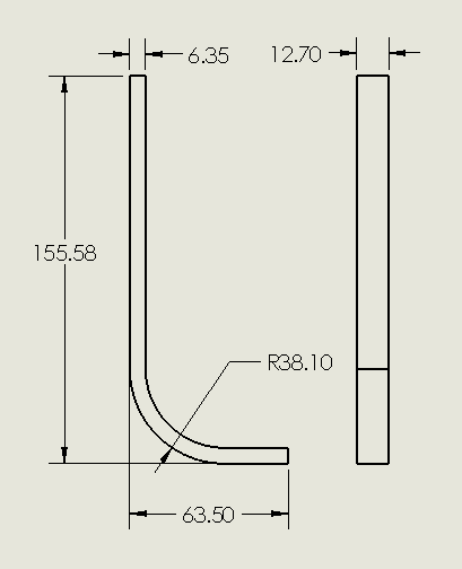

Figure A.8: CAD drawing of J-shaped extension

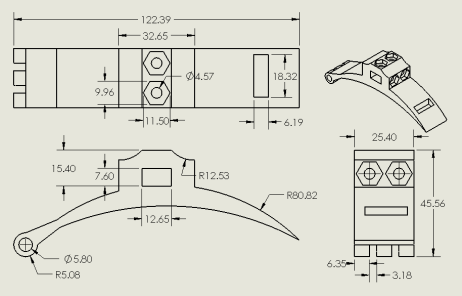

Figure A.9: CAD drawing of bottom hand clamp

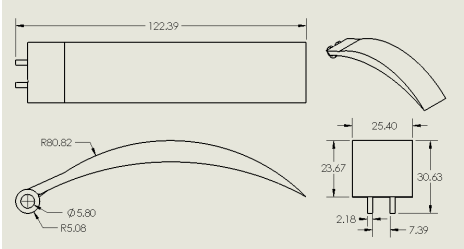

Figure A.10: CAD drawing of top hand clamp

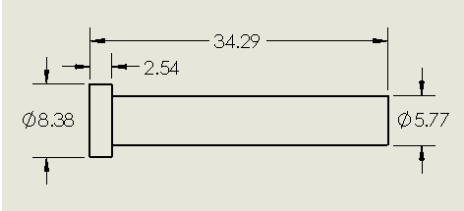

Figure A.11: CAD drawing of hand clamp pin

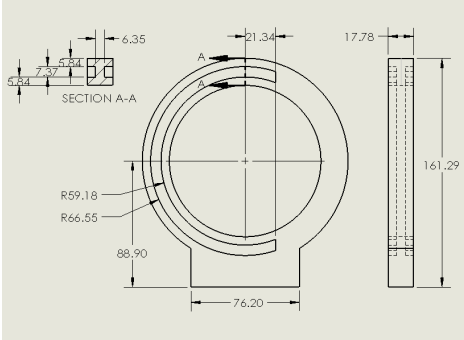

Figure A.12: CAD drawing of circular ring

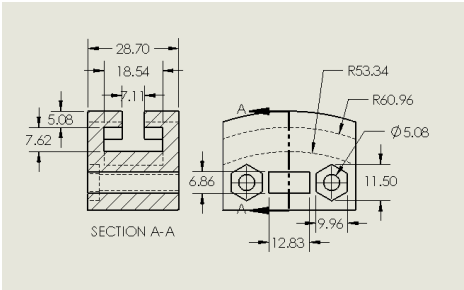

Figure A.13: CAD drawing of sliding cart

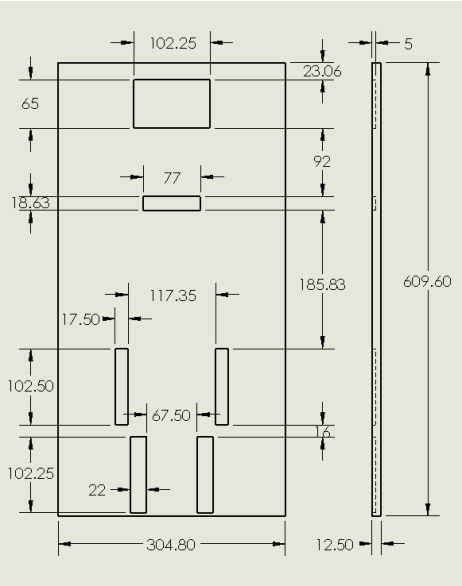

Figure A.14: CAD drawing of acrylic engraving

A.2.2 3D Models of Parts

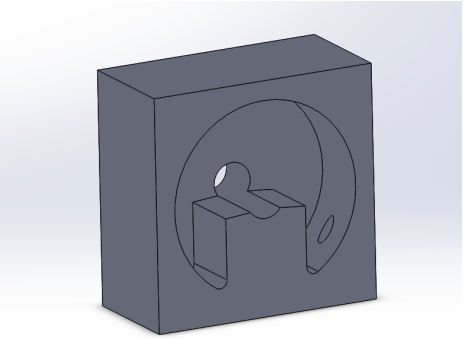

Figure A.15: 3D model of first half of vane actuator.

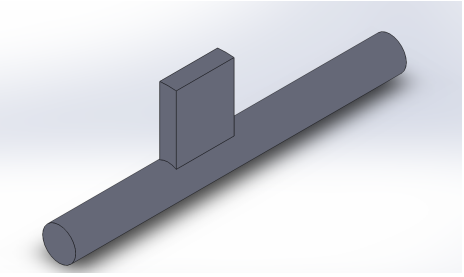

Figure A.16: 3D model of shaft with sliding seal

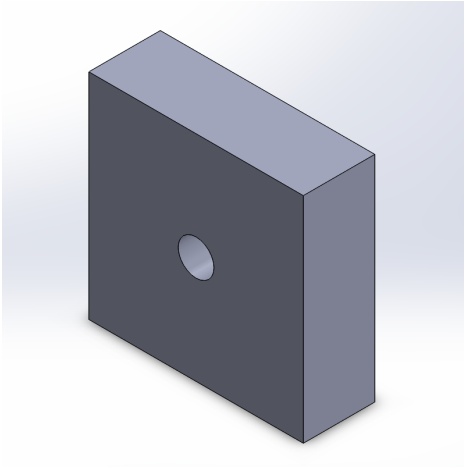

Figure A.17: 3D model of second half of vane actuator

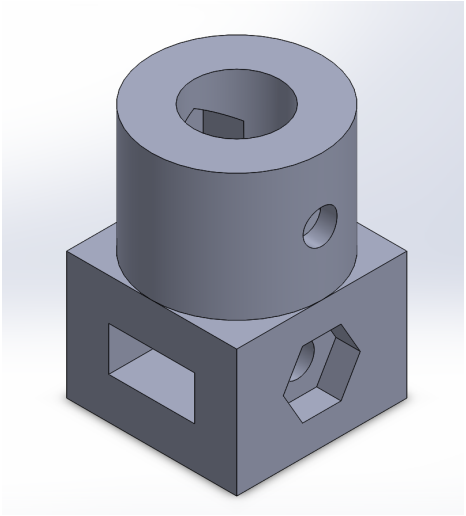

Figure A.18: 3D model of shaft coupler

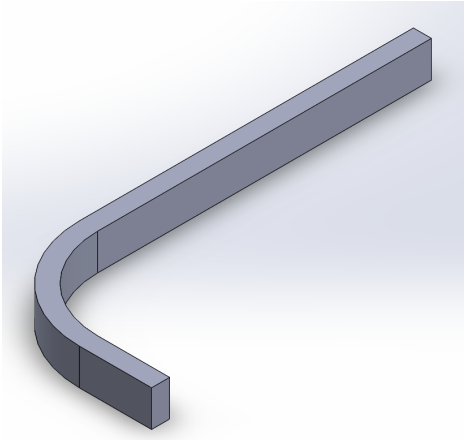

Figure A.19: 3D model of J-shaped extension

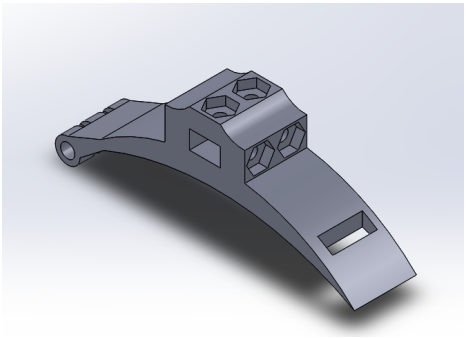

Figure A.20: 3D model of bottom hand clamp

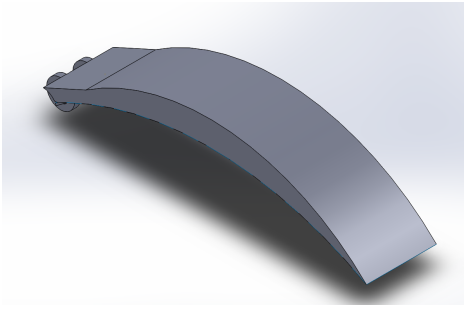

Figure A.21: 3D model of top hand clamp

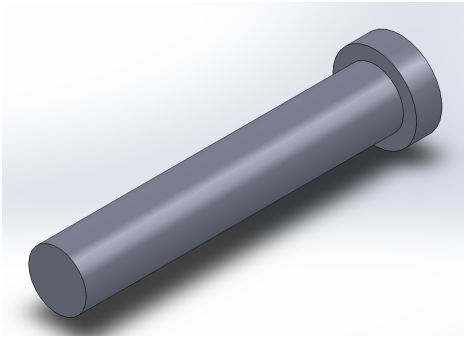

Figure A.22: 3D model of hand clamp pin

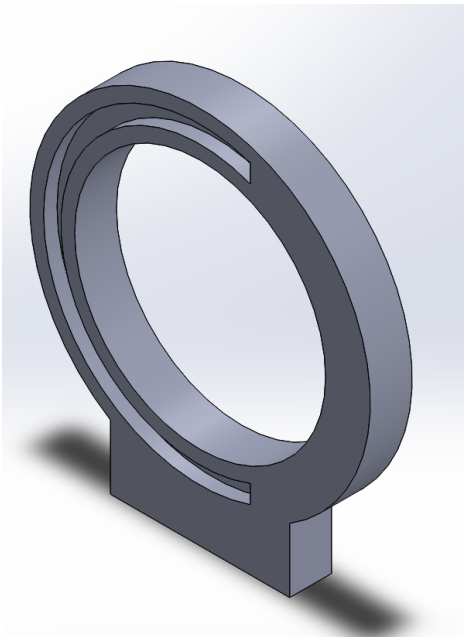

Figure A.23: 3D model of circular ring

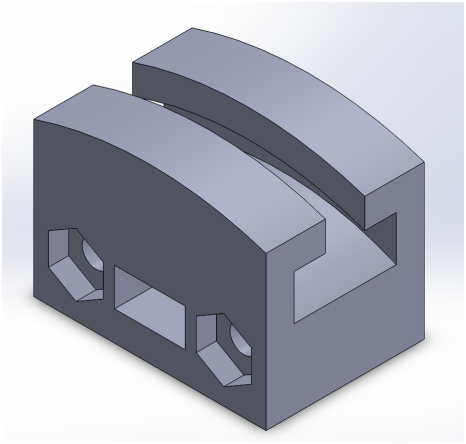

Figure A.24: 3D model of sliding cart

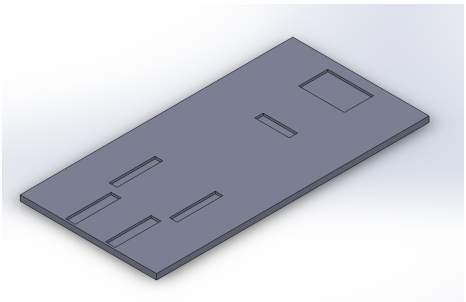

Figure A.25: 3D model of acrylic engraving

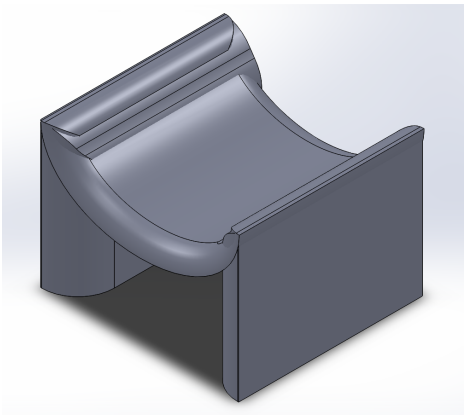

Figure A.26: 3D model of arm support

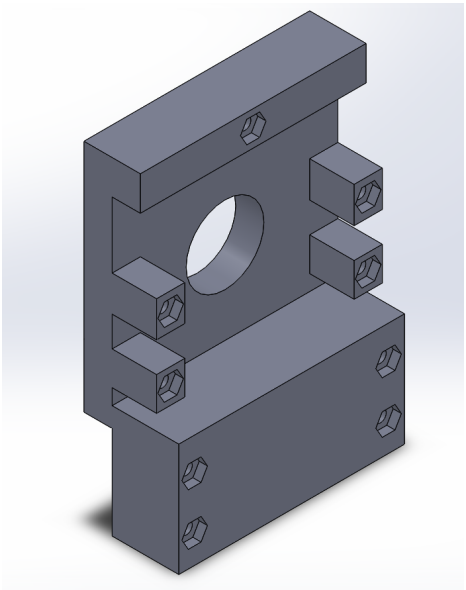

Figure A.27: 3D model of actuator base

A.3 Second Version of Rotational Device

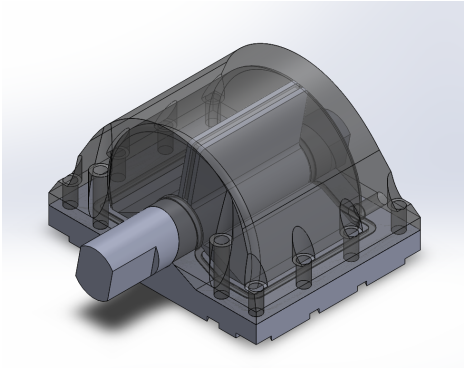

Figure A.28: 3D model of second version of rotational device

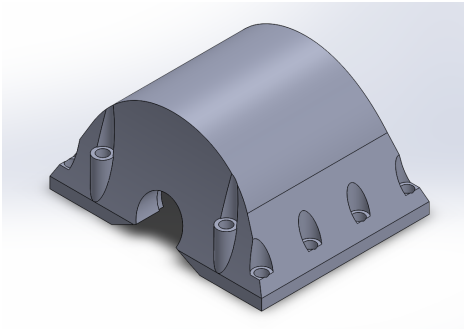

Figure A.29: 3D model of case

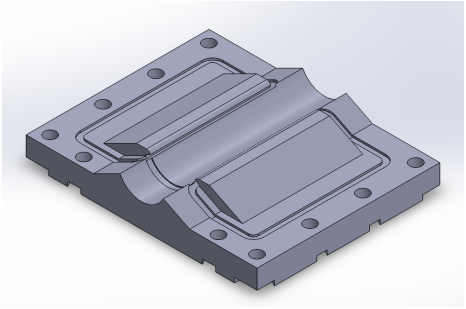

Figure A.30: 3D model of base

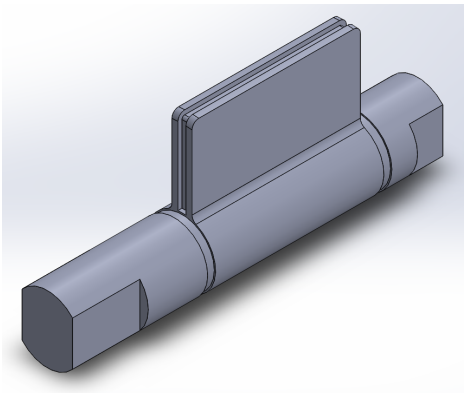

Figure A.31: 3D model of rod

APPENDIX B

INTRASUBJECT VARIABILITY EXAMPLE

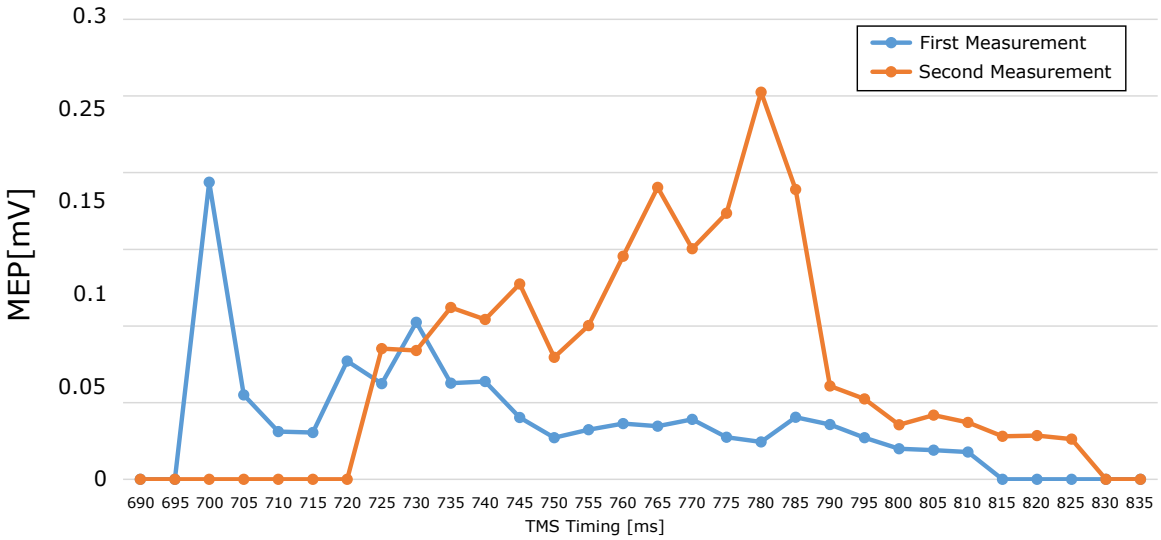

Figure B.1: Intrasubject variability ISI-W Example (n=1). MEP measurement was conducted for the same subject on two days (16 days apart).

REFERENCES

[1] P. Tonin, S. Casson, M. Ermani, G. Pizzolato, V. Iaia, and L. Battistin, "The effects of long-term rehabilitation therapy on poststroke hemiplegic patients," *Stroke*, vol. 24, no. 8, pp. 1186–1191, 1993.

[2] S Balasubramanian, J Klein, and E. Burdet, "Robot-assisted rehabilitation of hand function," *Current opinion in neurology*, vol. 23, pp. 661–670, 6 2010.

[3] A. A. Blank, J. A. French, A. U. Pehlivan, and M. K. OMalley, "Current trends in robot-assisted upper-limb stroke rehabilitation: Promoting patient engagement in therapy," *Current Physical Medicine and Rehabilitation Reports*, vol. 2, no. 3, 184195, 2014.

[4] K. E. Laver, S. George, S. Thomas, J. E. Deutsch, and M. Crotty, "Virtual reality for stroke rehabilitation," *Cochrane Database of Systematic Reviews*, 2015.

[5] B. Lange, C.-Y. Chang, E. Suma, B. Newman, A. S. Rizzo, and M. Bolas, "Development and evaluation of low cost game-based balance rehabilitation tool using the microsoft kinect sensor," in *Proceedings of 33rd Annual International Conference of the IEEE Engineering in Medicine and Biology Society*, 2011, pp. 1831–1834.

[6] K. Kawahira, M. Shimodozono, S. Etoh, K. Kamada, T. Noma, and N. Tanaka, "Effects of intensive repetition of a new facilitation technique on motor functional recovery of the hemiplegic upper limb and hand," *Brain Injury*, vol. 24, no. 10, pp. 1202–1213, 2010.

[7] E. Kim, I. Kovalenko, L. Lacey, M. Shinohara, and J. Ueda, "Timing analysis of robotic neuromodulatory rehabilitation system for paired associative stimulation," *IEEE Robotics and Automation Letters*, vol. 1, no. 2, pp. 1028–1035, 2016.

[8] E. Castel-Lacanal, A. Gerdelat-Mas, P. Marque, I. Loubinoux, and M. Simonetta-Moreau, "Induction of cortical plastic changes in wrist muscles by paired associative stimulation in healthy subjects and post-stroke patients," *Experimental Brain Research*, vol. 180, no. 1, pp. 113–122, 2007.

[9] N. Dancause, "Vicarious function of remote cortex following stroke: Recent evidence from human and animal studies," *The Neuroscientist*, vol. 12, no. 6, pp. 489–499, 2006.

[10] R. J. Nudo, B. Wise, F. SiFuentes, and G. Milliken, "Neural substrates for the effects of rehabilitative training on motor recovery after ischemic infarct," *Science*, vol. 272, no. 5269, pp. 1791–1794, 1996.

[11] A. Pascual-Leone, C. Freitas, L. Oberman, J. C. Horvath, M. Halko, M. Eldaief, S. Bashir, M. Vernet, M. Shafi, B. Westover, and et al., "Characterizing brain cortical plasticity and network dynamics across the age-span in health and disease with tms-eeg and tms-fmri," *Brain Topography*, vol. 24, no. 3-4, 302315, 2011.

[12] T. V. P. Bliss and G. L. Collingridge, "A synaptic model of memory: Long-term potentiation in the hippocampus," *Nature*, vol. 361, no. 6407, pp. 31–39, 1993.

[13] H. Markram, "Regulation of synaptic efficacy by coincidence of postsynaptic aps and epsps," *Science*, vol. 275, no. 5297, pp. 213–215, 1997.

[14] N. C. Kennedy and R. G. Carson, "The effect of simultaneous contractions of ipsilateral muscles on changes in corticospinal excitability induced by paired associative stimulation (pas)," *Neuroscience Letters*, vol. 445, no. 1, pp. 7–11, 2008.

[15] S. Meunier, H. Russmann, M. Simonetta-Moreau, and M. Hallett, "Changes in spinal excitability after pas," *Journal of Neurophysiology*, vol. 97, no. 4, 31313135, 2007.

[16] K. Stefan, "Induction of plasticity in the human motor cortex by paired associative stimulation," *Brain*, vol. 123, no. 3, pp. 572–584, 2000.

[17] T Fulp, N Douziech, M. Jacob, M Hauck, J Wallach, and L Robert, "Age-related alterations in the signal transduction pathways of the elastin-laminin receptor," *Pathologie Biologie*, vol. 49, no. 4, pp. 339–348, 2001.

[18] R. Soudmand, L. C. Ward, and T. R. Swift, "Effect of height on nerve conduction velocity," *Neurology*, vol. 32, no. 4, pp. 407–407, 1982.

[19] W Hennessey, "Gender and arm length: Influence on nerve conduction parameters in the upper limb," *Archives of Physical Medicine and Rehabilitation*, vol. 75, no. 3, pp. 265–269, 1994.

[20] R. M. Buschbacher, "Body mass index effect on common nerve conduction study measurements," *Muscle & Nerve*, vol. 21, no. 11, pp. 1398–1404, 1998.

[21] S. Kumpulainen, N. Mrachacz-Kersting, J. Peltonen, M. Voigt, and J. Avela, "The optimal interstimulus interval and repeatability of paired associative stimulation when the soleus muscle is targeted," *Experimental Brain Research*, vol. 221, no. 3, 241–249, 2012.

[22] H. Tokimura, V. D. Lazzaro, Y. Tokimura, A. Oliviero, P. Profice, A. Insola, P. Mazzone, P. Tonali, and J. C. Rothwell, "Short latency inhibition of human hand motor cortex by somatosensory input from the hand," *The Journal of Physiology*, vol. 523, no. 2, 503513, 2000.

[23] A. Sailer, "Short and long latency afferent inhibition in parkinsons disease," *Brain*, vol. 126, no. 8, 18831894, 2003.

[24] R. Bikmullina, T. Bumer, S. Zittel, and A. Mnchau, "Sensory afferent inhibition within and between limbs in humans," *Clinical Neurophysiology*, vol. 120, no. 3, 610618, 2009.

[25] S. C. Schwerin, J. Yao, and J. P. Dewald, "Using paired pulse tms to facilitate contralateral and ipsilateral meps in upper extremity muscles of chronic hemiparetic stroke patients," *Journal of Neuroscience Methods*, vol. 195, no. 2, 151160, 2011.

[26] S. Grosprłtre and A. Martin, "Conditioning effect of transcranial magnetic stimulation evoking motor-evoked potential on v-wave response," *Physiological Reports*, vol. 2, no. 12, 2014.

[27] K. Kawahira, M. Shimodozono, A. Ogata, and N. Tanaka, "Addition of intensive repetition of facilitation exercise to multidisciplinary rehabilitation promotes motor functional recovery of the hemiplegic lower limb," *J. of Rehabilitation Medicine*, vol. 36, no. 4, pp. 159–164, 2004.

[28] K. Kawakami, H. Miyasaka, S. Nonoyama, K. Hayashi, Y. Tonogai, G. Tanino, Y. Wada, A. Narukawa, Y. Okuyama, Y. Tomita, and S. Sonoda, "Randomized controlled comparative study on effect of training to improve lower limb motor paralysis in convalescent patients with post-stroke hemiplegia," *J. of Physical Therapy Science*, vol. 27, no. 9, pp. 2947–2950, 2015.

[29] M. Shimodozono, T. Noma, Y. Nomoto, N. Hisamatsu, K. Kamada, R. Miyata, S. Matsumoto, A. Ogata, S. Etoh, J. Basford, and K. Kawahira, "Benefits of a repetitive facilitative exercise program for the upper paretic extremity after subacute stroke: A randomized controlled trial.," *Neurorehabil neural repair.*, vol. 27(4), pp. 296–305, 2013.

[30] M. Shimodozono, T. Noma, S. Matsumoto, R. Miyata, S. Etoh, and K. Kawahira, "Repetitive facilitative exercise under continuous electrical stimulation for severe arm impairment after sub-acute stroke: A randomized controlled pilot study.," *Brain Injury*, vol. 28(2), pp. 203–10, 2014.

[31] M. F. Davis, C. C. Lay, C. H. Chen-Bee, and R. D. Frostig, "Amount but not pattern of protective sensory stimulation alters recovery after permanent middle cerebral artery occlusion," *Stroke*, vol. 42, no. 3, 792798, 2011.

[32] C. C. Lay, M. F. Davis, C. H. Chen-Bee, and R. D. Frostig, "Mild sensory stimulation completely protects the adult rodent cortex from ischemic stroke," *PLoS ONE*, vol. 5, no. 6, 2010.

[33] C. C. Lay, M. F. Davis, C. H. Chen-Bee, and R. D. Frostig, "Mild sensory stimulation reestablishes cortical function during the acute phase of ischemia," *Journal of Neuroscience*, vol. 31, no. 32, 1149511504, 2011.

[34] J. Classen, A. Wolters, K. Stefan, M. Wycislo, F. Sandbrink, A. Schmidt, and E. Kunesch, "Chapter 59 paired associative stimulation," *Supplements to Clinical Neurophysiology*, vol. 57, no. 3, pp. 563–569, 2004.

[35] E. Kim, W. Meinhold, and J. Ueda, "Assessment of robot necessity in time interval dependent rehabilitation therapy," *2018 International Symposium on Medical Robotics (ISMR)*, 2018.

[36] K. T. Patton and G. A. Thibodeau, *Brief Atlas of the Human Body t/a Anatomy & Physiology 7th*. Mosby EIseveir, 2010.

[37] L. Lacey, A. Maliki, D. Bhatacharjee, J. Veldhorst, and J. Ueda, "Design of mri-compatible hemiparesis rehabilitation device," *J. of Medical Devices*, vol. 8, no. 2, p. 020 929, 2014.

[38] F. C. Hummel and L. G. Cohen, "Non-invasive brain stimulation: A new strategy to improve neurorehabilitation after stroke?" *The Lancet Neurology*, vol. 5, no. 8, 708712, 2006.

[39] P. Jung and U. Ziemann, "Homeostatic and nonhomeostatic modulation of learning in human motor cortex," *Journal of Neuroscience*, vol. 29, no. 17, 55975604, 2009.

[40] J. T. H. Teo, O. B. C. Swayne, B. Cheeran, R. J. Greenwood, and J. C. Rothwell, "Human theta burst stimulation enhances subsequent motor learning and increases performance variability," *Cerebral Cortex*, vol. 21, no. 7, 16271638, 2010.

[41] Y.-H. Kim, S. H. You, M.-H. Ko, J.-W. Park, K. H. Lee, S. H. Jang, W.-K. Yoo, and M. Hallett, "Repetitive transcranial magnetic stimulationinduced corticomotor excitability and associated motor skill acquisition in chronic stroke," *Stroke*, vol. 37, no. 6, 14711476, 2006.

[42] V. D. Lazzaro, P. Profice, F. Pilato, F. Capone, F. Ranieri, P. Pasqualetti, C. Colosimo, E. Pravat, A. Cianfoni, M. Dileone, and et al., "Motor cortex plasticity predicts recovery in acute stroke," *Cerebral Cortex*, vol. 20, no. 7, 15231528, 2009.

[43] N. C. Kennedy and R. G. Carson, "The effect of simultaneous contractions of ipsilateral muscles on changes in corticospinal excitability induced by paired associative stimulation (pas)," *Neuroscience Letters*, vol. 445, no. 1, 711, 2008.

[44] S. Meunier, H. Russmann, M. Simonetta-Moreau, and M. Hallett, "Changes in spinal excitability after pas," *Journal of Neurophysiology*, vol. 97, no. 4, 31313135, 2007.

[45] K. Stefan, "Induction of plasticity in the human motor cortex by paired associative stimulation," *Brain*, vol. 123, no. 3, pp. 572–584, 2000.

[46] A. Wolters *et al.*, "A temporally asymmetric hebbian rule governing plasticity in the human motor cortex," *J. of Neurophysiology*, vol. 89, no. 5, pp. 2339–2345, 2003.

[47] R. G. Carson and N. C. Kennedy, "Modulation of human corticospinal excitability by paired associative stimulation," *Frontiers in Human Neuroscience*, vol. 7, 2013.

[48] M. Shimodozono, T. Noma, Y. Nomoto, N. Hisamatsu, K. Kamada, R. Miyata, S. Matsumoto, A. Ogata, S. Etoh, J. R. Basford, and et al., "Benefits of a repetitive facilitative exercise program for the upper paretic extremity after subacute stroke," *Neurorehabilitation and Neural Repair*, vol. 27, no. 4, 296305, 2012.

[49] K. Kawahira, T. Noma, J. Iiyama, S. Etoh, A. Ogata, and M. Shimodozono, "Improvements in limb kinetic apraxia by repetition of a newly designed facilitation exercise in a patient with corticobasal degeneration," *International Journal of Rehabilitation Research*, vol. 32, no. 2, 178183, 2009.

[50] S. Matsumoto, M. Shimodozono, T. Noma, T. Uema, S. Horio, K. Tomioka, J.-I. Sameshima, N. Yunoki, and K. Kawahira, "Outcomes of repetitive facilitation exercises in convalescent patients after stroke with impaired health status," *Brain Injury*, vol. 30, no. 13-14, 17221730, 2016.

[51] P. Langhorne, J. Bernhardt, and G. Kwakkel, "Stroke rehabilitation," *The Lancet*, vol. 377, no. 9778, 16931702, 2011.

[52] A. Pollock, S. E. Farmer, M. C. Brady, P. Langhorne, G. E. Mead, J. Mehrholz, and F. V. Wijck, "Interventions for improving upper limb function after stroke," *Cochrane Database of Systematic Reviews*, 2014.

[53] J. M. Veerbeek, E. V. Wegen, R. V. Peppen, P. J.V. D. Wees, E. Hendriks, M. Rietberg, and G. Kwakkel, "What is the evidence for physical therapy poststroke? a systematic review and meta-analysis," *PLoS ONE*, vol. 9, no. 2, 2014.

[54] S. Kumpulainen, N. Mrachacz-Kersting, J. Peltonen, M. Voigt, and J. Avela, "The optimal interstimulus interval and repeatability of paired associative stimulation when the soleus muscle is targeted," *Experimental Brain Research*, vol. 221, no. 3, 241249, 2012.

[55] D. E. Poon, F. D. Roy, M. A. Gorassini, and R. B. Stein, "Interaction of paired cortical and peripheral nerve stimulation on human motor neurons," *Experimental Brain Research*, vol. 188, no. 1, pp. 13–21, 2008.

[56] D. R. Pereira, S. Cardoso, F. Ferreira-Santos, C. Fernandes, C. Cunha-Reis, T. O. Paiva, P. R. Almeida, C. Silveira, F. Barbosa, J. Marques-Teixeira, and et al., "Effects of inter-stimulus interval (isi) duration on the n1 and p2 components of the auditory event-related potential," *International Journal of Psychophysiology*, vol. 94, no. 3, 311318, 2014.

[57] N. Takeuchi and S.-I. Izumi, "Combinations of stroke neurorehabilitation to facilitate motor recovery: Perspectives on hebbian plasticity and homeostatic metaplasticity," *Frontiers in Human Neuroscience*, vol. 9, p. 349, 2015.

[58] A. Wolters, A. Schmidt, A. Schramm, D. Zeller, M. Naumann, E. Kunesch, R. Benecke, K. Reiners, and J. Classen, "Timing-dependent plasticity in human primary somatosensory cortex," *The Journal of Physiology*, vol. 565, no. 3, 10391052, 2005.

[59] T Fulp, N Douziech, M. Jacob, M Hauck, J Wallach, and L Robert, "Age-related alterations in the signal transduction pathways of the elastin-laminin receptor," *Pathologie Biologie*, vol. 49, no. 4, pp. 339–348, 2001.

[60] D. A. Cohen, C. Freitas, J. M. Tormos, L. Oberman, M. Eldaief, and A. Pascual-Leone, "Enhancing plasticity through repeated rtms sessions: The benefits of a night of sleep," *Clinical Neurophysiology*, vol. 121, no. 12, 21592164, 2010.

[61] H. J. Lee, Y. W. Park, D. H. Jeong, and H. Y. Jung, "Effects of night sleep on motor learning using transcranial magnetic stimulation," *Annals of Rehabilitation Medicine*, vol. 36, no. 2, p. 226, 2012.

[62] D. O. HEBB, *The organization of behavior: a neuropsychological theory*. John Wiley & Sons, 1949.

[63] T. V. P. Bliss and G. L. Collingridge, "A synaptic model of memory: Long-term potentiation in the hippocampus," *Nature*, vol. 361, no. 6407, 3139, 1993.

[64] H. Markram, "Regulation of synaptic efficacy by coincidence of postsynaptic aps and epsps," *Science*, vol. 275, no. 5297, 213215, 1997.

[65] K. Stefan, E. Kunesch, R. Benecke, L. G. Cohen, and J. Classen, "Mechanisms of enhancement of human motor cortex excitability induced by interventional paired associative stimulation," *The Journal of Physiology*, vol. 543, no. 2, 699708, 2002.

[66] U. Ziemann, "Learning modifies subsequent induction of long-term potentiation-like and long-term depression-like plasticity in human motor cortex," *Journal of Neuroscience*, vol. 24, no. 7, 16661672, 2004.

[67] J. F. M. Mller, Y. Orekhov, Y. Liu, and U. Ziemann, "Erratum: Homeostatic plasticity in human motor cortex demonstrated by two consecutive sessions of paired associative stimulation," *European Journal of Neuroscience*, vol. 26, no. 4, 10771077, 2007.

[68] V. D. Lazzaro, A. Oliviero, P. Profice, M. A. Pennisi, S. D. Giovanni, G. Zito, P. Tonali, and J. C. Rothwell, "Muscarinic receptor blockade has differential effects on the excitability of intracortical circuits in the human motor cortex," *Experimental Brain Research*, vol. 135, no. 4, 455461, 2000.

[69] R. Aronoff, F. Matyas, C. Mateo, C. Ciron, B. Schneider, and C. C. Petersen, "Long-range connectivity of mouse primary somatosensory barrel cortex," *European Journal of Neuroscience*, vol. 31, no. 12, 22212233, 2010.

[70] I. Ferezou, F. Haiss, L. J. Gentet, R. Aronoff, B. Weber, and C. C. Petersen, "Spatiotemporal dynamics of cortical sensorimotor integration in behaving mice," *Neuron*, vol. 56, no. 5, 907923, 2007.

[71] V. D. Lazzaro, F. Pilato, M. Dileone, P. Profice, F. Ranieri, V. Ricci, P. Bria, P. Tonali, and U. Ziemann, "Segregating two inhibitory circuits in human motor cortex at the level of gabaa receptor subtypes: A tms study," *Clinical Neurophysiology*, vol. 118, no. 10, 22072214, 2007.

[72] J. C. Rothwell, M. M. Traub, and C. D. Marsden, "Influence of voluntary intent on the human long-latency stretch reflex," *Nature*, vol. 286, no. 5772, 496498, 1980.

[73] M. Shinohara, C. T. Moritz, M. A. Pascoe, and R. M. Enoka, "Prolonged muscle vibration increases stretch reflex amplitude, motor unit discharge rate, and force fluctuations in a hand muscle," *Journal of Applied Physiology*, vol. 99, no. 5, 18351842, 2005.

[74] S. Kojima, H. Onishi, K. Sugawara, S. Miyaguchi, H. Kirimoto, H. Tamaki, H. Shirozu, and S. Kameyama, "No relation between afferent facilitation induced by digital nerve stimulation and the latency of cutaneomuscular reflexes and somatosensory evoked magnetic fields," *Frontiers in Human Neuroscience*, vol. 8, 2014.

[75] H. Devanne, A. Degardin, L. Tyvaert, P. Bocquillon, E. Houdayer, A. Manceaux, P. Derambure, and F. Cassim, "Afferent-induced facilitation of primary motor cortex excitability in the region controlling hand muscles in humans," *European Journal of Neuroscience*, vol. 30, no. 3, 439448, 2009.

[76] S. Tamburin, A. Fiaschi, A. Andreoli, S. Marani, and G. Zanette, "Sensorimotor integration to cutaneous afferents in humans: The effect of the size of the receptive field," *Experimental Brain Research*, vol. 167, no. 3, 362369, 2005.

[77] R. Chen, B. Corwell, and M. Hallett, "Modulation of motor cortex excitability by median nerve and digit stimulation," *Experimental Brain Research*, vol. 129, no. 1, p. 77, 1999.

[78] B. L. Day, H Riescher, A Struppler, J. C. Rothwell, and C. D. Marsden, "Changes in the response to magnetic and electrical stimulation of the motor cortex following muscle stretch in man.," *The Journal of Physiology*, vol. 433, no. 1, 4157, 1991.

[79] E. Kim, M. Shinohara, and J. Ueda, "Optimal inter-stimulus interval for paired associative stimulation with mechanical stimulation," *2017 39th Annual International Conference of the IEEE Engineering in Medicine and Biology Society (EMBC)*, 2017.

[80] E. Kim, I. Kovalenko, L. Lacey, M. Shinohara, and J. Ueda, "Timing analysis of robotic neuromodulatory rehabilitation system for paired associative stimulation," *IEEE Robotics and Automation Letters*, vol. 1, no. 2, 10281035, 2016.

[81] M.-C. Lo and A. S. Widge, "Closed-loop neuromodulation systems: Next-generation treatments for psychiatric illness," *International Review of Psychiatry*, vol. 29, no. 2, 191204, 2017.

[82] M. N. Raczkowska, W. Y. X. Peh, Y. Teh, M. Alam, S.-C. Yen, and N. V. Thakor, "Closed-loop bladder neuromodulation therapy in spinal cord injury rat model," *2019 9th International IEEE/EMBS Conference on Neural Engineering (NER)*, 2019.

[83] A. Delitto, M. J. Strube, A. D. Shulman, and S. D. Minor, "A study of discomfort with electrical stimulation," *Physical Therapy*, vol. 72, no. 6, 410421, 1992.

[84] E Pierrot-Deseilligny and D Mazevet, "The monosynaptic reflex: A tool to investigate motor control in humans. interest and limits," *Neurophysiologie Clinique/Clinical Neurophysiology*, vol. 30, no. 2, 6780, 2000.

[85] H. Motulsky and A. Christopoulos, *Fitting models to biological data using linear and nonlinear regression: a practical guide to curve fitting*. Oxford Univ. Press, 2010.

[86] C. E. Rasmussen and C. K. I. Williams, *Gaussian processes for machine learning*. MIT Press, 2008.

[87] K. Takemura, E. Kim, and J. Ueda, "Individualized inter-stimulus timing estimation for neural facilitation in human motor system: A particle filtering approach," in *ASME 2018 Dynamic Systems and Control Conference*, 2018.

[88] N. J. Gordon *et al.*, "Novel approach to nonlinear/non-gaussian bayesian state estimation," *IEE Proceedings F - Radar and Signal Processing*, vol. 140, no. 2, pp. 107–113, 1993.

[89] L. Lacey, V. Buharin, M. Turkseven, M. Shinohara, and J. Ueda, "Control of voluntary and involuntary nerve impulses for hemiparesis rehabilitation and mri study," *ASME 2013 Dynamic Systems and Control Conference*, 2013.

[90] D. Burke, S. C. Gandevia, and B. McKeon, "The afferent volleys responsible for spinal proprioceptive reflexes in man," *The Journal of Physiology*, vol. 339, no. 1, pp. 535–552, 1983.

[91] Y. Ma, N. V. Thakor, and X. Jia, "Statistical model applied to motor evoked potentials analysis," *2011 Annual International Conference of the IEEE Engineering in Medicine and Biology Society*, 2011.

[92] S. M. Goetz, B. Luber, S. H. Lisanby, and A. V. Peterchev, "A novel model incorporating two variability sources for describing motor evoked potentials," *Brain Stimulation*, vol. 7, no. 4, 541552, 2014.

[93] S. M. Goetz and A. V. Peterchev, "A model of variability in brain stimulation evoked responses," *2012 Annual International Conference of the IEEE Engineering in Medicine and Biology Society*, 2012.

[94] J. Cirillo, F. J. Calabro, and M. A. Perez, "Impaired organization of paired-pulse tms-induced i-waves after human spinal cord injury," *Cerebral Cortex*, vol. 26, no. 5, 21672177, 2015.

[95] J. Cirillo and M. A. Perez, "Subcortical contribution to late tms-induced i-waves in intact humans," *Frontiers in Integrative Neuroscience*, vol. 9, 2015.

[96] A. Mohammadi, M. Ebrahimi, S. Kaartinen, G. Jarnefelt, J. Karhu, and P. Julkunen, "Individual characterization of fast intracortical facilitation with paired biphasic-wave transcranial magnetic stimulation," *IEEE Transactions on Neural Systems and Rehabilitation Engineering*, vol. 26, no. 9, 17101716, 2018.

[97] I Delvendahl, H Lindemann, A Pechmann, H Siebner, and V Mall, "Influence of current direction on short-interval intracortical facilitation probed with paired-pulse tms," *Klinische Neurophysiologie*, vol. 43, no. 01, 2012.

[98] E. Kallioniemi, P. Savolainen, G. Jrnefelt, P. Koskenkorva, J. Karhu, and P. Julkunen, "Transcranial magnetic stimulation modulation of corticospinal excitability by targeting cortical i-waves with biphasic paired-pulses," *Brain Stimulation*, vol. 11, no. 2, 322326, 2018.

[99] J. F. M. Mller-Dahlhaus, Y. Orekhov, Y. Liu, and U. Ziemann, "Interindividual variability and age-dependency of motor cortical plasticity induced by paired associative stimulation," *Experimental Brain Research*, vol. 187, no. 3, 467475, 2008.

[100] M. Wischnewski and D. J. Schutter, "Efficacy and time course of paired associative stimulation in cortical plasticity: Implications for neuropsychiatry," *Clinical Neurophysiology*, vol. 127, no. 1, 732739, 2016.

[101] J. Wearden, "Do humans possess an internal clock with scalar timing properties?" *Learning and Motivation*, vol. 22, no. 1-2, 5983, 1991.

[102] E. Kim *et al.*, "Optimal inter-stimulus interval for paired associative stimulation with mechanical stimulation," in *Proc. of 39th Annual Int. Conf. of the IEEE Engineering in Medicine and Biology Society*, 2017, pp. 1134–1137.

[103] L. Lacey, A. Maliki, D. Bhattacharjee, J. Veldhorst, and J. Ueda, "Design of mri-compatible hemiparesis rehabilitation device," *Journal of Medical Devices*, vol. 8, no. 2, p. 020 928, 2014.

[104] Y. Youm, R. Dryer, K Thambyrajah, A. Flatt, and B. Sprague, "Biomechanical analyses of forearm pronation-supination and elbow flexion-extension," *Journal of Biomechanics*, vol. 12, no. 4, pp. 245–255, 1979.

[105] F. Abyarjoo, A. Barreto, S. Abyarjoo, F. R. Ortega, and J. Cofino, "Monitoring human wrist rotation in three degrees of freedom," in *Southeastcon, 2013 Proceedings of IEEE*, IEEE, 2013, pp. 1–5.

[106] N. V. Tsekos, A. Khanicheh, E. Christoforou, and C. Mavroidis, "Magnetic resonance-compatible robotic and mechatronics systems for image-guided interventions and rehabilitation: A review study," *Annu. Rev. Biomed. Eng.*, vol. 9, pp. 351–387, 2007.

[107] J. F. Schenck, "''the role of magnetic susceptibility in magnetic resonance imaging: Mri magnetic compatibility of the first and second kinds", medical physics," *Vol.*, vol. 23, pp. 815–997, 1996.

[108] Y. Lin-Chen, J Wang, and Q. Wu, "A software tool development for pneumatic actuator system simulation and design," *Computers in industry*, vol. 51, no. 1, pp. 73–88, 2003.

[109] C. Bode, "Design of an mr-safe haptic wrist manipulator for movement disorder diagnostics," PhD thesis, TU Delft, Delft University of Technology, 2012.

[110] M. Sorli, L. Gastaldi, E Codina, and S. de las Heras, "Dynamic analysis of pneumatic actuators," *Simulation Practice and Theory*, vol. 7, no. 5, pp. 589–602, 1999.

[111] J. Ueda, L. Lacey, M. Turkseven, M. Shinohara, I. Kovalenko, E. Kim, and F. Sulejmani, "Robotic neuromuscular facilitation for regaining neural activation in hemiparetic limbs," *Volume 5A: 39th Mechanisms and Robotics Conference*, 2015.

[112] I. Kovalenko, J. Lai, J. Williams, A. Maliki, and J. Ueda, "Design and testing of a pneumatic hemiparesis rehabilitation device for a neurofacilitation exercise1," *Journal of Medical Devices*, vol. 9, no. 3, 2015.

[113] P. Beater, "6 Modelling of Long Lines," no. Hennig 1982, pp. 473–477, 2004.

[114] ISO6358:1989, *Pneumatic fluid power - components using compressible fluids - determination of flow-rate characteristics*, Norm, 1989.

[115] P. Bigras and K. Khayati, "Nonlinear Observer for Pneumatic System With Non Negligible Connection Port Restriction," pp. 0–4, 2002.

[116] N. Gulati and E. Barth, "A Globally Stable, Load-Independent Pressure Observer for the Servo Control of Pneumatic Actuators," *IEEE/ASME Transactions on Mechatronics*, vol. 14, no. 3, pp. 295–306, Jun. 2009.

[117] C. K. Skinner and F. D. Wagner, "A study of the process of charging and discharging constant volume tanks with air," PhD thesis, Dept. Mech. Eng. M.I.T., Cambridge, MA, 1954.

[118] E. Richer and Y. Hurmuzlu, "A High Performance Pneumatic Force Actuator System : Part I Nonlinear Mathematical," vol. 122, no. September, 2000.

[119] B. Yang, U.-x. Tan, A. Mcmillan, R. Gullapalli, J. P. Desai, and S. Member, "Design and Implementation of a Pneumatically-Actuated Robot for Breast Biopsy under Continuous MRI," 2011.

[120] W. Meinhold, S.-I. Izumi, and J. Ueda, "Automated variable stimulus tendon tapping modulates somatosensory evoked potentials," *2019 IEEE 16th International Conference on Rehabilitation Robotics (ICORR)*, 2019.

[121] R. Treister, M. Lang, M. M. Klein, and A. L. Oaklander, "Non-invasive transcranial magnetic stimulation (tms) of the motor cortex for neuropathic painat the tipping point?" *Rambam Maimonides Medical Journal*, vol. 4, no. 4, 2013.

[122] S. Rossi, M. Hallett, P. M. Rossini, and A. Pascual-Leone, "Safety, ethical considerations, and application guidelines for the use of transcranial magnetic stimulation in clinical practice and research," *Clinical Neurophysiology*, vol. 120, no. 12, 20082039, 2009.

[123] L. M. Koponen, J. O. Nieminen, and R. J. Ilmoniemi, "Minimum-energy coils for transcranial magnetic stimulation: Application to focal stimulation," *Brain Stimulation*, vol. 8, no. 1, 124134, 2015.